http://lib.uliege.ac.be http://matheo.uliege.be

Master thesis : Experimental and numerical study of first passage time

Auteur : Delhez, Elise
Promoteur(s) : Golinval, Jean-Claude; Denoel, Vincent
Faculté : Faculté des Sciences appliquées
Diplôme : Master en ingénieur civil en aérospatiale, à finalité spécialisée en "aerospace engineering"
Année académique : 2017-2018
URI/URL : http://hdl.handle.net/2268.2/4622

Avertissement à l'attention des usagers :

Tous les documents placés en accès ouvert sur le site le site MatheO sont protégés par le droit d'auteur. Conformément aux principes énoncés par la "Budapest Open Access Initiative"(BOAI, 2002), l'utilisateur du site peut lire, télécharger, copier, transmettre, imprimer, chercher ou faire un lien vers le texte intégral de ces documents, les disséquer pour les indexer, s'en servir de données pour un logiciel, ou s'en servir à toute autre fin légale (ou prévue par la réglementation relative au droit d'auteur). Toute utilisation du document à des fins commerciales est strictement interdite.

Par ailleurs, l'utilisateur s'engage à respecter les droits moraux de l'auteur, principalement le droit à l'intégrité de l'oeuvre et le droit de paternité et ce dans toute utilisation que l'utilisateur entreprend. Ainsi, à titre d'exemple, lorsqu'il reproduira un document par extrait ou dans son intégralité, l'utilisateur citera de manière complète les sources telles que mentionnées ci-dessus. Toute utilisation non explicitement autorisée ci-avant (telle que par exemple, la modification du document ou son résumé) nécessite l'autorisation préalable et expresse des auteurs ou de leurs ayants droit.

Élise DELHEZ

Experimental and numerical study of first passage time

Master thesis submitted in partial fulfillment of the requirements for the degree of Master in Aerospace Engineering

University of Liège
Faculty of Applied Sciences
Academic year 2017-2018

ABSTRACT

The first passage time refers to the time required for a dynamical system to reach a target energy level for the first time, starting from a known initial state. This concept has been developed as an efficient alternative to the classical stability theories that are no longer relevant in the stochastic context. Analytical studies of single-degree-of-freedom systems governed by the linear Mathieu equation and subjected to broadband forced and parametric excitations have revealed the existence of different regimes for the first passage time.

This Master thesis aims at the experimental validation of the existence of these regimes for a real structure. The experimental set-up consists in a vertical strip pre-stressed by a mass and subjected to forced and parametric excitations. The complete process, from the structure design to the experimental validation, is conducted in this work.

A finite element model of the structure is built in MATLAB to get a numerical representation of the dynamics of the structure. The model is updated by implementing various state-of-the-art techniques from the field of experimental modal analysis. Data acquisition and signal processing are carried out using the LMS Test.Lab software and the LMS SCADAS Lab acquisition system.

A model reduction of the full multi-degree-of-freedom system is introduced to match the conditions of the analytical results. It is shown that the dynamics of the structure can be approached by a single-degree-of-freedom reduced model if both the forced and parametric excitations are narrow-band processes triggering only one mode of the structure. The influence of narrow-band excitations on the first passage time is therefore studied numerically. Behaviors similar to the broadband excitations case considered in the analytical study can be recovered when the frequency band of the forced excitation includes the natural frequency of the oscillator and the frequency band of the parametric excitation contains the corresponding second harmonic. Depending on the other parameters of the problem, small quantitative differences can be observed but the dynamics remains qualitatively similar.

The results of this numerical preparatory study are used to define the conditions of the experimental tests. First passage time maps are reproduced experimentally in the framework of the linear single-degree-of-freedom Mathieu equation. Some tests are also carried out to get a first insight into the first passage time maps of nonlinear or multi-degree-of-freedom systems.

This work provides the first physical evidence that the first passage time of real multi-degree-of-freedom systems can be characterized with the physical properties of the structure. It also addresses for the first time the influence of narrow-band excitations. Therefore, it opens the way to broadening the scope of the first passage time theory beyond the context of one-degree-of-freedom linear systems subjected to broadband excitations considered so far.

ACKNOWLEDGMENTS

First of all, I would like to express my deep gratitude to Professors Jean-Claude Golinval and Vincent Denoël. As supervisors, they have really helped me with their daily encouragement, their useful critiques and their support throughout this work.

Then, other important people have guided me these last months. On the one hand, I thank Hélène Vanvinckenroye for her availability, her precious advice and her constructive comments. On the other hand, I also thank the V2i company and, more particularly, Sébastien Hoffait and Jérôme Ligot, always available at the lab and who advised me a lot about the use of the LMS software and acquisition system.

At last, I do not forget all those who are not explicitly mentioned but who have contributed to the accomplishment of this work.

CONTENTS

Introduction **1**

1 Mathieu equation - State of the art and original developments **3**
1.1 Deterministic version of Mathieu equation 4
1.2 Stochastic version of Mathieu equation 8
1.2.1 Generalized Pontryagin equation for the n-th statistical moment 9
1.2.2 Undamped oscillator 10
1.2.3 Damped oscillator 14
1.2.4 New developments about the asymptotic behavior of the average first passage time of a damped oscillator in the three regimes 15
1.2.5 New developments about the mean square first passage time of damped systems . . 19

2 Experimental set-up **20**
2.1 Preliminary design 20
2.2 Set-up description 21
2.3 Measurement chain 23

3 Finite element modeling **27**
3.1 Modal analysis of the non-instrumented structure 28
3.1.1 Theoretical modal analysis 28
3.1.2 Experimental modal analysis 33
3.1.3 Model updating 40
3.2 Modal analysis of the instrumented structure 44
3.2.1 Experimental modal analysis 45
3.2.2 Model updating 45
3.2.3 Damping 50
3.3 Nonlinearities detection 52

4 Numerical study of first passage time **55**
4.1 From multiple-degree-of-freedom to single-degree-of-freedom equations of motion 55
4.1.1 Model reduction 55
4.1.2 Validity of the single-degree-of-freedom governing equation 57
4.1.3 Validity of the reduction for deterministic excitations 58
4.1.4 Validity of the reduction for stochastic excitations 60
4.2 Influence of narrow-band excitations on the first passage time 62

4.2.1 Introduction of the tools used in the study of narrow-band processes 62
4.2.2 Influence of the frequency band of the forced excitation 66
4.2.3 Influence of the frequency band of the parametric excitation 68
4.2.4 Damping and power spectral densities influence 69
4.3 Numerical study of first passage time conclusions 71

5 Experimental study of first passage time **72**
5.1 Experimental limitations 72
5.1.1 Nondimensionalization 72
5.1.2 Constraints on the parameters 73
5.2 Single-degree-of-freedom system first passage time 74
5.2.1 Constraints on the excitations 75
5.2.2 Linear Mathieu equation 75
5.2.3 Nonlinear Mathieu equation 80
5.3 Multi-degree-of-freedom system first passage time 81

Conclusions and perspectives **83**

Bibliography **87**

A Numerical generation of stochastic processes **90**
A.1 Power spectral density 90
A.1.1 Definition 90
A.1.2 Numerical computation 91
A.2 Random process generation 91
A.2.1 Broadband noise generation 91
A.2.2 Narrow-band noise generation 92

B Numerical integration of the equations of motion **94**

LIST OF FIGURES

1.1 Largest Floquet multiplier of the unforced Mathieu equation as a function of the amplitude and the pulsation of the parametric excitation . . . 6
1.2 Qualitative representation of the boundary between stable and unstable zones of the Mathieu equation as a function of the excitation frequency, the excitation amplitude and the damping . . . 6
1.3 Solutions of the undamped Mathieu equation with parametric excitation only . . . 7
1.4 Solutions of the damped Mathieu equation with parametric excitation only . . . 7
1.5 Solutions of Mathieu equation with forced excitation only . . . 8
1.6 Solutions of Mathieu equation with forced and parametric excitations . . . 8
1.7 Reduced average first passage time $U_1 S_u/4$ as a function of H_0^* and ΔH^* for an undamped system . . . 11
1.8 Linearity of the average first passage time in the incubation regime . . . 11
1.9 Reduced mean square first passage time $U_2 S_u^2/32$ as a function of H_0^* and ΔH^* for an undamped system . . . 13
1.10 Coefficient of variation CV as a function of H_0^* and ΔH^* for an undamped system . . . 13
1.11 Reduced average first passage time $U_1 S_u/4$ as a function of H_0^* and ΔH^* for damped systems with a equal to 0.5, 0.8, 1.5, 2, 3 and comparison with the undamped system . . . 15
1.12 Reduced average first passage time $U_1 S_u/4$ as a function of H_0^* and ΔH^* for damped systems characterized by $a = 0.5$, 1.5 and 2.5 . . . 16
1.13 Reduced mean square first passage time $U_2 S_u^2/32$ as a function of ΔH^* for different values of H_0^*: Monte Carlo simulations and analytical solution . . . 19
1.14 Reduced mean square first passage time $U_2 S_u^2/32$ as a function of H_0^* and ΔH^* for an undamped system ($a = 0$) and a damped system ($a = 0.5$) . . . 19

2.1 Schematic views of a simple pendulum in the gravity field with random excitation of its support (non-stiffened pendulum, stiffened pendulum and inverted pendulum) . . . 20
2.2 Schematic view of the structure that consists in a vertical strip pre-stressed by a mass and subjected to forced and parametric excitations . . . 22
2.3 Picture of the non-instrumented structure . . . 22
2.4 LMS SCADAS Mobile acquisition system . . . 24
2.5 LMS SCADAS Lab acquisition system . . . 24
2.6 Polytec laser transducer . . . 24
2.7 Laser beam of the laser transducer . . . 24
2.8 Impact hammer and force transducer . . . 25
2.9 Vibration Test System TV 50009 . . . 25
2.10 Impedance head . . . 25

2.11 Picture of the tested structure with the shakers mounted 26
2.12 Close-up on the mounting of the horizontal and vertical shakers 26

3.1 Model updating scheme 28
3.2 The seven first modes of vibration obtained with the initial finite element model 30
3.3 Natural frequencies normalized by the natural frequencies computed with 50 elements as a function of the number of elements 31
3.4 Excitation and measurement points 34
3.5 Power spectral density of a typical impact force performed with the vinyl tip 35
3.6 Frequency response function and coherence function corresponding to an excitation at point P9 and the measure of the response at point P2 36
3.7 Peak-picking method (fifth bending mode) 37
3.8 Circle-fit method (fifth bending mode) 37
3.9 Illustration of the reciprocity principle 38
3.10 Stabilization diagram of the LSCE method applied to the non-instrumented structure . . . 39
3.11 Argand diagrams of the six first bending modes (non-instrumented structure) 41
3.12 The six first bending modes of the non-instrumented structure identified with the LSFD method compared to the modes obtained with the finite element method 42
3.13 Auto-MAC matrix of the experimental bending modes (non-instrumented structure) 43
3.14 MAC matrix between the numerical modes (initial model) and the experimental modes (non-instrumented structure) 43
3.15 Global error on the natural frequencies as a function of the stiffness in rotation 44
3.16 MAC matrix between the numerical modes (updated model) and the experimental modes (non-instrumented structure) 44
3.17 Frequency response function measured at the drive point P9. 45
3.18 Stabilization diagram of the SSI method applied to the instrumented structure 46
3.19 Horizontal shaker picture 47
3.20 Horizontal shaker modeling 47
3.21 Close-up on the impedance head/structure interaction 48
3.22 The six first bending modes of vibration obtained in MATLAB with the updated model of the instrumented structure 49
3.23 MAC matrix between the numerical modes (updated model) and the experimental modes of the instrumented structure 50
3.24 Comparison of the frequency response functions (excitation at point P9, measurement at point P3) of the numerical finite element model and the experimental set-up 51
3.25 Envelope of the velocity of the structure as a function of the frequency for sine-sweep excitations of amplitudes 0.125, 0.25, 0.5, 1, 2 and 4 N. 52
3.26 Velocity at point P3 as a function of the frequency for sine-sweep excitations of amplitude 4 N in up and down senses 54
3.27 Time evolution of the velocity at point P3 for sine excitations of amplitude 4 N and frequencies 57 and 57.5 Hz. 54
3.28 Velocity at point P3 as a function of the frequency for sine-sweep excitations of amplitude 4 N in up and down senses and expected NLFR 54
3.29 Time evolution of the velocity at point P3 for sine excitation of amplitude 4 N and frequency 65 Hz. Illustration of the quasiperiodiciy nonlinear phenomenon 54

4.1 Comparison of the temporal responses of the single- and multi-DOF undamped motion equations to a forced excitation of amplitude 1 N and frequency f_0 59
4.2 Comparison of the temporal responses of the single- and multi-DOF undamped motion equations to a parametric excitation of amplitude 2 N and frequency $2f_0$ 59

4.3 Comparison of the temporal responses of the single- and multi-DOF damped motion equations to a forced excitation of amplitude 1 N and frequency $1.05 f_0$ 59
4.4 Comparison of the temporal responses of the single- and multi-DOF damped motion equations to a parametric excitation of amplitude 0.1 N and frequency $1.95 f_0$ 59
4.5 Comparison of the temporal responses of the single- and multi-DOF damped motion equations to a forced excitation of power spectral density $\tilde{S}_w = 10^{-4}$ N^2/Hz 61
4.6 Comparison of the temporal responses of the single- and multi-DOF damped motion equations to F_w of intensity $\tilde{S}_w = 10^{-4}$ N^2/Hz on $[0.8 f_0 ; 1.2 f_0]$ and F_u on $[0.8 f_0 ; 2.4 f_0]$ 61
4.7 Comparison of the reduced average first passage time $U_1 S_u/4$ maps obtained numerically and analytically for broadband excitations ($a = 0$, $S_u = 10^{-3}$, $S_w = 5 \cdot 10^{-4}$) 63
4.8 Comparison of the reduced mean square first passage time $U_2 S_u^2/32$ maps obtained numerically and analytically for broadband excitations ($a = 0$, $S_u = 10^{-3}$, $S_w = 5 \cdot 10^{-4}$) 63
4.9 Convergence of the reduced average first passage time $U_1 S_u/4$ at five distinct points of the map with the number of samples ($a = 0$, $S_u = 10^{-3}$, $S_w = 5 \cdot 10^{-4}$, u on $[0.1 f_0 ; 3 f_0]$ and w on $[0.8 f_0 ; 1.2 f_0]$) 64
4.10 Comparison of the reduced first passage time maps obtained numerically for narrow-band excitations (u on $[0.1 f_0 ; 3 f_0]$ and w on $[0.8 f_0 ; 1.2 f_0]$) and analytically for broadband excitations ($a = 0$, $S_u = 10^{-3}$, $S_w = 5 \cdot 10^{-4}$) 64
4.11 Histogram of the reduced first passage time ($H_0^* = -1.6$ and $\Delta H^* = 0.7$) and inverse Gaussian distribution fitted to the data 65
4.12 Second indicator (u on $[0.1 f_0 ; 3 f_0]$, w on $[0.8 f_0 ; 1.2 f_0]$, $a = 0$, $S_u = 10^{-3}$, $S_w = 5 \cdot 10^{-4}$) . 65
4.13 Comparison of the reduced average first passage time maps obtained numerically for broadband u and narrow-band w ($[0.9 f_0 ; 1.1 f_0]$) and analytically for broadband excitations ($a = 0$, $S_u = 10^{-3}$, $S_w = 5 \cdot 10^{-4}$) 67
4.14 Second indicator (broadband u, w on $[0.9 f_0 ; 1.1 f_0]$, $a = 0$, $S_u = 10^{-3}$, $S_w = 5 \cdot 10^{-4}$) . . . 67
4.15 Comparison of the reduced average first passage time maps obtained numerically for broadband u and narrow-band w ($[0.8 f_0 ; 1.2 f_0]$) and analytically for broadband excitations ($a = 0$, $S_u = 10^{-3}$, $S_w = 5 \cdot 10^{-4}$) 67
4.16 Second indicator (broadband u, w on $[0.8 f_0 ; 1.2 f_0]$, $a = 0$, $S_u = 10^{-3}$, $S_w = 5 \cdot 10^{-4}$) . . . 67
4.17 Indicator I at point $H_0^* = 10^{-1.5}$ and $\Delta H^* = 10^0$ as a function of the lower and upper bounds of the frequency band of the parametric excitation 69
4.18 Indicator I at point $H_0^* = 10^{-1.5}$ and $\Delta H^* = 10^0$ as a function of the parameters of the problem a, S_u and S_w 70
4.19 Indicator I as a function of S_u for $S_w = 10^{-2}$ and $a = 1.6$ 70

5.1 Power spectral densities of the forced and parametric excitations measured experimentally and reference power spectral densities 76
5.2 Fragment of the time evolution of the velocity measured at point P3 76
5.3 Power spectral density of the velocity measured at point P3 76
5.4 Fragment of the time evolution of the Hamiltonian 77
5.5 Three fragments of the measured experimental trajectory of the system in the phase plane and contours of the Hamiltonian 77
5.6 Reduced average first passage time $U_1 S_u/4$ as a function of H_0^* and ΔH^*. Comparison of the maps obtained experimentally and numerically for narrow-band excitations (F_u on $[0.77 f_0 ; 2.57 f_0]$, F_w on $[0.87 f_0 ; 1.13 f_0]$) and analytically for broadband excitations ($a = 132$, $S_w = 2.5 \cdot 10^{-10}$, $S_u = 1.8 \cdot 10^{-4}$) 78
5.7 Cross-sections of the reduced average first passage time map (Fig. 5.6(b)) for $H_0^* = 2 \cdot 10^{-2}$ and $H_0^* = 2 \cdot 10^{-3}$ 78

5.8 Reduced average first passage time $U_1 S_u/4$ as a function of H_0^* and ΔH^*. Comparison of the maps obtained experimentally for narrow-band excitations (F_u on $[0.77 f_0\,;1.27 f_0]$, F_w on $[0.87 f_0\,;1.13 f_0]$) and analytically for broadband excitations ($a = 108$, $S_w = 2.5 \cdot 10^{-10}$, $S_u = 2.2 \cdot 10^{-4}$) . . . 80
5.9 Reduced average first passage time $U_1 S_u/4$ as a function of H_0^* and ΔH^*. Comparison of the maps obtained experimentally and numerically for narrow-band excitations (F_u on $[0.77 f_0\,;1.27 f_0]$, F_w on $[0.87 f_0\,;1.13 f_0]$). $a = 29$, $S_w = 3 \cdot 10^{-9}$, $S_u = 8 \cdot 10^{-4}$. Nonlinear case . . . 81
5.10 Cross-sections of the average first passage time map in the incubation regime for $H_0^* = 5 \cdot 10^{-2}$ (in blue) and $H_0^* = 6 \cdot 10^{-3}$ (in green). Experimental data and linear regression: nonlinear case . . . 81
5.11 Average first passage time $\tilde{U}_1$ [s] as a function of H_0 and ΔH. Map obtained experimentally for broadband excitations (F_w on $[30\,;70]$ Hz, F_u on $[10\,;400]$). $\tilde{S}_w = 10^{-4}$ N^2/Hz, $\tilde{S}_u = 8 \cdot 10^{-6}$ N^2/Hz . . . 82
5.12 Cross-sections of the average first passage time map for $H_0 = 10^{-5}$ J and $H_0 = 10^{-5.5}$ J (multi-degree-of-freedom case) . . . 82
I Sheet metal coating process: metal sheet moving between two rollers at the translation speed v and subjected to tension . . . 84
II Tension measured experimentally on a plate during the coating process . . . 85
III Power spectral density of the tension measured experimentally on a plate during the coating process . . . 85
IV Power spectral densities of the forced and parametric excitations acting on a crane measured during wind tunnel tests . . . 85

A.1 Illustration of the Welch method for the computation of the power spectral density . . . 91
A.2 Illustrative stochastic force signals numerically generated and corresponding power spectral densities . . . 93
A.3 Fast Fourier transform of the narrow-band noise between 30 and 50 Hz generated by the second method ($S_F = 10^{-2}$ N^2/Hz, $f_s = 500$ Hz) . . . 93
A.4 Computation times of the two narrow-band process generation methods presented as a function of the length of the generated signal ($f_s = 500$ Hz) . . . 93

B.1 Newmark integration scheme for linear systems . . . 95

LIST OF TABLES

2.1 Geometrical properties of the structure 23
2.2 Material properties of the steel structure 23
2.3 Characteristics of the laser transducer 24
2.4 Characteristics of the impact hammer 25
2.5 Characteristics of the shakers 25
2.6 Characteristics of the impedance heads 25

3.1 Eigenfrequencies obtained with the initial finite element model (50 elements) 29
3.2 Eigenfrequencies obtained with the MATLAB finite element model when the stiffness is ignored and analytical eigenfrequencies of a straight tensioned cable 31
3.3 Coefficients λ_i for the eigenfrequencies of a single span straight beam for clamped-clamped boundary conditions 32
3.4 Eigenfrequencies obtained with the MATLAB finite element model with zero pre-stress of the structure and analytical eigenfrequencies of a single span straight beam 32
3.5 Eigenfrequencies obtained with the MATLAB finite element model and analytical eigenfrequencies of a pre-stressed single span beam clamped at its extremities 33
3.6 Eigenfrequencies identified with the frequency response function (preliminary data acquisition) 37
3.7 Comparison of the eigenfrequencies and damping ratios obtained with the LSCE method implemented in MATLAB and the PolyMAX method implemented in the LMS Test.Lab software 40
3.8 Comparison of the eigenfrequencies obtained from theoretical (initial model) and experimental (non-instrumented structure) modal analyses 41
3.9 Comparison of the eigenfrequencies obtained from theoretical (after updating of the model) and experimental modal analyses 44
3.10 Comparison of the eigenfrequencies and damping ratios of the instrumented structure obtained with the SSI method implemented in MATLAB and the PolyMAX method implemented in the LMS Test.Lab software 46
3.11 Comparison of the eigenfrequencies obtained from theoretical (non-instrumented structure) and experimental (instrumented structure) modal analyses 46
3.12 Equivalent parameters of the spring-mass system modeling the horizontal shaker 47
3.13 Mechanical and geometrical properties of the aluminum stinger 47
3.14 Comparison of the eigenfrequencies obtained from theoretical(updated model) and experimental modal analyses of the instrumented structure 48

INTRODUCTION

Many engineering problems involve systems subjected to both forced and parametric excitations. Parametric excitations differ from forced excitations since their action appears as a time varying modification of a system parameter. The dynamics of many such systems can be modeled by the linear Mathieu equation that, for a damped system, takes the general form

$$\ddot{x} + 2\xi\dot{x} + [1 + u(t)]\,x = w(t),$$

where $w(t)$ and $u(t)$ denote respectively the forced and parametric excitations. Applications of this equation are present in all fields of engineering. This equation can for instance model parametric vibrations of cables subjected to axial oscillations, some aero-elastic stability problems or electromagnetic phenomena in inhomogeneous media [21, 26, 32].

This equation has been widely studied in the deterministic case, *i.e.* when the forced and parametric excitations have known deterministic analytical expressions, in particular in the harmonic case, with the aim of characterizing its steady-state solution and its stability [9, 30]. In most realistic applications, however, the forced and parametric excitations are stochastic processes and the system is slightly damped, so that the system spends most of its time in a stochastic transient regime.

In the stochastic context, the classical stability theories are no longer relevant and the theory of first passage time has been developed as an efficient alternative. The first passage time can be defined as the amount of time required for a stochastic process to reach a given threshold for the first time when starting from a given initial state. This concept is not directly related to a stability criterion but answers the usual engineer's questions that can be expressed as "How much time does it take to [reach a given state starting from a given initial condition]?". This question can be customized by the reader in an infinite number of ways for a wide range of applications in engineering, but also in science, economics or industry: "How much time does it take for a disease to spread over?", "How much time does it take for a mechanical system to reach its limit state?","How much time does it take for the exchange rate of euro to U.S. dollar to reach a given value?", "How much time does it take to observe and measure an increase of 5°C at a weather station?", etc. Numerical studies, often based on Monte Carlo simulations, can provide a first and quick answer to these questions. However, a better insight into the problem is obtained by solving the stochastic equations analytically. Very recent developments using this analytical approach have highlighted the influence of some dimensionless groups and the existence of different behavioral regimes for the first passage time of single-degree-of-freedom systems governed by the linear Mathieu equation and subjected to broadband excitations [36, 37].

The analytical results have already been illustrated experimentally using a tower crane model tested in a wind-tunnel [35]. These experimental tests validated the existence of the different regimes but did not relate them to the physical parameters of the problem. The initial aim of this Master thesis is to design a new experimental set-up to observe and, hence, validate the existence of these different regimes. The objective is also to be able to predict the first passage time with the physical parameters of the structure. The complete process, from the structure design to the experimental validation, is conducted in this work. This report is divided into several parts that correspond to the different steps followed in the process.

The first part of the work summarizes the relevant background material about Mathieu equation in both deterministic and stochastic contexts and the principal theoretical results about first passage time. Some original contributions to these analytical results are also included. The second part is dedicated to the design of an experimental set-up for the validation of the first passage time theory. The different components of the measurement chain are also described. A finite element model of the structure is built in the third part. Experimental modal analysis performed on the real structure allows to update the numerical model to get a reliable model to be used in the sequel. The fourth and fifth parts constitute the heart of the work. They are devoted respectively to the numerical and the experimental studies of first passage time.

The numerical results discussed in this report are obtained with home made MATLAB [42] implementations of the different algorithms, methods and techniques that constitute the state of the art in the fields of modal analysis and stochastic dynamics. Some heavy calculations are also performed in Wolfram Mathematica [46]. The software SAMCEF Field developed by Siemens [43] is used to validate some results obtained with MATLAB. The LMS Test.Lab software, which is also developed by Siemens, is used for signal processing in all the experimental tests.

PART 1

MATHIEU EQUATION - STATE OF THE ART AND ORIGINAL DEVELOPMENTS

This first part of the work summarizes the theoretical background required to understand the studies described in the following parts. The first section describes the main results about the deterministic version of Mathieu equation. The second section focuses on the stochastic version of Mathieu equation and introduces the concept of first passage time. The main theoretical results related to first passage time are also summarized.

This work focuses on the study of a generalization of the Mathieu equation. For a single-degree-of-freedom damped system, the extended Mathieu equation considered here takes the general dimensionless form

$$\ddot{x}(t) + 2\xi\dot{x}(t) + [1 + u(t)]x(t) = w(t), \tag{1.1}$$

where x is the state variable, t is a dimensionless time and ξ is the damping coefficient. The right-hand side $w(t)$ is an external force applied to the system that will be referred to in the following as the forced excitation. By contrast, the function $u(t)$ is called the parametric excitation, as it induces variation in time of a parameter of the dynamical system (its stiffness in the current case). This excitation does not appear in the governing equation as an external force applied to the system. The deterministic, undamped and unforced version of (1.1) was first introduced in 1868 by the French mathematician Émile Mathieu when studying the vibrations of an elliptic membrane [24]. Even if (1.1) does not exactly correspond to the equation initially studied by Émile Mathieu and commonly called the Mathieu equation in the literature, it will be referred to in the following as the Mathieu equation to ease the reading of the report.

This equation can be used to model many physical problems in all fields of engineering. For instance, it describes the oscillations of a pendulum in the gravity field when its support is subjected to a vertical motion that causes its stiffness to vary in time [17]. This equation also allows to study the deflection of a cable subjected to axial oscillations at one of its ends [21]. The rotative equilibrium of a crane in a turbulent wind can also be modeled by this equation [35]. The linear stability of Faraday waves that occur when a container of liquid is periodically oscillating in the vertical direction can also be described by a Mathieu equation [29].

1.1 Deterministic version of Mathieu equation

The Mathieu equation has been widely studied in the particular case where the parametric excitation is deterministic, and often harmonic. The equation is then rewritten for the state variable $x(t)$ as

$$\ddot{x}(t) + 2\xi\dot{x}(t) + [1 + A_u \cos(\omega_u t)]x(t) = w(t), \tag{1.2}$$

where the stiffness of the oscillator varies at a pulsation ω_u with an amplitude A_u. The natural pulsation of this oscillator is $\omega_0 = 1$. The externally and parametrically excited oscillator is usually studied to determine the stability zones, the amplitude of the limit cycle oscillations or the steady-state solutions.

In the specific case without damping nor external excitation, the equation takes the simple form

$$\ddot{x}(t) + [1 + A_u \cos(\omega_u t)]x(t) = 0 \tag{1.3}$$

and corresponds to the equation initially studied by Émile Mathieu [24]. This equation can be rewritten as

$$\begin{bmatrix} \dot{x}_1 \\ \dot{x}_2 \end{bmatrix} = \mathbf{A}(t) \begin{bmatrix} x_1 \\ x_2 \end{bmatrix}, \tag{1.4}$$

where $x_1(t) = x(t)$, $x_2(t) = \dot{x}(t)$ and

$$\mathbf{A}(t) = \begin{bmatrix} 0 & 1 \\ -[1 + A_u \cos(\omega_u t)] & 0 \end{bmatrix} \tag{1.5}$$

is periodic with period $T = 2\pi/\omega_u$. According to Floquet theory [38], the solution does not need to be periodic but will, in general, be a linear combination of elementary solutions of the form

$$e^{\mu t} \begin{bmatrix} x_1(t) \\ x_2(t) \end{bmatrix}, \tag{1.6}$$

where $x_1(t)$ and $x_2(t)$ have period T and μ is a so-called Floquet exponent. The system has two such Floquet exponents μ_1 and μ_2 which may be complex. The Floquet exponents can be used to characterize the stability of the unforced Mathieu equation.

The Floquet exponents are related to the Floquet multipliers $\rho = e^{\mu T}$, which are the eigenvalues of the fundamental matrix

$$\mathbf{B} = \begin{bmatrix} x_1^{(1)}(T) & x_1^{(2)}(T) \\ \dot{x}_1^{(1)}(T) & \dot{x}_1^{(2)}(T) \end{bmatrix} \tag{1.7}$$

associated to the fundamental set of solutions

$$\begin{bmatrix} x_1^{(1)}(t) \\ x_2^{(1)}(t) \end{bmatrix}, \quad \begin{bmatrix} x_1^{(2)}(t) \\ x_2^{(2)}(t) \end{bmatrix} \tag{1.8}$$

of (1.4) generated by considering the initial conditions

$$\begin{bmatrix} x_1^{(1)}(0) \\ x_2^{(1)}(0) \end{bmatrix} = \begin{bmatrix} 1 \\ 0 \end{bmatrix} \quad \text{and} \quad \begin{bmatrix} x_1^{(2)}(0) \\ x_2^{(2)}(0) \end{bmatrix} = \begin{bmatrix} 0 \\ 1 \end{bmatrix}. \tag{1.9}$$

The Floquet multipliers ρ_1 and ρ_2 are such that

$$\rho_1\rho_2 = 1 \quad \text{and} \quad \rho_1 + \rho_2 = \frac{1}{2}\text{tr}(\mathbf{B}) = 2\phi, \tag{1.10}$$

so that

$$\rho_{1,2} = \phi \pm \sqrt{\phi^2 - 1}. \tag{1.11}$$

Different cases can be considered.

- If $\phi > 1$, then $\rho_1 > 1 > \rho_2 > 0$. The solution is unstable and has the form

$$\mathbf{x}(t) = c_1 e^{\mu_1 t}\mathbf{p}_1(t) + c_2 e^{-\mu_1 t}\mathbf{p}_2(t), \tag{1.12}$$

  where $\mathbf{p}_1(t)$ and $\mathbf{p}_2(t)$ have a period T.

- If $\phi = 1$, then $\rho_1 = \rho_2 = 1$. The solution is unstable and has the form

$$\mathbf{x}(t) = (c_1 + tc_2)\mathbf{p}_1(t) + c_2\mathbf{p}_2(t), \tag{1.13}$$

  where $\mathbf{p}_1(t)$ and $\mathbf{p}_2(t)$ have a period T.

- If $-1 < \phi < 1$, then $\rho = \exp(\pm j\sigma T)$ ($|\rho_1| = |\rho_2| = 1$). The solution is stable and pseudo-periodic and has the form

$$\mathbf{x}(t) = c_1\Re[e^{j\sigma t}\mathbf{p}(t)] + c_2\Im[e^{j\sigma t}\mathbf{p}(t)], \tag{1.14}$$

  where $\mathbf{p}(t)$ has a period T.

- If $\phi = -1$, then $\rho_1 = \rho_2 = -1$. The solution is unstable and has the form

$$\mathbf{x}(t) = (c_1 + tc_2)\mathbf{q}_1(t) + c_2\mathbf{q}_2(t), \tag{1.15}$$

  where $\mathbf{q}_1(t)$ and $\mathbf{q}_2(t)$ have a period $2T$.

- If $\phi < -1$, then $\rho_1 < -1 < \rho_2 < 0$. The solution is unstable and has the form

$$\mathbf{x}(t) = c_1 e^{\gamma t}\mathbf{q}_1(t) + c_2 e^{-\gamma t}\mathbf{q}_2(t), \tag{1.16}$$

  where $\mathbf{q}_1(t)$ and $\mathbf{q}_2(t)$ have a period $2T$.

Approximations of the boundary between stability and instability zones of the Mathieu equation can be found in the literature [38]. Here, the Floquet multipliers are computed numerically using Wolfram Mathematica. Fig. 1.1(a) shows the norm of the largest Floquet multiplier as a function of the parametric excitation amplitude A_u and pulsation ω_u. The solution becomes unstable and grows unbounded when a Floquet multiplier is larger than one. These parametric instabilities appear when the pulsation of the excitation is close to the critical pulsations

$$\omega_u^{(k)} = 2\frac{\omega_0}{k}, \qquad \forall k \in \mathbb{N}_0, \tag{1.17}$$

where ω_0 is the natural pulsation of the system. For small amplitude excitations, the most critical behavior is observed at twice the natural frequency of the system. The other unstable modes appear only in very narrow bands around the critical frequencies. In the unstable regions, the Floquet multipliers increase with the amplitude A_u of the excitation. Periodic solutions of period T and $2T$ occur at the boundary between the stable and unstable regions.

The same reasoning can be followed in the presence of damping. The damped Mathieu equation can be expressed as

$$\ddot{x}(t) + 2\xi\dot{x}(t) + [1 + A_u\cos(\omega_u t)]x(t) = 0. \tag{1.18}$$

This equation can be transformed into the undamped Mathieu equation

$$\ddot{y}(t) + [1 - \xi^2 + A_u\cos(\omega_u t)]y(t) = 0 \tag{1.19}$$

by defining

$$x(t) = e^{-\xi t}y(t). \tag{1.20}$$

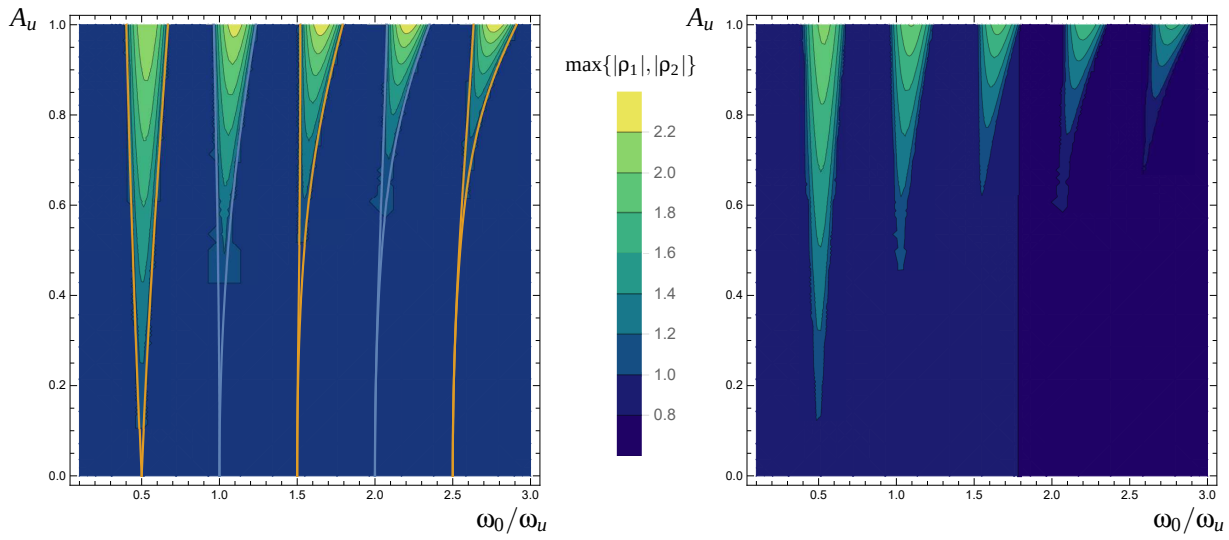

(a) Undamped case ($\xi = 0$).

(b) Damped case ($\xi = 0.02$).

FIGURE 1.1 - Largest Floquet multiplier of the unforced Mathieu equation (1.18) as a function of the amplitude and the pulsation of the parametric excitation.

For small values of the damping coefficient ξ, parametric instabilities still develop at the critical pulsations $\omega_u^{(k)}$ (1.17) but the Floquet multipliers are decreased by a factor $e^{-\xi T}$ (Fig. 1.1(b)). Therefore, parametric instabilities only occur for excitations with a sufficiently large amplitude. As schematized in Fig. 1.2 and pointed out by [21], damping has an erosive effect on the boundary of the instability regions. The amplitude of the parametric excitation required to trigger the parametric instability increases with k.

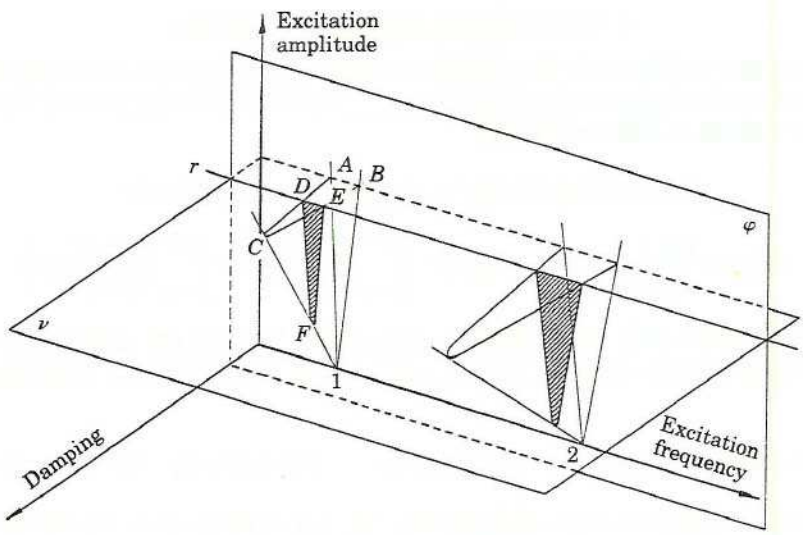

FIGURE 1.2 - Qualitative representation of the boundary between stable and unstable zones of the Mathieu equation as a function of the excitation frequency, the excitation amplitude and the damping [21].

Figs. 1.3 and 1.4 represent the time responses of the undamped and damped unforced Mathieu equations (1.3) and (1.18) to parametric excitations of amplitude $A_u = 0.2$. From Fig. 1.1, it is expected that the response is unstable for $\omega_u = 2\omega_0$ in the undamped case and for $\xi = 0.02$. It is indeed observed that the response grows exponentially in both cases. The growth is more rapid in the undamped case. For $\omega_u = 1.5\omega_0$, the response is stable. The effect of damping is clearly seen in Fig. 1.4(a).

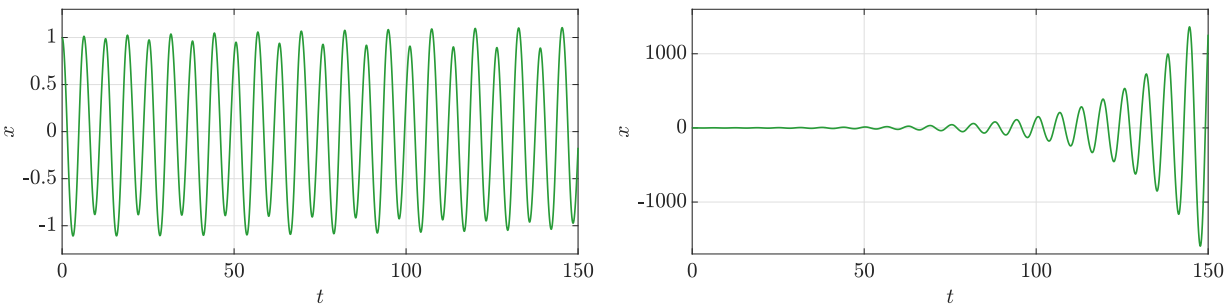

(a) Stable solution ($A_u = 0.2,\ \omega_u = 1.5\omega_0$).

(b) Unstable solution ($A_u = 0.2,\ \omega_u = 2\omega_0$).

FIGURE 1.3 - Solutions of the undamped Mathieu equation (1.3) with parametric excitation only.

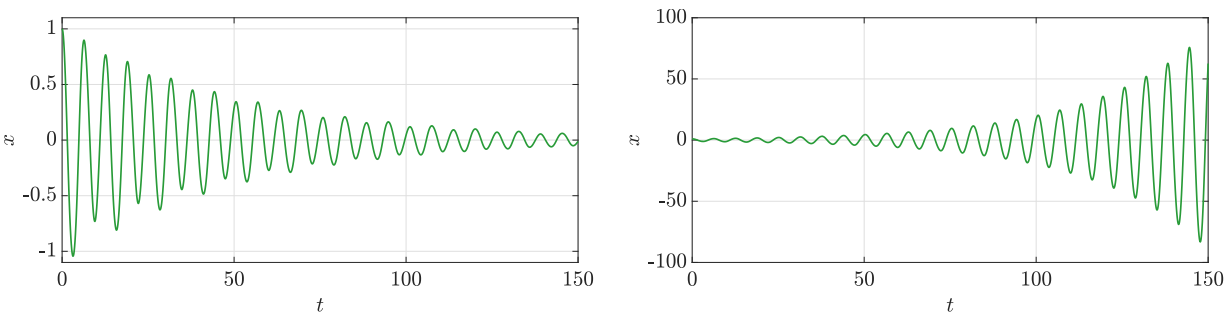

(a) Stable solution ($A_u = 0.2,\ \omega_u = 1.5\omega_0$).

(b) Unstable solution ($A_u = 0.2,\ \omega_u = 2\omega_0$).

FIGURE 1.4 - Solutions of the damped Mathieu equation (1.18) with parametric excitation only ($\xi = 0.02$).

When the oscillator is subjected to an external harmonic forced excitation, the governing equation writes

$$\ddot{x}(t) + 2\xi\dot{x}(t) + [1 + A_u\cos(\omega_u t)]x(t) = A_w\cos(\omega_w t) \tag{1.21}$$

and can no longer be studied with the Floquet theory. When only the forced excitation is considered ($A_u = 0$), the dynamics of the system shows the classical characteristics. For an undamped system excited at its natural frequency, the response grows linearly (Fig. 1.5(a)). In the damped case, the response eventually reaches an asymptotic value (Fig. 1.5(b)).

When the oscillator is subjected to both forced and parametric excitations, similar conclusions can be drawn. Both instabilities combine when the forced excitation has a pulsation $\omega_w = \omega_0$ and the parametric excitation a pulsation $\omega_u = 2\omega_0$ (Fig. 1.6(a)). Damping has still an erosive effect on the instability zones. A forced excitation characterized by a pulsation ω_w different from ω_0 has also an erosive effect on the instability zones. As shown in Fig. 1.6(b) for $\omega_w = 0.5\omega_0$ and $\omega_u = 2\omega_0$, the parametric instability is less pronounced when the forced excitation amplitude A_w increases.

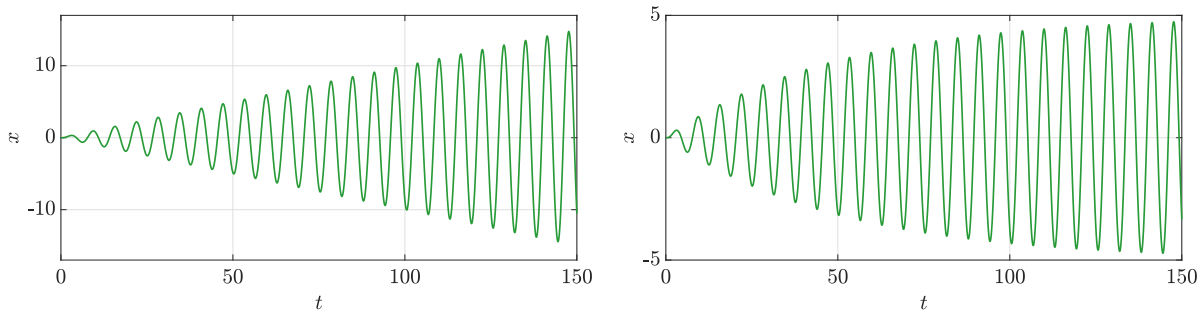

(a) Undamped solution ($\xi = 0$).

(b) Damped solution ($\xi = 0.02$).

FIGURE 1.5 - Solutions of Mathieu equation (1.21) with forced excitation only ($A_w = 0.2,\ \omega_w = \omega_0$).

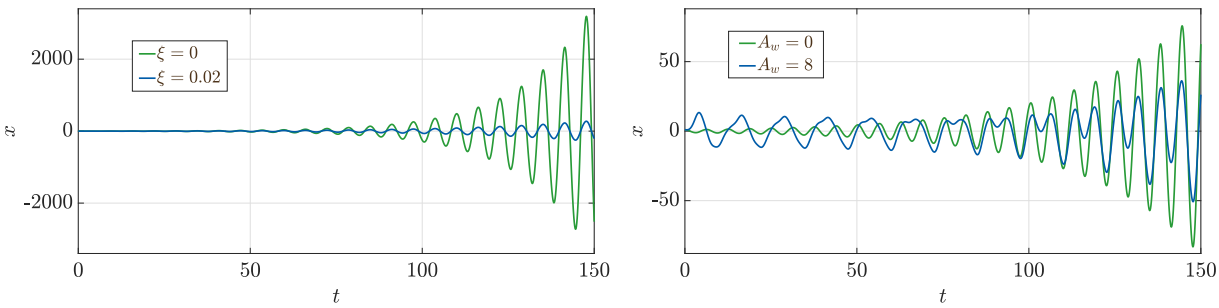

(a) $A_w = 0.2,\ \omega_w = \omega_0$.

(b) $\omega_w = 0.5\omega_0,\ \xi = 0.02$.

FIGURE 1.6 - Solutions of Mathieu equation (1.21) with forced and parametric excitations ($A_u = 0.2,\ \omega_u = 2\omega_0$).

1.2 Stochastic version of Mathieu equation

The generalized Mathieu equation of a damped system submitted to forced and parametric excitations takes the general form

$$\ddot{x} + 2\xi\dot{x} + [1 + u(t)]x = w(t), \tag{1.22}$$

with $x(t)$ the state variable function of the dimensionless time t, ξ the damping coefficient and $w(t)$ and $u(t)$ the forced and parametric excitations that are now random processes.

As in the deterministic case, the stochastic oscillator can also be studied with the aim to characterize the stability zones or steady-state solutions. However, when damping is absent or very small, these objectives have little interest since the system spends a long time in a stochastic regime. Accordingly, the problem has to be studied from a different point of view.

When damping is small, it is more interesting to study the time required for the system to reach a given energy level starting from a known initial condition. Such a problem is referred to in the literature as a first passage problem [33]. In a stochastic context (*i.e.* when the excitation is stochastic and/or when the parameters of the system vary in a random way), the first passage time is a random variable characterized by its probability density function. The complete statistical distribution of the first passage time is available for very few problems only. In order to characterize the distribution, the first statistical moments can be obtained numerically (through Monte Carlo simulations for instance) or, in some rare cases, analytically.

The next sections are devoted to the presentation of the main analytical results available to define the probability density function. This state of the art related to the stochastic version of the Mathieu equation is mainly based on two papers by H. Vanvinckenroye about the first passage time theory: [36] for the statement of the problem and the development of analytical expressions for the first moment of the first passage time and [37] for the development of analytical expressions for the second moment of the first passage time. Some original contributions are also added to these analytical results in sections 1.2.4 and 1.2.5.

1.2.1 Generalized Pontryagin equation for the n-th statistical moment

The energy balance of the governing equation (1.22) is obtained by time integration of the power fluxes

$$\int (\ddot{x} + 2\xi\dot{x} + [1+u(t)]x)\,\dot{x}dt = \int w\dot{x}dt, \tag{1.23}$$

which yields

$$\frac{\dot{x}^2}{2} + \frac{x^2}{2} + \int \left(2\xi\dot{x}^2 + ux\dot{x}\right) dt = \int w\dot{x}dt. \tag{1.24}$$

The Hamiltonian of the system is composed of a potential energy and a kinetic energy and is defined by

$$H = \frac{x^2}{2} + \frac{\dot{x}^2}{2}. \tag{1.25}$$

If the damping coefficient and the amplitudes of the excitations are small, *i.e.* if

$$\{\xi, u, w\} \ll 1, \tag{1.26}$$

the Hamiltonian evolves on a slow time scale since

$$\dot{H} = w\dot{x} - 2\xi\dot{x}^2 - ux\dot{x} \ll 1. \tag{1.27}$$

It can therefore be assumed that the energy is nearly constant along one period of oscillation, *i.e.* that the system is quasi-Hamiltonian. In the following, only quasi-Hamiltonian systems will be considered. When the system is not quasi-Hamiltonian, the steady-state regime is reached fast enough and the theory of first passage time is of limited interest.

The conservative system evolves along closed trajectories of constant Hamiltonian H. The period of revolution of a complete orbit of the unperturbed system ($u = w = \xi = 0$) is independent of the considered energy level H and is given by

$$T = 2\pi. \tag{1.28}$$

In order to derive an analytical equation characterizing the probability density function of the first passage time of an oscillator, the problem is first represented in the state-space by its Itô formulation for Markov times. Under the assumption of a quasi-Hamiltonian system, the stochastic averaging of the Itô equation over one revolution $T = 2\pi$ provides the averaged Itô equation governing the time-evolution of the Hamiltonian H [5]. The drift and diffusion coefficients $m(H)$ and $\sigma^2(H)$ can then be obtained as functions of the Hamiltonian H and the parameters of the problem. When the excitations $u(t)$ and $w(t)$ are Brownian δ-correlated noises of small amplitudes measured by their power spectral densities S_u and S_w (see appendix A for the definitions and conventions adopted in the current work), the drift and diffusion coefficients are given by

$$m(H) = \frac{H}{2}S_u + \frac{1}{2}S_w - 2\xi H \qquad \text{and} \qquad \sigma^2(H) = \frac{H^2}{2}S_u + HS_w. \tag{1.29}$$

Let $\mathcal{D}$ be a closed domain in the phase plane defined by $\mathcal{D} = \{H : 0 \leqslant H \leqslant H_c\}$ and an initial condition $H_0 \in \mathcal{D}$. The n-th statistical moment of the first passage time $U_n = E\left[t_1^n\right]$ $(n = 1, 2, 3, ...)$ to reach the boundary $\partial\mathcal{D}$ starting from the initial Hamiltonian H_0 is governed by the generalized Pontryagin equation [28]

$$\frac{1}{2}\sigma^2(H_0)\frac{d^2}{dH_0^2}U_n + m(H_0)\frac{d}{dH_0}U_n = -nU_{n-1}, \tag{1.30}$$

with $U_0 = 1$ and the boundary conditions

$$U_n(H_0) = 0 \quad \forall H_0 \in \partial\mathcal{D} \qquad \text{and} \qquad |U_n(0)| < \infty. \tag{1.31}$$

It is interesting to note that the governing equation is independent of the correlation between the parametric and forced excitation, *i.e.* independent of the cross-spectral density S_{uv}. Some analytical solutions of (1.30) have been recently derived in specific cases and show interesting behaviors of the first passage time of quasi-Hamiltonian systems [36, 37]. Those are discussed in the following sections.

1.2.2 Undamped oscillator

In the undamped case, the studied Mathieu equation can be written as

$$\ddot{x} + [1 + u(t)]x = w(t), \tag{1.32}$$

where $u(t)$ and $w(t)$ are Brownian δ-correlated noises of small intensities S_u and S_w.

Mean first passage time U_1

The mean first passage time of the system at an energy level H_c starting from an energy level H_0 is obtained by solving (1.30) for $n = 1$ and takes the simple form

$$U_1(H_0) = \frac{4}{S_u}\ln\left(\frac{H_c S_u + 2S_w}{H_0 S_u + 2S_w}\right) = \frac{4}{S_u}\ln\left(1 + \frac{\Delta H S_u}{H_0 S_u + 2S_w}\right), \tag{1.33}$$

where

$$\Delta H = H_c - H_0. \tag{1.34}$$

This solution is only valid for positive first passage times, *i.e.* for a target energy higher than the initial energy ($\Delta H \geqslant 0$). This expression presents two limiting cases without parametric or forced excitation.

When there is no parametric excitation, *i.e.* $S_u = 0$, the average first passage time becomes

$$U_1(H_0) = 2\frac{\Delta H}{S_w}. \tag{1.35}$$

The average first passage time varies linearly with the energy increment. This is referred to as an incubation regime. Increasing the forced excitation decreases the first passage time.

When there is no forced excitation, *i.e.* $S_w = 0$, the average first passage time becomes

$$U_1(H_0) = \frac{4}{S_u}\ln\left(\frac{H_c}{H_0}\right) = \frac{4}{S_u}\ln\left(1 + \frac{\Delta H}{H_0}\right). \tag{1.36}$$

The average first passage time scales with the ratio H_c/H_0 on a logarithmic scale. This is called the multiplicative regime. Increasing the parametric excitation decreases the first passage time.

These two limiting cases reflect that the parametric and forced excitations influence the dynamics of the problem in two distinct ways. As illustrated in section 1.1 when describing the instabilities observed for forced or parametric excitation only, this is also the case for deterministic excitations.

When both parametric and external forced excitations are considered, three regimes characterized by different behaviors of the average first passage time can be identified, depending on the relative values of the parameters S_u, S_w, H_0 and H_c. To ease the notation, the reduced groups

$$H_0^* = \frac{H_0 S_u}{2S_w} \quad \text{and} \quad \Delta H^* = \frac{\Delta H S_u}{2S_w} \tag{1.37}$$

are introduced. The average first passage time (1.33) takes the form

$$U_1 = \frac{4}{S_u} \ln\left(1 + \frac{\Delta H^*}{H_0^* + 1}\right). \tag{1.38}$$

Fig. 1.7 shows the ratio $U_1 S_u/4$ as a function of H_0^* and ΔH^*. The bottom left corner in the figure corresponds to the limiting case where there is no parametric excitation and the upper right corner to the limiting case where there is no forced excitation.

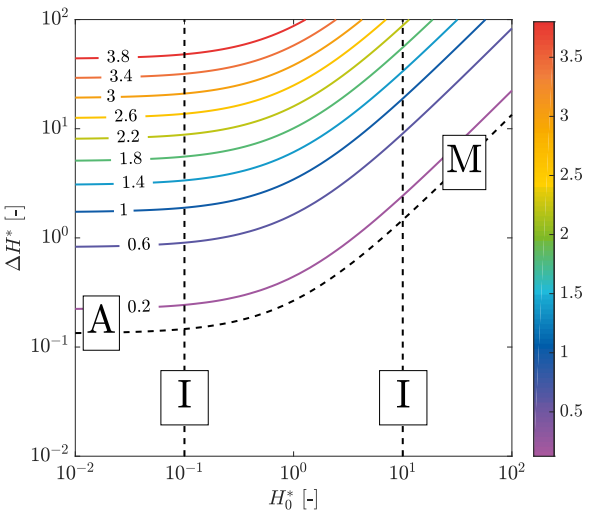

FIGURE 1.7 - Reduced average first passage time $U_1 S_u/4$ as a function of H_0^* and ΔH^* for an undamped system. Identification of the additive (A), multiplicative (M) and incubation (I) regimes.

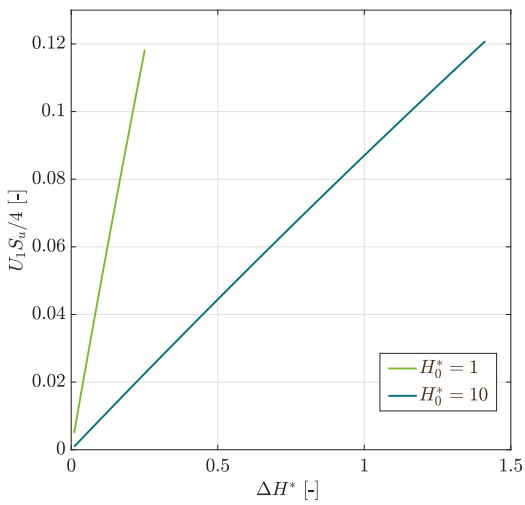

FIGURE 1.8 - Linearity of the average first passage time in the incubation regime. Cross-sections of the reduced average first passage time map (Fig. 1.7) for $U_1 < U_{1,\text{incub}}$ and H_0^* equal to 1 and 10.

The incubation regime is defined as the regime where the average first passage time may be linearized. This is the case when the argument of the logarithm is close to 1, *i.e.* when

$$\Delta H^* \ll H_0^* + 1. \tag{1.39}$$

In the incubation regime, the average first passage time may be written as

$$U_1 = \frac{4}{S_u} \frac{\Delta H^*}{H_0^* + 1} \tag{1.40}$$

and scales therefore linearly with ΔH^*. This approximation ceases to be valid when condition (1.39) is no longer met, *i.e.* for

$$U_1 \simeq \frac{4}{S_u}. \tag{1.41}$$

A characteristic incubation time $U_{1,\text{incub}}$ can therefore be defined by

$$U_{1,\text{incub}} := \frac{1}{2S_u}. \tag{1.42}$$

From a practical point of view, this means that the first passage time is proportional to ΔH^*, might be estimated by (1.40) and that the resulting estimate is valid provided it is shorter than $U_{1,\text{incub}}$. The incubation zone is located on the bottom of Fig. 1.7 and conveniently limited by the curve $U_1 S_u/4 = 1/8$. Fig. 1.8 highlights the behavior of the average first passage time in the incubation regime. It corresponds to cross-sections of the map for constant values of H_0^*. The linear dependency in ΔH^* can be clearly observed.

Expression (1.38) reveals the existence of two other regimes, respectively when H_0^* is large or small compared to 1. These two regimes overlap with the incubation regime as shown in Fig. 1.7.

If $H_0^* \gg 1$, the mean first passage is given by

$$U_1 = \frac{4}{S_u} \ln\left(1 + \frac{\Delta H^*}{H_0^*}\right). \tag{1.43}$$

This regime is called the multiplicative regime because the first passage time depends on the factor by which the initial energy is multiplied to obtain the target energy level. The mean first passage time is independent of the forcing excitation intensity S_w. This regime corresponds to the right part of Fig. 1.7 which shows oblique asymptotes of unit slopes.

If $H_0^* \ll 1$, the mean first passage time is independent of H_0^* and is given by

$$U_1 = \frac{4}{S_u} \ln\left(1 + \Delta H^*\right). \tag{1.44}$$

This regime is called the additive regime. The expected first passage time only depends on the energy increment ΔH^*. This regime corresponds to the left part of Fig. 1.7 which shows horizontal asymptotes.

Mean square first passage time U_2

The general form of the generalized Pontryagin equation (1.30) is the same for all orders n so that strong similarities are expected between the first and higher moments of the statistical distribution of the first passage time. For the undamped system governed by (1.32), the mean square first passage time $U_2 = E[t_1^2]$, solution of the Pontryagin equation (1.30) for $n = 2$, can be expressed in terms of the same reduced parameters H_0^* and ΔH^* by

$$\begin{aligned} U_2 = \frac{32}{S_u^2} \Bigg[& \mathcal{P}(1+H_0^*) - \mathcal{P}(1+H_0^*+\Delta H^*) + \ln(1+H_0^*+\Delta H^*) \ln\left(\frac{1+H_0^*+\Delta H^*}{H_0^*+\Delta H^*}\right) \\ & - \ln(1+H_0^*) \ln\left(\frac{1+H_0^*+\Delta H^*}{H_0^*}\right) + \ln\left(1 + \frac{\Delta H^*}{1+H_0^*}\right) \Bigg], \end{aligned} \tag{1.45}$$

where $\mathcal{P}$ stands for the real part of the polylogarithm of order 2 (the dilogarithm) and is defined for any real x by

$$\mathcal{P}(x) = \text{Re}\left[\text{Polylog}(2,x)\right] = -\text{Re}\left[\int_0^x \frac{\ln(1-t)}{t} dt\right]. \tag{1.46}$$

Fig. 1.9 shows the ratio $U_2 S_u^2/32$ as a function of H_0^* and ΔH^*. The asymptotic behaviors of the mean square first passage time in the three previously identified regimes can be developed.

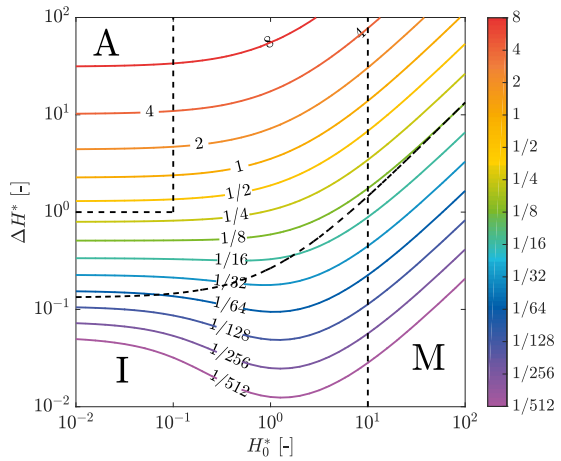

FIGURE 1.9 - Reduced mean square first passage time $U_2 S_u^2/32$ as a function of H_0^* and ΔH^* for an undamped system. Identification of the additive (A), multiplicative (M) and incubation (I) regimes.

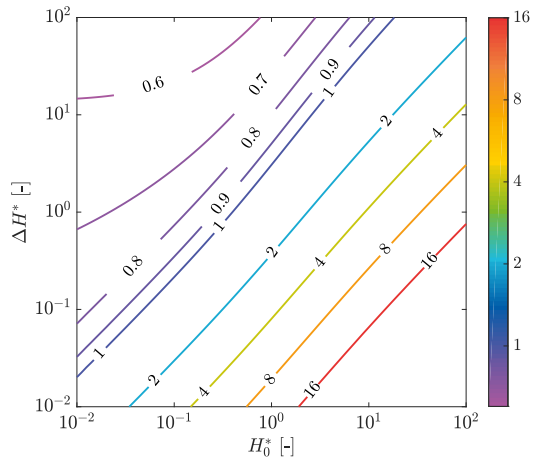

FIGURE 1.10 - Coefficient of variation CV as a function of H_0^* and ΔH^* for an undamped system.

In the incubation regime ($\Delta H^* \ll H_0^* + 1$), the mean square scales linearly with ΔH^* and is given by

$$U_2 = \frac{32}{S_u^2} \frac{\Delta H^*}{H_0^* + 1} \left[1 - \frac{\ln(1 + H_0^*)}{H_0^*} \right]. \tag{1.47}$$

For $H_0^* \gg 1$, the second order moment becomes

$$U_2 = \frac{32}{S_u^2} \left[\ln\left(1 + \frac{\Delta H^*}{H_0^*}\right) + \frac{1}{2} \ln\left(1 + \frac{\Delta H^*}{H_0^*}\right)^2 \right]. \tag{1.48}$$

This corresponds to the multiplicative regime previously identified. This expression only depends on the ratio $\Delta H^*/H_0^*$, which explains the unit slope in the right part of Fig. 1.9.

The additive regime is now restricted to the upper left corner ($H_0^* \ll 1$ and $\Delta H^* \gg 1$). The mean square writes

$$U_2 = \frac{32}{S_u^2} \left[-\frac{\pi^2}{6} + \frac{\ln(\Delta H^*)}{2\Delta H^*} \{4 + \Delta H^* \ln(\Delta H^*)\} + \ln(1 + \Delta H^*) \right] \tag{1.49}$$

and does not depend on H_0^*, which confirms the horizontal asymptote in Fig. 1.9. There is no overlap between the incubation and the additive regime.

Knowing the first and second moments of the statistical distribution of the first passage time, the variance is easily computed by

$$\sigma^2 = U_2 - U_1^2. \tag{1.50}$$

The spread in the distribution of the first passage time can be better evaluated with the coefficient of variation CV defined as

$$CV = \frac{\sqrt{\sigma^2}}{U_1}. \tag{1.51}$$

The coefficient of variation is represented in Fig. 1.10 as a function of H_0^* and ΔH^*. The lower the coefficient of variation, the smaller the sample size needs to be to provide estimates of the average first passage

time with small confidence intervals. The lowest coefficients of variation are found in the upper left corner, *i.e.* for the transition of a system from a low energy level to a much higher energy level. By contrast, the largest coefficients of variation are obtained in the bottom right corner, *i.e.* for small energy increments of a system starting from a high energy level. For $CV > \sqrt{2}/2$, the coefficient of variation depends in good approximation only on the ratio $\Delta H^*/H_0^*$. The behavior of the coefficient of variation is different in the upper left corner (additive regime).

1.2.3 Damped oscillator

In the damped case, the Mathieu equation takes the general form

$$\ddot{x} + 2\xi\dot{x} + [1 + u(t)]x = w(t). \tag{1.52}$$

Mean first passage time U_1

Solving the Pontryagin equation (1.30), the average first passage time can be expressed as

$$U_1 = \frac{4}{S_u(1-a)}\left[\frac{(1+H_0^*+\Delta H^*)^a - (1+H_0^*)^a}{a} - \int_{H_0^*}^{H_0^*+\Delta H^*} \frac{(1+t)^a - 1}{t} dt\right], \tag{1.53}$$

with the damping factor a defined by

$$a = \frac{8\xi}{S_u}. \tag{1.54}$$

This solution is only valid for positive first passage times since the Itô formulation on which it is based is only valid in this case. The two limiting cases corresponding to the absence of parametric or forced excitation can be discussed.

When there is no parametric excitation, *i.e.* $S_u = 0$, the average first passage time becomes

$$U_1(H_0) = -\frac{1}{2\xi}\ln\left(1 + \frac{\Delta H^*}{H_0^*}\right) + \frac{\mathrm{Ei}(aH_0^* + a\Delta H^*) - \mathrm{Ei}(aH_0^*)}{2\xi}, \tag{1.55}$$

with Ei the exponential integral defined by

$$\mathrm{Ei}(x) = \int_{-\infty}^{x} \frac{e^t}{t} dt. \tag{1.56}$$

The linear behavior identified in the undamped case disappears when damping is introduced.

When there is no forced excitation, *i.e.* $S_w = 0$, the average first passage time becomes

$$U_1 = \frac{4}{S_u(1-a)}\ln\left(1 + \frac{\Delta H^*}{H_0^*}\right). \tag{1.57}$$

It is interesting to note that, in this case, damping does not modify the form of the first passage time for $a < 1$. It still increases with the logarithm of the ratio H_c/H_0. This solution is positive as long as $a < 1$, which means that the energy of the system can increase, on average, if the damping ratio is below a certain threshold $\xi = S_u/8$.

Fig. 1.11 shows the reduced average first passage time $U_1 S_u/4$ as a function of H_0^* and ΔH^* for different values of a. The three regimes identified in the undamped case are recovered in the figure. In the additive regime, damping tends to increase the average first passage time. In the multiplicative regime, damping changes the slope of the iso-time curves. In the whole map, increasing damping increases the first passage time as expected. Details about the asymptotic behaviors of the average first passage time in the three regimes can be found in section 1.2.4.

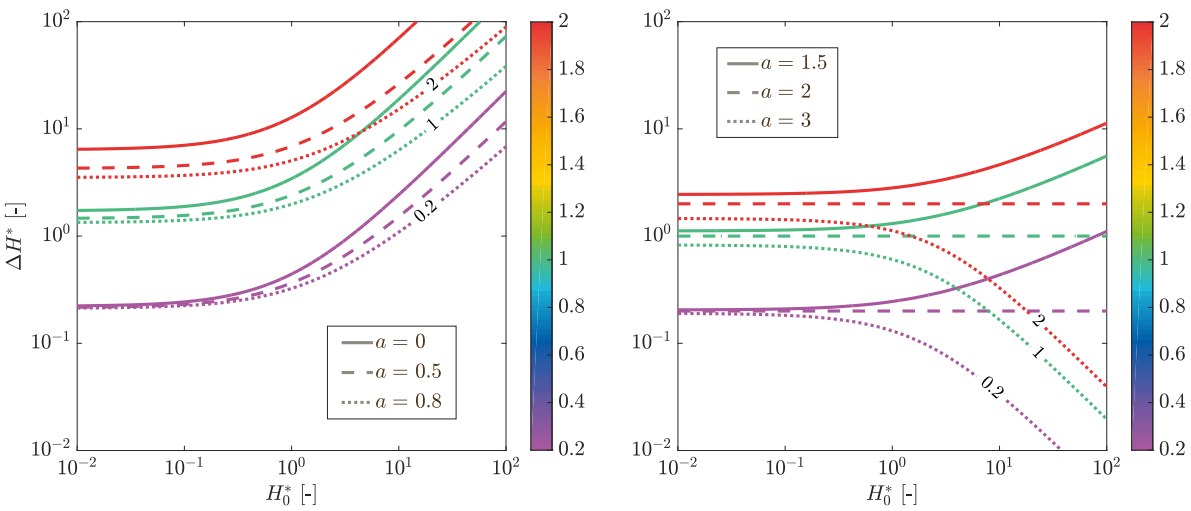

FIGURE 1.11 - Reduced average first passage time $U_1 S_u/4$ as a function of H_0^* and ΔH^* for damped systems with a equal to 0.5, 0.8, 1.5, 2, 3 and comparison with the undamped system.

Mean square first passage time U_2

No general analytical results related to the mean square first passage time of a damped system have been developed up to now. Section 1.2.5 presents some personal contributions to the analytical developments for specific damping conditions.

1.2.4 New developments about the asymptotic behavior of the average first passage time of a damped oscillator in the three regimes

In this section, the asymptotic behaviors of the mean first passage time of a damped system are derived in the three regimes. The limits of the different regimes are also estimated. The analytical developments are carried out using Wolfram Mathematica.

The general expression of the mean first passage time is given by (1.53). The integral appearing in the definition of U_1 can be written in terms of the hypergeometric function ${}_2F_1$ [22] as

$$\int_{H_0^*}^{H_0^*+\Delta H^*} \frac{(1+t)^a}{t} dt = \frac{(1+H_0^*+\Delta H^*)^{1+a}}{a(H_0^*+\Delta H^*)} {}_2F_1\left(1,1,1-a,-\frac{1}{H_0^*+\Delta H^*}\right) - \frac{(1+H_0^*)^{1+a}}{aH_0^*} {}_2F_1\left(1,1,1-a,-\frac{1}{H_0^*}\right). \quad (1.58)$$

Fig. 1.12 shows the reduced average first passage time $U_1 S_u/4$ as a function of H_0^* and ΔH^* for different values of a.

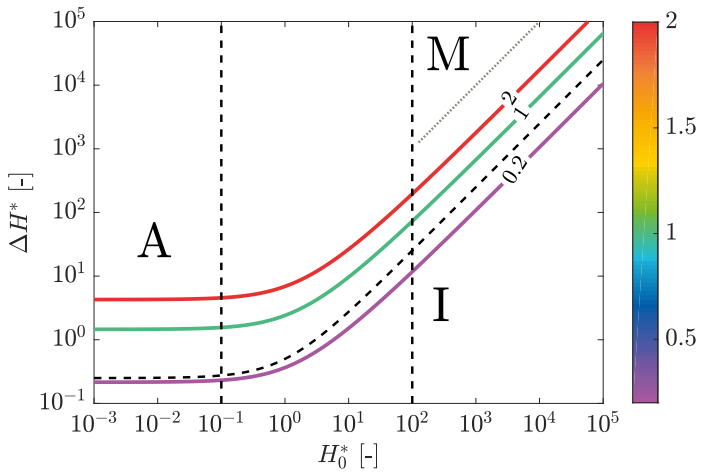

(a) $a = 0.5$.

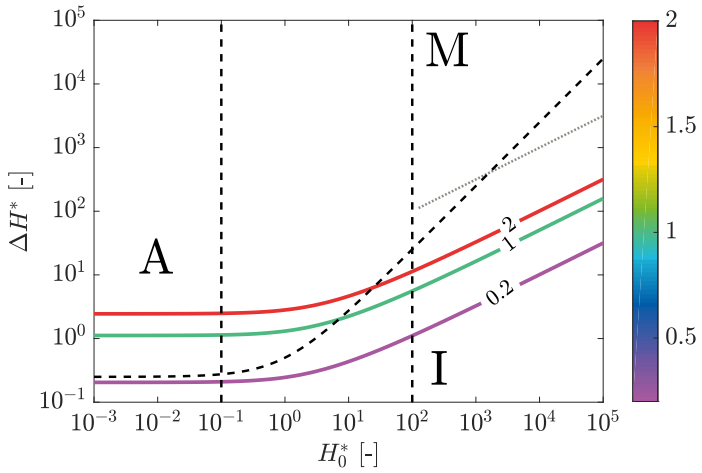

(b) $a = 1.5$.

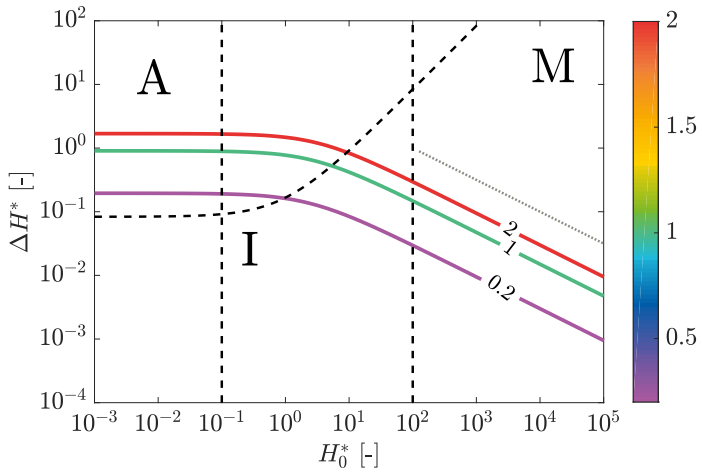

(c) $a = 2.5$.

FIGURE 1.12 - Reduced average first passage time $U_1 S_u/4$ as a function of H_0^* and ΔH^* for damped systems characterized by $a = 0.5$, 1.5 and 2.5. Identification of the additive (A), multiplicative (M) and incubation (I) regimes. Dotted gray lines indicate the asymptotic behavior in the multiplicative regime.

Additive regime

The additive regime is characterized by the fact that the mean first passage time does not depend on the initial level of energy H_0^*. The following developments show that this is the case when $H_0^* \ll 1$. The corresponding asymptotic value is also derived.

Since, for $a \neq 0$,

$$ {}_2F_1\left(1,1,1-a,-\frac{1}{x}\right) \sim ax\ln x, \qquad (x \to 0), \tag{1.59} $$

it comes

$$ \int_{H_0^*}^{H_0^*+\Delta H^*} \frac{(1+t)^a}{t}dt \sim \frac{(1+\Delta H^*)^{1+a}}{a\Delta H^*}{}_2F_1\left(1,1,1-a,-\frac{1}{\Delta H^*}\right) - \ln H_0^*, \qquad (H_0^* \to 0), \tag{1.60} $$

and eventually

$$ U_1 \sim \frac{4}{S_u(1-a)}\left[\ln\Delta H^* + \frac{(1+\Delta H^*)^a - 1}{a} - \frac{(1+\Delta H^*)^{1+a}}{a\Delta H^*}{}_2F_1\left(1,1,1-a,-\frac{1}{\Delta H^*}\right)\right], \quad (H_0^* \to 0). \tag{1.61} $$

This result shows that the mean first passage time tends to be independent of H_0^* when the initial energy level is small. This behavior can be observed in Fig. 1.12 where horizontal asymptotes appear for $H_0^* \ll 1$. Note that this result is not valid if $a = 0$ or $a = 1$ since (1.53) and/or (1.59) must be adapted in these cases.

Multiplicative regime

In the multiplicative regime, the first passage time depends on the ratio of the target energy and the initial energy. It is shown here that this is the case for $H_0^* \gg 1$.

The hypergeometric function behaves asymptotically as

$$ {}_2F_1(1,1,1-a,x) \sim 1 + \frac{x}{1-a} + O(x^2), \qquad (x \to 0). \tag{1.62} $$

Therefore, when $H_0^* \gg 1$, the integral in (1.53) can be approximated by

$$ \begin{aligned} \int_{H_0^*}^{H_0^*+\Delta H^*} \frac{(1+t)^a}{t}dt \sim{}& \frac{(1+H_0^*+\Delta H^*)^{1+a}}{a(H_0^*+\Delta H^*)}\left[1 - \frac{1}{(1-a)(H_0^*+\Delta H^*)}\right] \\ &- \frac{(1+H_0^*)^{1+a}}{aH_0^*}\left[1 - \frac{1}{(1-a)H_0^*}\right], \quad (H_0^* \to \infty). \end{aligned} \tag{1.63} $$

This leads to

$$ U_1 \sim \frac{4}{S_u(1-a)}\left[\frac{\Delta H^*}{H_0^*} - \frac{\Delta H^*}{(H_0^*)^{2-a}}\right], \qquad (H_0^* \to \infty). \tag{1.64} $$

The dominant behavior therefore depends on the value of a. If $a < 1$, one has

$$ U_1 \sim \frac{4}{S_u(1-a)}\frac{\Delta H^*}{H_0^*}, \qquad (H_0^* \to \infty). \tag{1.65} $$

In the first passage time map (with axes in logarithmic scale), this behavior appears as oblique asymptotes with unit slope (Fig. 1.12(a)). If $a > 1$, then

$$ U_1 \sim \frac{4}{S_u(a-1)}\frac{\Delta H^*}{(H_0^*)^{2-a}}, \qquad (H_0^* \to \infty), \tag{1.66} $$

and oblique asymptotes with slope $2-a$ are observed in the first passage time map. These asymptotes have therefore positive slopes for $a < 2$ (Fig. 1.12(b)) and negative slopes for $a > 2$ (Fig. 1.12(c)).

Incubation regime

In the incubation regime, the first passage time evolves linearly with ΔH^*. This is the case when $\Delta H^* \ll 1$. The two terms of the general expression (1.53) become

$$\frac{(1+H_0^*+\Delta H^*)^a-(1+H_0^*)^a}{a} \sim (1+H_0^*)^{a-1}\Delta H^* - \frac{1}{2}(1-a)(1+H_0^*)^{a-2}(\Delta H^*)^2 + O(\{\Delta H^*\}^3), \qquad (\Delta H^* \to 0), \quad (1.67)$$

and

$$\int_{H_0^*}^{H_0^*+\Delta H^*} \frac{(1+t)^a-1}{t}dt \sim \Delta H^* \frac{(1+H_0^*)^a-1}{H_0^*} + \frac{(\Delta H^*)^2}{2(H_0^*)^2}\left[1-(1+H_0^*)^a+aH_0^*(1+H_0^*)^{a-1}\right] + O(\{\Delta H^*\}^3), \qquad (\Delta H^* \to 0), \quad (1.68)$$

so that

$$U_1 \sim \frac{4\Delta H^*}{S_u(1-a)H_0^*}\left[H_0^*(1+H_0^*)^{a-1}-(1+H_0^*)^a+1\right] = \frac{4\Delta H^*}{S_u(1-a)H_0^*}\left[1-(1+H_0^*)^{a-1}\right]. \quad (1.69)$$

This expression is positive whatever the value of a.

In (1.67), the second order term can be neglected with respect to the term in ΔH^* if

$$\left|(1-a)(1+H_0^*)^{a-2}(\Delta H^*)^2\right| \ll \left|(1+H_0^*)^{a-1}\Delta H^*\right|, \quad (1.70)$$

i.e. if

$$|1-a|\frac{\Delta H^*}{(1+H_0^*)} \ll 1. \quad (1.71)$$

In (1.68), the second order term can be neglected with respect to the term in ΔH^* in the evaluation of the integral if

$$\frac{\Delta H^*}{H_0^*}\left|\frac{aH_0^*(1+H_0^*)^{a-1}}{(1+H_0^*)^a-1}-1\right| \ll 1. \quad (1.72)$$

The first condition (1.71) is always more restrictive than the second one (1.72) so that the incubation regime can be observed for values of ΔH^* and H_0^* such that

$$|1-a|\frac{\Delta H^*}{(1+H_0^*)} \ll 1. \quad (1.73)$$

For values of a less than 1, this domain can be approached by

$$U_1 < \frac{1}{2S_u(1-a)} \quad (1.74)$$

and the boundary of the incubation region can therefore be described by a curve of constant reduced average first passage time as for undamped systems. For values of a greater than 1, the limit does not follow a curve of equal mean first passage time. The domain can be approached by

$$U_1 < \frac{1}{2S_u(1-a)|1-a|}\frac{(1+H_0^*)-(1+H_0^*)^a}{H_0^*}. \quad (1.75)$$

The limits of the incubation regime are represented in Fig. 1.12 for different values of a. For $a = 0.5$, the limit can indeed be approached by a curve of constant value of $U_1S_u/4$. For $a = 1.5$ and $a = 2.5$, the limit does not follow a curve of the map.

1.2.5 New developments about the mean square first passage time of damped systems

The mean square first passage time U_2 of a damped system is obtained by solving the Pontryagin equation (1.30) for $n = 2$. Compact solutions can be found with Wolfram Mathematica when $a = k + 1/2$ with k integer. Indeed, for such a, the hypergeometric functions appearing in the solution of the Pontryagin equation can be easily expressed with logarithm functions.

For instance, introducing the variables $X = \sqrt{1+H_0^*}$ and $Y = \sqrt{1+H_0^*+\Delta H^*}$ to simplify the expression, the mean square of a damped oscillator characterized by $a = 0.5$ writes

$$U_2 = \frac{512}{S_u^2}\left[\mathcal{P}\left(\frac{1+X}{2}\right) - \mathcal{P}\left(\frac{1+Y}{2}\right) - \ln(1+X) + \ln(1-X)\left(\ln\{1+X\} - \ln 2\right)\right. \tag{1.76}$$
$$\left. + \ln 2 \cdot \ln(1-Y) + \ln(1+Y)\left(1 + 2\,\mathrm{atanh}\{Y\} - \ln\{1+X\}\right)\right],$$

where $\mathcal{P}$ is defined by (1.46).

This analytical result can be compared with the mean square first passage time U_2 obtained numerically with Monte Carlo simulations of the oscillator. The different curves of Fig. 1.13 correspond to different initial energy levels H_0^*. A good match is observed between the analytical and numerical results.

The mean square first passage time map is represented in Fig. 1.14 for $a = 0.5$ and compared to the undamped case. Even if a large shift between the curves is observed, the general behavior of the mean square first passage time is recovered for damped systems. The different regimes are also present. For small initial energy levels, $U_2 S_u^2/32$ does not depend on H_0^*. This corresponds to the additive regime. For large initial energy levels, the curves show the same slope. The incubation regime can also be highlighted by looking at Fig. 1.13. For small ΔH^*, the mean square first passage time evolves linearly with the energy increment.

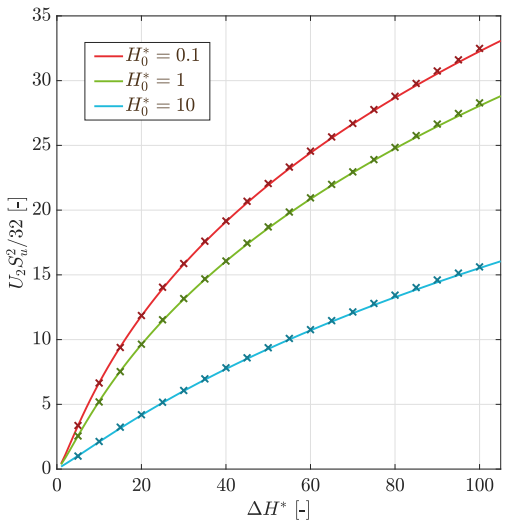

FIGURE 1.13 - Reduced mean square first passage time $U_2 S_u^2/32$ as a function of ΔH^* for different values of H_0^*. Monte Carlo simulations (cross markers) and analytical solution (full lines).

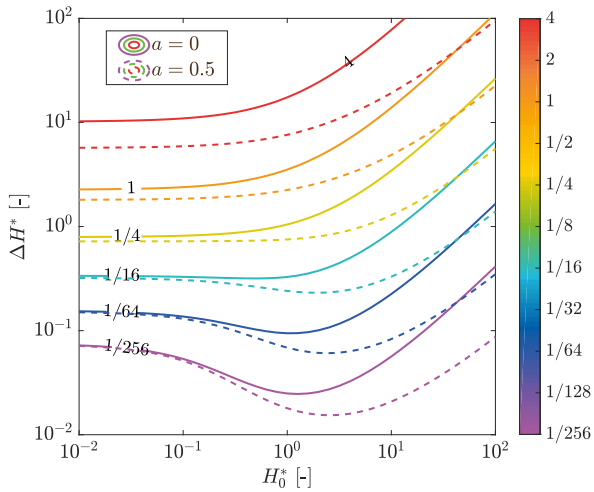

FIGURE 1.14 - Reduced mean square first passage time $U_2 S_u^2/32$ as a function of H_0^* and ΔH^* for an undamped system ($a = 0$) and a damped system ($a = 0.5$).

PART 2

EXPERIMENTAL SET-UP

This second part of the work is dedicated to the design of the experimental set-up used to illustrate the first passage time theory. In the first section, the design of the set-up is described and justified. Then, the real set-up is described in detail and the geometrical and physical properties of the structure are carefully identified. The measurement chain used in all the experimental tests is described in the last section.

2.1 Preliminary design

The final objective of the experimental set-up is to validate the existence of the different regimes for the first passage time. As explained in section 1.2, the theory studied is based on the one-degree-of-freedom Mathieu equation. This first section therefore aims at designing a structure governed by the Mathieu equation, *i.e.* subjected to an external forced excitation and a parametric excitation that modifies the stiffness of the dynamical structure. It will be shown further (section 4.1) how the assumption of a single-degree-of-freedom system can be verified in good approximation with a real intrinsically multi-degree-of-freedom structure.

It was initially suggested to study the oscillations of a simple pendulum of mass m and length ℓ in the gravity field when the pendulum is excited by a random motion of its support (Fig. 2.1, left). A horizontal excitation (perpendicular to the pendulum at rest) of its support $\ddot{x}_0$ can be seen as the forced excitation $w(t)$ in Mathieu equation (1.22). A vertical excitation (aligned with the pendulum at rest) $\ddot{y}_0$ makes the stiffness of the pendulum vary in time and therefore constitutes the parametric excitation $u(t)$.

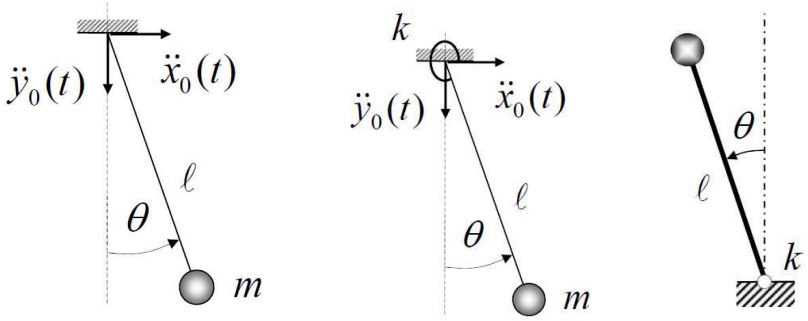

FIGURE 2.1 - Schematic views of a simple pendulum in the gravity field with random excitation of its support (left: non-stiffened pendulum, middle: stiffened pendulum, right: inverted pendulum).

The small oscillations θ of the pendulum around its stable equilibrium position $\theta = 0$ are governed by

$$m\ell^2\ddot{\theta} + c\ell\dot{\theta} + [mg\ell + m\ddot{y}_0\ell]\,\theta = -m\ddot{x}_0\ell. \tag{2.1}$$

Introducing the characteristic time $T = \sqrt{\ell/g}$, the equation of motion writes in dimensionless form

$$\theta'' + \frac{c}{m\sqrt{\ell g}}\theta' + \left[1 + \frac{\ddot{y}_0}{g}\right]\theta = \frac{-\ddot{x}_0}{g}. \tag{2.2}$$

Numerical simulations show, however, that such a set-up is not feasible from a practical point of view because it does not allow to reach a Hamiltonian $H = \theta^2/2 + \theta'^2/2$ larger than 10^{-2} (which is required to observe the different regimes of the first passage time) in a reasonable amount of time. In order to have sufficiently small first passage times, prohibitively large forces have to be applied or the natural frequency of the pendulum has to be increased by decreasing its length ℓ down to a few millimeters. This second solution would require very sensitive transducers, which are not available at the lab, to measure the mass position with accuracy. The same conclusions hold for an inverted pendulum or a stiffened pendulum (Fig. 2.1, middle and right). Moreover, such a set-up does not allow to extend the theory for multi-degree-of-freedom systems since a pendulum is fundamentally designed to be a single-degree-of-freedom system.

After careful consideration of the problem, an experimental set-up consisting in a vertical strip pre-stressed by a mass has been developed. A schematic representation of the set-up is given in Fig. 2.2. A horizontal force (perpendicular to the strip) F_w applied to the structure can play the role of the forced excitation $w(t)$ of Mathieu equation (1.22). The shakers used to excite the structure are characterized by a limited stroke and a limited velocity. In order to limit the amplitude of displacements of the strip where the shaker acts and therefore to avoid any impedance mismatch that arises when the shaker just follows the movement of the structure, the strip is excited sufficiently close to the bottom fixation. The parametric excitation $u(t)$ can be created by a vertical force F_u applied at the bottom end of the strip, below the pre-stress mass. Such a force induces variations in time of the strip stiffness since it modifies the pre-stress of the strip. The initial pre-stress by the mass m is obviously essential to avoid the instability of the strip.

The structure is made of carbon steel. The strip is chosen among those provided by the manufacturer Hasberg [40], specialist in steel strip. A strip with thickness 0.4 mm and width 25 mm is selected. The strip is clamped at its top end. At its bottom end, a lateral guide constrains the strip to move only in the vertical direction (Fig. 2.2).

2.2 Set-up description

This section aims at characterizing in detail the experimental set-up. The geometrical properties of the strip and its material properties are identified with accuracy. A picture of the experimental set-up in the lab is provided in Fig. 2.3.

As a first step, the geometrical properties of the structure are carefully determined. The length of the strip is measured. It is also checked that the width and the thickness of the steel strip correspond to the values given in the data sheet of Hasberg manufacturer [40]. The pre-stress mass is also accurately weighed. The properties are given in Table 2.1.

Then, the material properties of the steel that composes the strip have to be accurately identified. Two 30 cm samples of the strip are weighted to estimate the carbon steel density. The value $\rho = 7\,767\ \mathrm{kg/m^3}$ found is in good agreement with the density of traditional carbon steels. The value of the Poisson ratio is chosen as the Poisson ratio of usual carbon steels [2]. The material properties used in the following of the study are summarized in Table 2.2.

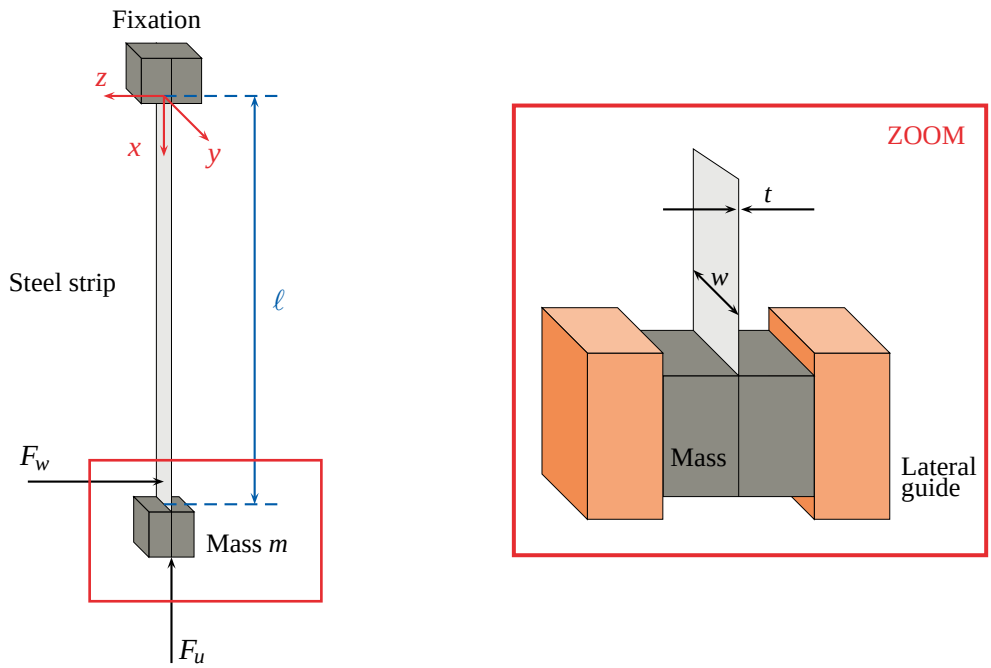

FIGURE 2.2 - Schematic view of the structure that consists in a vertical strip pre-stressed by a mass and subjected to forced and parametric excitations F_w and F_u.

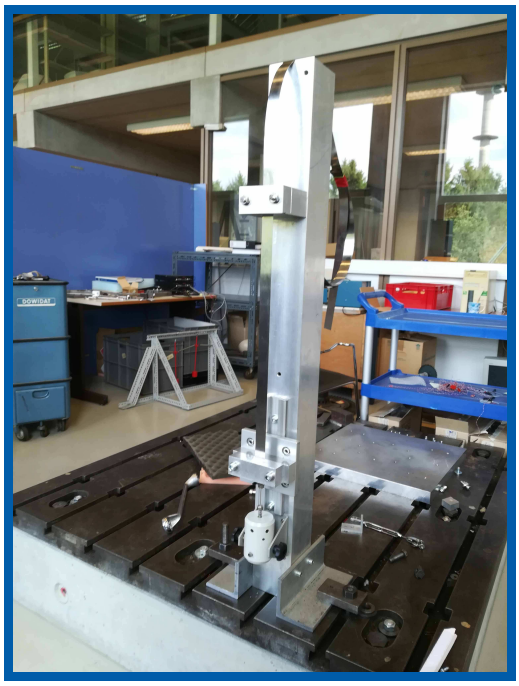

FIGURE 2.3 - Picture of the non-instrumented structure.

Parameter	*Symbol*	*Value*	*Units*
Length	ℓ	50.1	cm
Width	w	25	mm
Thickness	t	0.4	mm
Pre-stress mass	m	1.816	kg

TABLE 2.1 - Geometrical properties of the structure.

Parameter	*Symbol*	*Value*	*Units*
Density	ρ	7767	kg/m^3
Young's modulus	E	206	GPa
Poisson's ratio	ν	0.33	[-]

TABLE 2.2 - Material properties of the carbon steel structure.

Two different methods are used to get an accurate estimate of the Young's modulus. The two methods are applied on samples at ambient temperature, which corresponds to the conditions of the experimental tests described further. On the one hand, vibration properties of the strip are exploited. The strip sample is suspended at a stand by means of two small rigidity elastics. An accelerometer is glued on the sample and the sample is impacted using an impact hammer. In order to excite and measure a maximum of modes of the strip sample, vibration nodes have to be avoided for the impact and the response measurement: the measurement point and the excitation point are chosen at the two ends of the sample. This impact test allows to evaluate the first natural frequencies of the strip sample. A finite element model of a free-free beam with a concentrated mass (equal to the accelerometer mass) at the location of the accelerometer is then built. The Young's modulus is determined as the one that minimizes in a least square sense the error between the experimental natural frequencies and the natural frequencies of the finite element model. It is given by $E = 201$ GPa. On the other hand, a direct measure of the Young's modulus is obtained with tensile tests. Three tensile tests are performed on a single 30 cm sample at the *Laboratoire de Mécanique des Matériaux & Structures* of the University of Liège [44]. A mean Young's modulus $E = 206$ GPa (standard deviation of 1.45 GPa) is found. The first method based on the experimental measurement of the modal properties of the sample is less accurate than the second one because it relies on the assumptions and simplifications of the numerical model, for instance regarding the boundary conditions. It provides, however, an estimate of E close to the one determined with the tensile tests. In the following, the Young's modulus is taken equal to 206 GPa. This value is in agreement with usual values of Young's modulus of carbon steels [2].

2.3 Measurement chain

Before going further in the analysis, the main components of the measurement chain are described. All the experimental tests are carried out at the *LTAS - Vibrations et Identification des Structures* (LTAS-VIS) laboratory unit of the Department of Aerospace and Mechanical engineering at the University of Liège [41].

The data acquisition and signal processing are carried out using the LMS Test.Lab software and the LMS SCADAS Mobile and LMS SCADAS Lab acquisition systems [43]. The acquisition systems are shown in Figs. 2.4 and 2.5. The software provides a complete portfolio of testing solutions. As it will be explained further, two different tools of the software are used: namely Test.Lab Structures Acquisition for the modal analysis and Test.Lab Environmental for the structure testing and the first passage time study.

Because the studied structure is very light, it is important to avoid modifying its mass by adding accelerometers on it. The response (in terms of velocity) of the structure to external excitation is therefore measured with a laser transducer whose main characteristics are given in Table 2.3. The Polytec laser transducer is pictured in Figs. 2.6 and 2.7. Reflective stickers are glued at the measurement points to concentrate the laser beam (Fig. 2.7).

FIGURE 2.4 - LMS SCADAS Mobile acquisition system.

FIGURE 2.5 - LMS SCADAS Lab acquisition system.

Sensitivity	1000 mV/[m/s]
Transducer type	MSA-400 OFV-552
Manufacturer	Polytec
Serial number	0110716

TABLE 2.3 - Characteristics of the laser transducer.

FIGURE 2.6 - Polytec laser transducer.

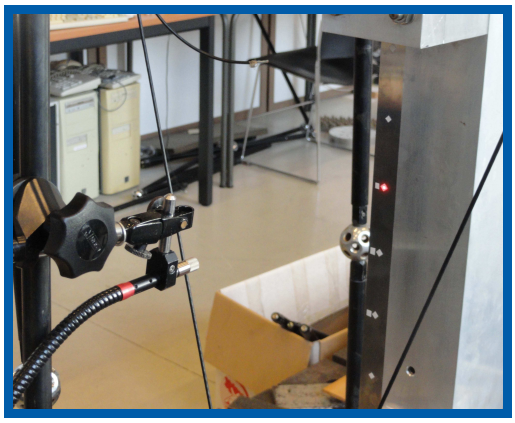

FIGURE 2.7 - Laser beam of the laser transducer.

In a first approach, an impact hammer is used to excite the structure (Fig. 2.8). This is indeed the simplest way for obtaining the impulse response functions (or equivalently the frequency response functions) required to identify the modal properties of the structure because it does not require to attach anything to the structure, which would not be appropriate considering the small weight of the steel strip. Impact testing with hammer also presents the advantage of requiring a limited and low cost equipment that allows a fast measurement. However, this technique shows a poor signal-to-noise ratio and the test engineer needs to get some experience and dexterity to avoid double impacts and ensure a good repeatability of the tests [3]. The hammer includes a force transducer. Its main characteristics are given in Table 2.4. In order to avoid exciting the nonlinearities, the amplitude of the force applied has to remain relatively small and the heavy head of the hammer is therefore removed. The impact hammer can be used with two tips of different stiffness: a steel tip and a vinyl one. For the current application, there is no need to excite the structure at very high frequencies since, in the following, only the first natural frequencies of the structure will be studied. The vinyl tip, which is softer, is therefore chosen. This choice will be justified more rigorously in the part of the work related to the experimental modal analysis of the structure (section 3.1.2).

Sensitivity	2.23 mV/N
Transducer type	086B03
Manufacturer	PCB
Serial number	5856

TABLE 2.4 - Characteristics of the instrumented impact hammer.

FIGURE 2.8 - Impact hammer and force transducer.

In a second step, the structure is excited with electrodynamic vibration exciters (or shakers) that can apply a wide range of force excitation signals. Two TV 50009 shakers have been selected to excite the structure (Fig. 2.9). With a rated peak force amplitude of 9 N, they correspond to the smallest model provided by the TIRA company [45]. Their main characteristics are given in Table 2.5.

Manufacturer	TIRA
Rated peak force	9 N
Frequency range	2 - 20000 Hz
Maximal displacement	3 mm

TABLE 2.5 - Characteristics of the shakers.

Sensitivity	23.41 mV/N - 99.0 mV/g
Transducer type	288D01
Manufacturer	PCB
Serial numbers	2592 - 2652

TABLE 2.6 - Characteristics of the impedance heads.

FIGURE 2.9 - Vibration Test System TV 50009 [45].

FIGURE 2.10 - Impedance head.

In order to apply the forced excitation F_w (Fig. 2.2), the first shaker is mounted horizontally close to the bottom fixation. As explained previously, this allows to avoid any impedance mismatch. In order to apply the parametric excitation F_u, the second shaker is mounted vertically at the bottom of the structure. A particular attention should be paid to the mounting of the shakers. The vibration exciters are attached to the structure under test through a drive rod (the stinger) which has the characteristics of being stiff in the direction of the excitation and flexible in the other directions. The stinger acts as a mechanical fuse. It is here an aluminum rod. The horizontal shaker is suspended with two cables at a fixed truss (Fig. 2.11). It is important to ensure that this shaker and the associated stinger are perfectly horizontal so that the force transmitted to the structure has only a horizontal component. To ensure this alignment, the shaker is the last element mounted on the structure. It is also checked that this alignment is preserved when the shaker acts and that the vibrations of the shaker base remain limited. The vertical shaker is fixed on its trunnion, which is the bracket that supports the shaker and allows to define with accuracy the position, angle and alignment of the shaker (Fig. 2.12).

Impedance heads, which combine both a force transducer and an accelerometer in a single housing (Fig. 2.10), are also added in order to facilitate the measurement of both parameters at a single point (where the shaker acts). Their main characteristics are given in Table 2.6. These impedance heads are glued on the structure at the excitation locations and the stingers are directly connected to the impedance heads. Such a mounting ensures that the transducer provides a reliable measure of the applied force and of the acceleration of the corresponding point. Impedance heads are always preferred to separate accelerometer and force transducer to measure drive point frequency responses [3]. Besides being more compact, they are also more accurate since the measurements are done exactly at the same point. Again, alignment is very important. In case of bad alignment, the impedance head sees loads that are not normal to the surface and there is a distortion of the actual measured force applied to the structure.

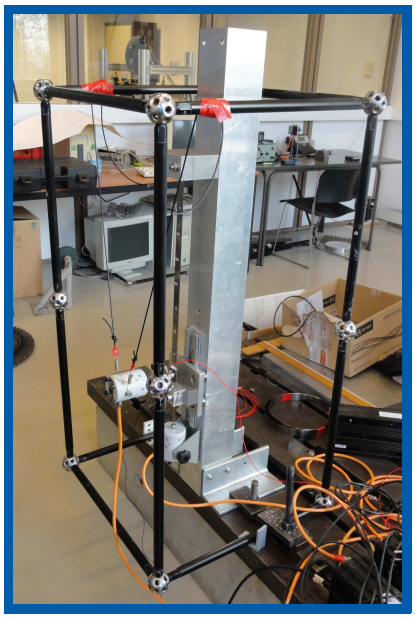

FIGURE 2.11 - Picture of the instrumented structure.

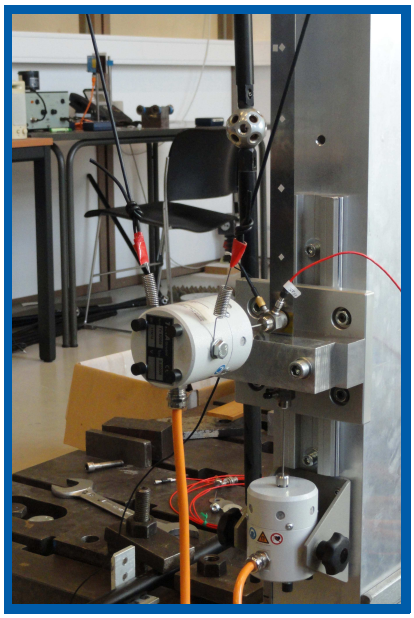

FIGURE 2.12 - Close-up on the mounting of the horizontal and vertical shakers.

PART 3

FINITE ELEMENT MODELING

This third part of the work aims at modeling the experimental set-up in an accurate way. The field of research referred to as “modal analysis” in the literature consists in understanding the dynamic behavior of a structure by identifying its modal parameters (namely the natural frequencies, the damping ratios and the mode shapes). It provides a powerful way to update a finite element model and get a reliable model of a mechanical structure.

Two different complementary approaches exist in modal analysis, respectively the theoretical and experimental modal analyses. On the one hand, the theoretical modal analysis is related to a direct problem. It requires a model of the structure. Model uncertainties are inherent to this kind of analysis. On the other hand, the experimental modal analysis is an inverse problem and requires a prototype. It allows to check if the finite element model represents the reality in an accurate way and to assess the impact of model uncertainties. It is important to highlight that modal analysis relies on two assumptions: linearity and time invariance of the structure. Even if these assumptions are never perfectly met in practice, they are not far from reality for most mechanical structures.

The flowchart shown in Fig. 3.1 summarizes the basics of the “model updating scheme” followed in this chapter. The methodology is inspired from the one described in [23]. Starting from a real structure, the two complementary modal analysis approaches are followed. The theoretical modal analysis of the structure consists in building a finite element model of the structure that allows to evaluate the modal properties of the strip. The results of this first study are then used to prepare the experimental measurements. The experimental modal analysis allows to get a second evaluation of the modal characteristics of the structure. Then, the results from both the theoretical and experimental modal analyses are compared with each other and the finite element model is updated in order to obtain a reliable model that reproduces the experimental results in an accurate way.

This chapter is divided into three main sections. In the first section, a model of the non-instrumented structure is built. In the second section, this model is adapted to take into account the interaction of the shakers with the structure. The methodology summarized in Fig. 3.1 is followed in these two sections. The last section shortly highlights the nonlinear behavior that the structure may experimentally exhibit when subjected to high amplitude excitations.

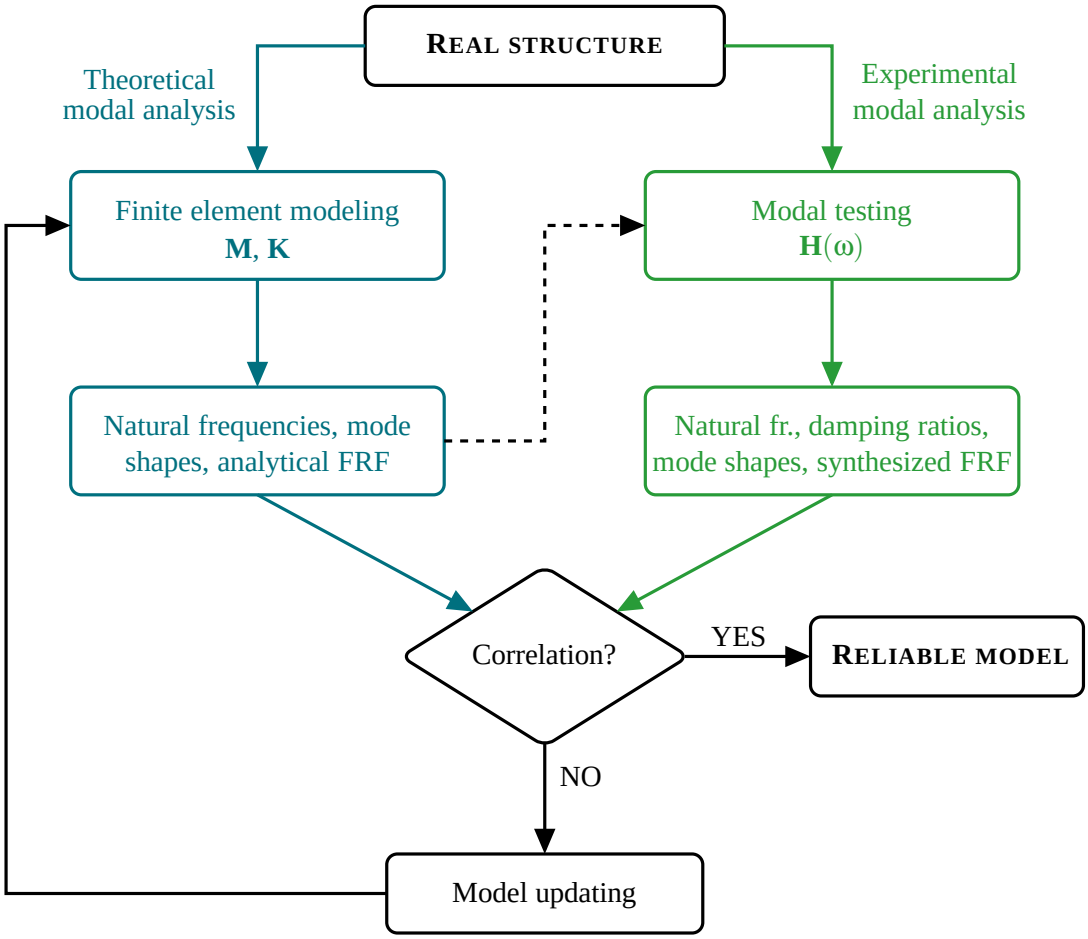

FIGURE 3.1 - Model updating scheme.

3.1 Modal analysis of the non-instrumented structure

The objective of this section is to obtain a reliable model describing the dynamics of the non-instrumented structure (without the shakers). Following the methodology summarized in Fig. 3.1, this section is divided in three parts. The first and second parts are respectively devoted to the theoretical and experimental modal analyses of the structure. In the third part, the results of the theoretical and the experimental modal analyses are compared and used to update the finite element model. Results of this section are also reported in [12].

3.1.1 Theoretical modal analysis

In this first section, finite element models of the structure are built in MATLAB and SAMCEF Field. These models are used to get a first estimate of the natural frequencies and mode shapes of the structure.

The structure is modeled in MATLAB using Bernoulli beam elements. The strip is divided into constant size elements. The mass and stiffness matrices $\mathbf{M}$ and $\mathbf{K}$ are obtained by assembling the corresponding elementary matrices. It should be noted that the stiffness matrix is composed of two parts: a geometrical stiffness matrix $\mathbf{K}_{\text{prestress,init}}$ is added to the usual linear stiffness matrix $\mathbf{K}_0$ to take into account the increased stiffness induced by the pre-stress mass. The elementary matrices used in the implementation of the finite element model can be found in [16]. The strip is assumed to be perfectly clamped at its top end. At the bottom, a lateral guide allows the strip to move only in the vertical x direction (Fig. 2.2).

A similar model is built in SAMCEF Field without the assumptions behind Bernoulli elements.

These two finite element models are used to compute the first seven natural frequencies of the strip. These frequencies are listed in Table 3.1. Both models use 50 elements of 1 cm length. It is checked further that this discretization is sufficient to capture the dynamics of the problem. The results obtained with the two models are in good agreement, which gives confidence in the MATLAB model and in the way in which pre-stress is taken into account. The results also confirm that Bernoulli elements are appropriate for representing the dynamics of the strip. The relative errors between the frequencies computed with the two models can be partially ascribed to the different treatments of shear deflection in the two approaches. The maximal relative error is indeed obtained with the fifth mode which is, as shown below, the first torsion mode of the structure.

	Frequency [Hz] MATLAB	*Frequency [Hz]* SAMCEF Field	*Relative error [%]*
Mode 1	18.36	18.34	0.08
Mode 2	39.71	39.75	0.10
Mode 3	65.93	65.94	0.03
Mode 4	98.16	98.17	0.02
Mode 5	101.94	102.61	0.65
Mode 6	137.01	137.02	0.01
Mode 7	182.81	182.82	0.01

TABLE 3.1 - Eigenfrequencies obtained with the initial finite element model (50 elements).

The corresponding mode shapes (obtained with the MATLAB model) are represented in Fig. 3.2. The modes obtained with the SAMCEF Field model (not shown) are similar. The higher the natural frequency, the more complex the form of the mode shape. The fifth mode is a torsion mode around the x-axis while the six other modes are the successive bending modes around the y-axis. Those are the usual low-frequency modes for a beam. From now, the bending mode shapes are normalized with a unit infinity norm (*i.e.* with a unit maximal displacement). This choice will allow an easy physical interpretation of the results.

In the absence of accurate information about damping, the damping ratios corresponding to the identified modes are not estimated with the finite element model. Only the experimental measurements described in the next section can provide reliable information on this issue.

Before further analyzing the structure, it is checked that the finite element discretization is sufficient to capture the dynamics of the strip up to its seventh mode. Fig. 3.3 shows the eigenfrequencies computed with the MATLAB model using different numbers of elements. The results are normalized by the eigenfrequencies computed with 50 elements, as listed in Table 3.1. Although the torsion frequency (mode 5) converges slightly more slowly, it can be checked that the different eigenfrequencies do not significantly change when the number of elements is increased beyond 50, *i.e.* for elements of length smaller than 1 cm. This finite element resolution is therefore considered as appropriate.

Some easy checks can be performed to give confidence in the theoretical modal analysis of the strip. They are based on the comparison of some numerical results with the corresponding analytical results available in the literature.

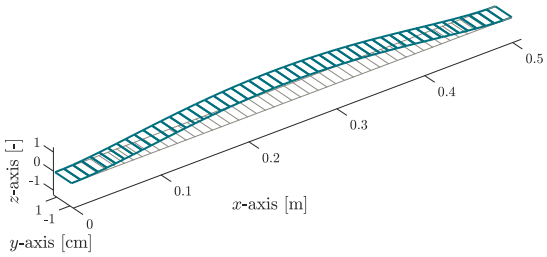

(a) Mode 1.

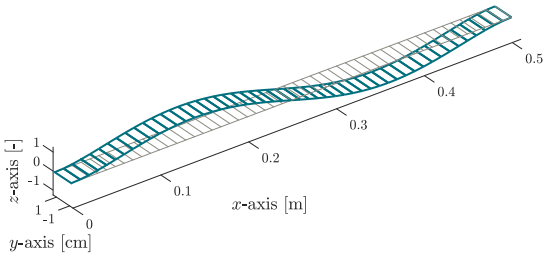

(b) Mode 2.

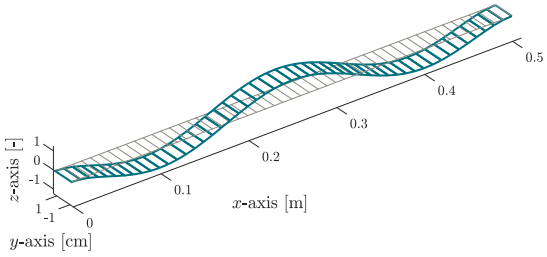

(c) Mode 3.

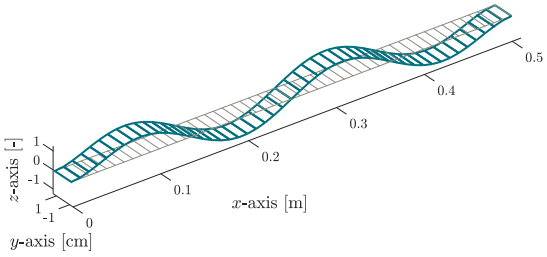

(d) Mode 4.

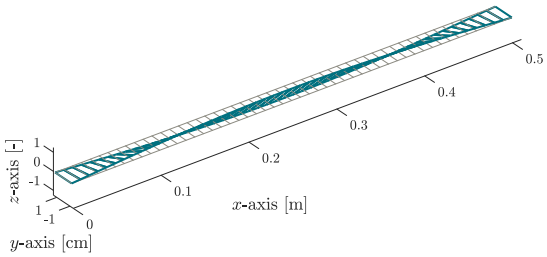

(e) Mode 5.

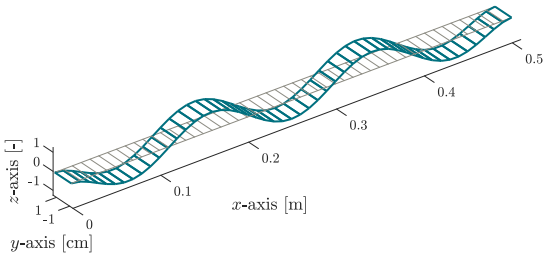

(f) Mode 6.

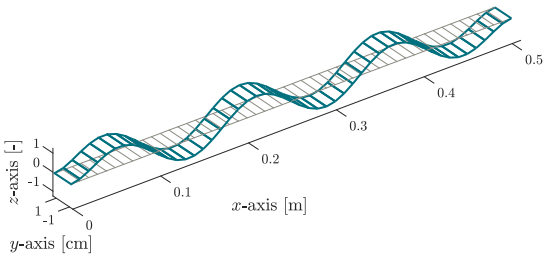

(g) Mode 7.

FIGURE 3.2 - The seven first modes of vibration obtained in MATLAB with the initial finite element model.

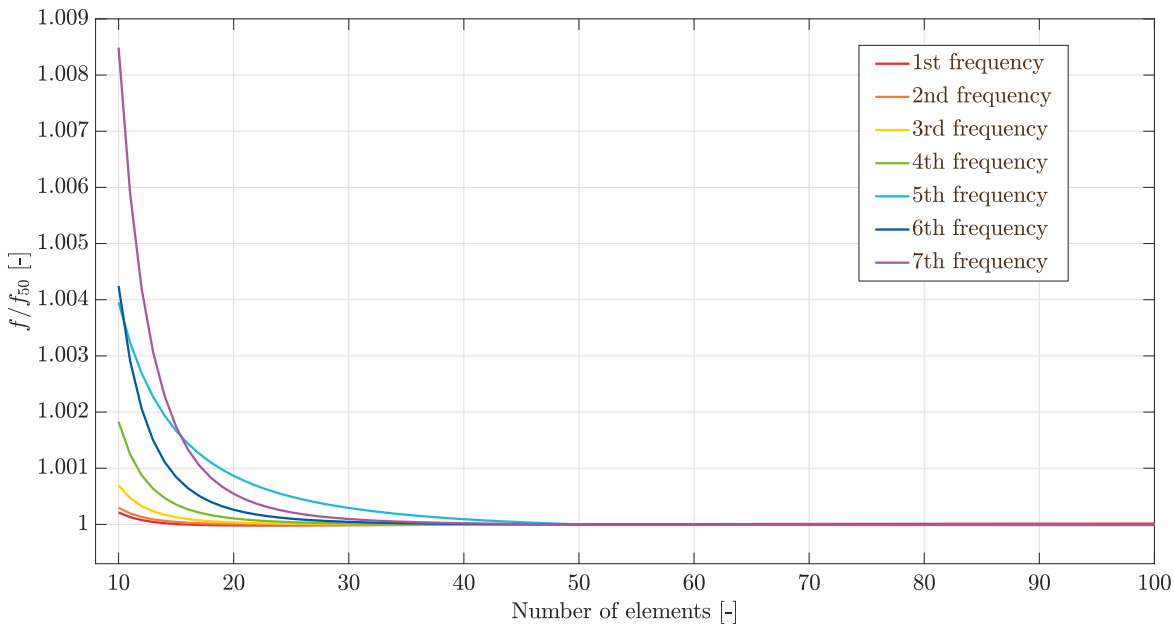

FIGURE 3.3 - Check of the convergence of the initial finite element model. Natural frequencies normalized by the frequencies computed with 50 elements as a function of the number of elements.

First, it is checked that, when the forces associated with the tension in the beam become much greater than the beam stiffness, the natural frequencies approach those of a straight tensioned cable. The natural frequencies f_i of a straight cable (with zero mean deflection) are given by

$$f_i = \frac{i}{2L}\left(\frac{T_0}{m}\right)^{1/2}, \qquad i \in \mathbb{N}_0, \tag{3.1}$$

where L is the cable length, m its mass per unit length and T_0 the tension in the cable [11]. Table 3.2 compares the natural frequencies obtained with the MATLAB finite element analysis when the stiffness of the structure is ignored with the analytical frequencies predicted by formula (3.1) for a tensioned cable. The very small differences between the two sets of results give confidence in the MATLAB finite element model.

	Frequency [Hz] MATLAB	*Frequency [Hz] Analytical*
Cable mode 1	15.12	15.11
Cable mode 2	30.24	30.23
Cable mode 3	45.37	45.34
Cable mode 4	60.48	60.46
Cable mode 5	75.61	75.58

TABLE 3.2 - Eigenfrequencies obtained with the MATLAB finite element model when the stiffness is ignored and analytical eigenfrequencies of a straight tensioned cable.

Then, the numerical eigenfrequencies of the structure in the absence of pre-stress can be compared with theoretical analytical results available in the literature. The book *Formulas for Natural Frequency and Mode Shape* by Blevins provides a review of analytical formulas and principles on the vibration of structures and fluid systems [6]. The natural frequencies in bending f_i of a single span straight beam are given by

$$f_i = \frac{\lambda_i^2}{2\pi L^2}\left(\frac{EI}{m}\right)^{1/2}, \tag{3.2}$$

where L is the beam length, E is its Young's modulus, I is the area moment of inertia of the beam about its neutral axis and m is the mass per unit length of the beam. The coefficients λ_i appearing in this formula depend on the boundary conditions. They are listed in Table 3.3 for a clamped-clamped beam. A nearly perfect agreement is observed between the eigenfrequencies provided by (3.2) and the bending natural frequencies obtained with the finite element model for a zero mass pre-stress (Table 3.4). Note however that torsion modes are not considered in (3.2).

i	1	2	3	4	5	>6
λ_i	4.73004074	7.85320462	10.9956078	14.1371655	17.2787597	$(2i+1)\pi/2$

TABLE 3.3 - Coefficients λ_i of (3.2) for the eigenfrequencies of a single span straight beam for clamped-clamped boundary conditions [6].

	Frequency [Hz] MATLAB	*Frequency [Hz] Analytical*
Bending mode 1	8.4364	8.4365
Bending mode 2	23.2554	23.2554
Bending mode 3	45.5900	45.5899
Bending mode 4	75.3626	75.3625
Bending mode 5	112.5786	112.5785

TABLE 3.4 - Eigenfrequencies obtained with the MATLAB finite element model with zero pre-stress of the structure and analytical eigenfrequencies of a single span straight beam.

Eventually, the natural frequencies of the pre-stressed strip can be compared with the analytical solutions provided by [6]. Tensile loads applied to beams increase their natural frequencies. Conversely, compressive loads decrease the natural frequencies. The natural frequencies f_i of a beam supporting a uniform axial load P differ from the natural frequencies in the absence of axial load $f_i|_{P=0}$ according to

$$f_i = f_i|_{P=0}\left(1+\frac{P}{|P_b|}\frac{\lambda_1^2}{\lambda_i^2}\right)^{1/2}, \tag{3.3}$$

where the coefficients λ_i are found in Table 3.3 for clamped-clamped boundary conditions and P_b is the critical buckling load of the structure which is given by

$$P_b = \frac{n^2\pi^2 EI}{L^2}, \tag{3.4}$$

where the coefficient n^2 depends on the boundary conditions and equals 4 for clamped-clamped boundary conditions.

The eigenfrequencies obtained numerically are compared with the analytical frequencies in Table 3.5. The two results differ by about 4 to 9%. These differences can be partially ascribed to the fact that the strip is not clamped at its two ends; its lower end can move in the vertical direction.

	Frequency [Hz] MATLAB	*Frequency [Hz] Analytical*	*Relative error [%]*
Bending mode 1	18.36	19.10	3.9
Bending mode 2	39.71	36.74	8.1
Bending mode 3	65.93	60.54	8.9
Bending mode 4	98.16	91.11	7.7
Bending mode 5	137.01	128.80	6.4
Bending mode 6	182.81	173.76	5.2

TABLE 3.5 - Eigenfrequencies obtained with the MATLAB finite element model and analytical eigenfrequencies of a pre-stressed single span beam clamped at its extremities.

3.1.2 Experimental modal analysis

This section describes the methodology and the main results of the experimental modal analysis of the physical prototype of the structure. First, the measurement process and the signal processing parameters are described and justified. Then, a preliminary data acquisition is performed in order to get a first estimate of the modal parameters of the strip. Eventually, a more detailed data acquisition is carried out and the modal parameters of the structure are identified.

Measurement process

The simplest way to perform the experimental modal analysis of the structure is to excite it with an impact hammer and to analyze the response of the structure to impacts. This is indeed a simple way of obtaining the impulse response functions required to identify the modal parameters of the structure because it does not require to attach anything to the structure. More information about the impact hammer and its use are given in section 2.3 dedicated to the description of the measurement chain.

The data acquisition and signal processing are carried out using the LMS Test.Lab software and the LMS SCADAS Mobile acquisition system. The tool Impact Testing of the Test.Lab Structures Acquisition module is chosen to perform the modal analysis with an impact hammer [43]. This module is particularly well suited for the current application and shows a wide range of capabilities, from the definition of the acquisition parameters to the detection of unusual circumstances, such as double hammer hits, to avoid incorrect measurements.

The finite element analysis performed in the previous section can be used to prepare the measurement process. In order to correctly represent the dynamics of the first six bending modes identified in Fig. 3.2, 9 equally spaced points on the central fiber of the strip are considered (Fig. 3.4). These points are denoted by P1 to P9 in this report. Because of its lightness, the structure is very responsive to hammer impacts. In order to avoid any overloading of the channels, the structure is only excited at the point closest to the bottom fixation (point P9 in Fig. 3.4). The laser transducer is used to measure the response at the different points P1 to P8. A roving accelerometer technique is used to measure a row of the frequency response functions matrix. As shown below, some measurements of the response at points located outside the neutral fiber are also performed to identify the torsion mode.

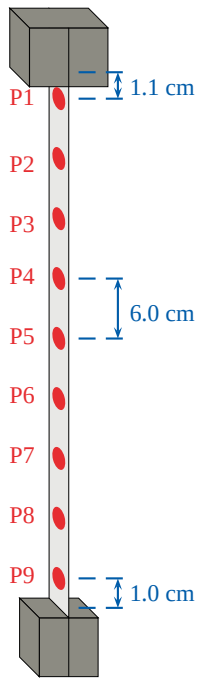

FIGURE 3.4 - Excitation and measurement points.

Selection of the appropriate bandwidth for the test and selection of the hammer tip are two very important factors that have to be considered at the beginning of the process [3]. All the modes of interest identified with the theoretical modal analysis have frequencies below 200 Hz. As justified in detail further, a bandwidth of $f_{\max} = 400$ Hz is selected in order to avoid errors below 200 Hz due to the anti-aliasing filter. In order to reach an accuracy close to 0.1 Hz on the frequencies, $N = 4096$ spectral lines are considered. This gives an acquisition time of 10.24 s.

On the one hand, if the tip is too soft with respect to the selected bandwidth, the power spectral density drops before the end of the frequency band so that the highest frequencies are not excited. This leads to bad coherence and wrong frequency response functions in that region. On the other hand, when a too hard tip is selected, the power spectral density is very flat on the whole frequency band, but the actual excited frequency range may be well beyond the selected bandwidth for the measurement. Actually, some of the data acquisition range will be used for the energy of the modes excited outside the desired bandwidth and will have a detrimental effect on the measurement. Only a small fraction of the total energy measured is associated with the bandwidth of interest. This results in a quantization problem in the analog-to-digital converter. The power spectral density of a typical impact with the vinyl tip is represented in Fig. 3.5(a) on the frequency band [0 ; 400 Hz] and in Fig. 3.5(b) on the frequency band [0 ; 1600 Hz] (4 times the bandwidth). These figures confirm that the chosen tip is appropriate. The power spectral density appears to be sufficiently smooth on [0 ; 400 Hz] and the roll off is sufficient beyond 400 Hz so that higher frequencies are not excited.

When processing the signal, two types of errors may appear: variance and bias errors [15]. Variance errors are due to the discrepancy between the mean of each sample and the mean of the ensemble. Such errors can be reduced by averaging a sufficiently large number of samples. To achieve a good compromise between the acquisition time and the accuracy of the measurements, the average between three successive tests is made. Bias errors can be separated into aliasing and leakage errors.

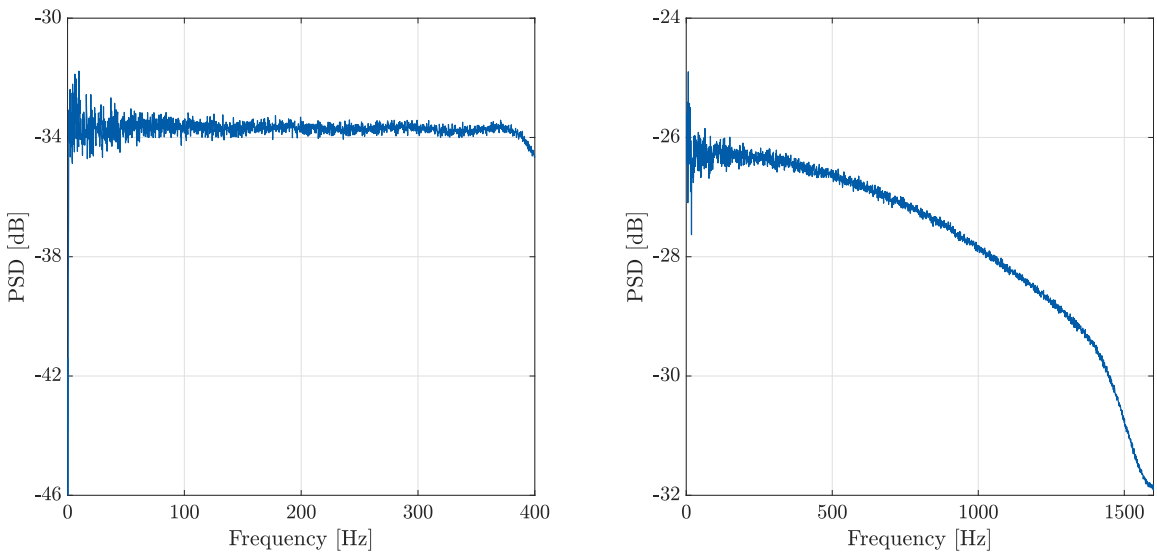

(a) On the bandwidth.

(b) On 4 times the bandwidth.

FIGURE 3.5 - Power spectral density of a typical impact force performed with the vinyl tip.

The LMS Test.Lab software sets the sampling frequency f_s at a sufficiently high value to avoid aliasing [43]. The LMS SCADAS Mobile acquisition system has a built-in anti-aliasing filter. This filter is however not ideal and the last 20% of the frequency band have to be treated with care. This justifies a posteriori the choice of the frequency band that is sufficiently wider than the band of interest.

In order to reduce leakage errors, windowing techniques are applied to the excitation and the response signals. These windows force the signal to vanish at the end of the observation time and, therefore, filter out otherwise unavoidable noise components at the end of the signal. The forms of the windows are adapted to the forms of the signal in order to limit its distortion: a rectangular window is chosen for the impact and an exponential one for the response (The response to impacts has the form of the damped exponential response of all the modes excited by the input.). The observation time must be long enough to ensure that the response decreases sufficiently and that the window does not distort too much the time measured data. The optimum parameters defining the windows are set by the LMS Test.Lab software by analyzing and averaging several successive impacts [43].

Potential quantization problems must also be addressed [3]. Quantization refers to the accuracy with which the amplitude of an analog signal is digitized. If sufficient resolution is not available, the signal will be distorted. The voltage ranges for each channel must be set to appropriate values so that the analog-to-digital converter is optimized. The acquisition system is used to autorange the response levels. The overload reject switch is turned on so that overloaded measurements are not accepted.

In order to correctly capture the impacts, two quantities have to be defined: the trigger level and the pretrigger. Those are automatically defined by the LMS Test.Lab software by analyzing and averaging several impacts [43]. The acquisition is triggered when the signal on the hammer channel exceeds the trigger level, which is 0.1 N here. The pretrigger determines the time prior to the trigger condition that will be included in the acquisition. It is given by 0.1 s in the considered experimental set-up and avoids losing part of the impact in the acquisition.

Preliminary data acquisition

Before embarking upon the complete modal analysis of the strip, the analysis of the response of the structure to a single impact is used to provide a first estimate of the natural frequencies and damping ratios. As explained previously, the structure is triggered at point P9 (Fig. 3.4). The measurement point must be carefully chosen in order to detect all the modes identified with the finite element method. It is therefore important that this point does not coincide with a vibration node of any bending mode. The point P2 meets this condition and is therefore selected.

The measured frequency response function and its coherence function are represented in Fig. 3.6. The coherence function is a good indicator of the accuracy and the repeatability of the performed impacts [23]. The values close to 1 taken by the coherence function in the whole range of interest indicate that the noise in the measured signals is limited and that the three successive impacts are performed with enough accuracy at the same location. As expected, the coherence function drops at low frequency and at the anti-resonance frequencies. This is not a problem since the output is very small at these locations.

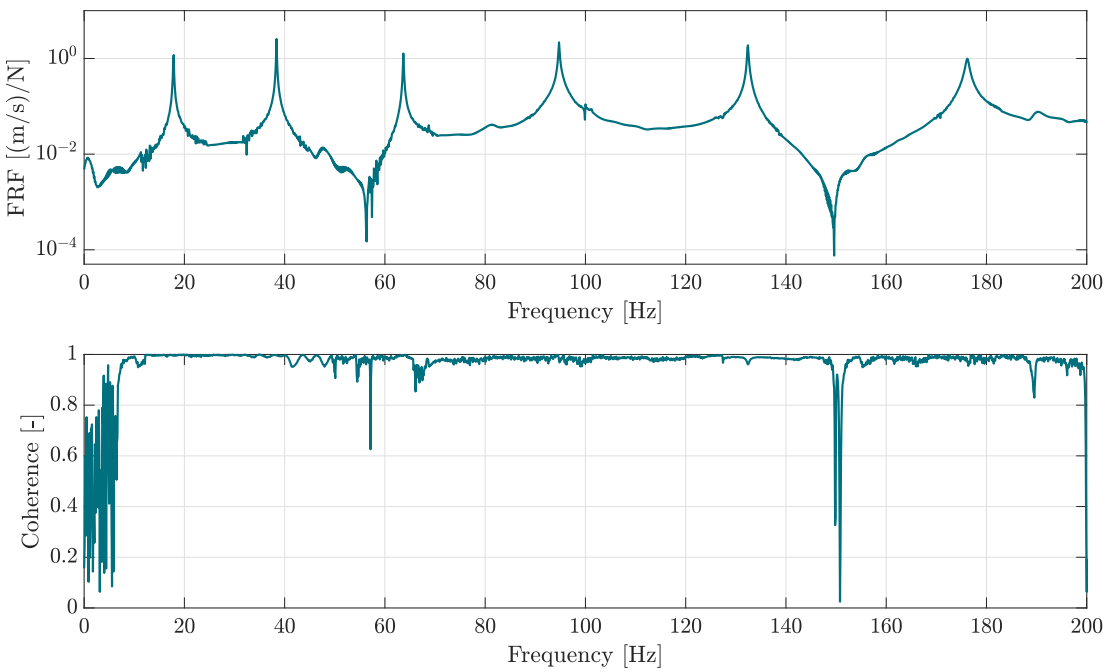

FIGURE 3.6 - Frequency response function and coherence function corresponding to an excitation at point P9 and the measurement of the response at point P2.

The measured frequency response function plotted in Fig. 3.6 provides a quick way of determining the number of modes in a given frequency band [15]. It allows to highlight the resonance peaks of the structure and, therefore, to identify the resonance frequencies. Six modes can be clearly seen between 0 and 200 Hz. They correspond to the six bending modes identified with the finite element model. The natural frequencies obtained by this analysis of the experimental data are given in Table 3.6.

	Frequency [Hz]
Bending mode 1	17.9
Bending mode 2	38.3
Bending mode 3	63.7
Bending mode 4	94.7
Bending mode 5	132.4
Bending mode 6	175.5

TABLE 3.6 - Eigenfrequencies identified with the frequency response function plotted in Fig. 3.6.

This preliminary data acquisition can also provide estimates of the damping ratios associated to the different modes. Two single-degree-of-freedom methods are implemented in MATLAB: the peak-picking method and the circle-fit method. These two methods work in the frequency domain. Single-degree-of-freedom modal analysis methods may be applied when the modes are well separated in frequencies and can therefore be analyzed separately by focusing on a given frequency band. The accuracy of the peak-picking method and the circle-fitting method depends on the number of points that describe the resonance peak. These methods are used here to estimate the damping ratio of the fifth bending mode. Similar results can be obtained for the other modes of the structure.

The peak-picking method is illustrated in Fig. 3.7 [23]. In this figure, the peak corresponding to the fifth bending mode is isolated. The Bode plot of the frequency response function amplitude is used to detect the maximum response and the half-power points. The modal damping is evaluated by

$$\varepsilon \simeq \frac{\Delta f}{2f}, \tag{3.5}$$

where Δf is the frequency bandwidth between the half-power points and f is the natural frequency of the mode (Fig. 3.7). A damping ratio of 0.09% is found.

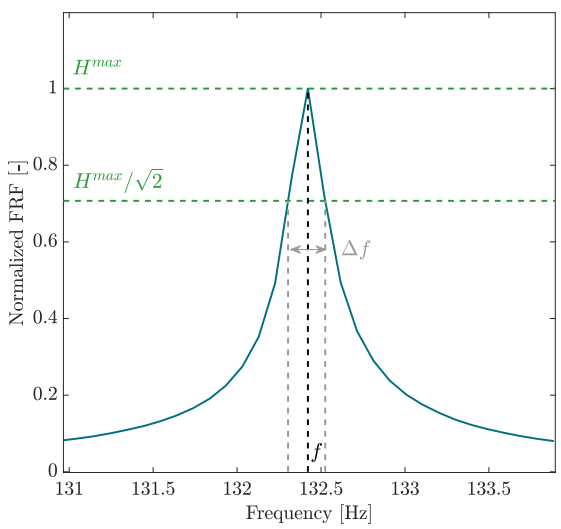

FIGURE 3.7 - Peak-picking method (fifth bending mode).

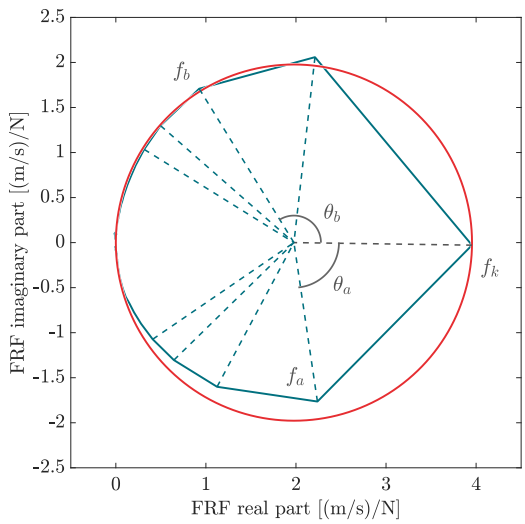

FIGURE 3.8 - Circle-fit method (fifth bending mode).

The circle-fit method is illustrated in Fig. 3.8. It is based on the circular nature of the Nyquist plot of the frequency response function when viscous damping is assumed and when the frequency response function is expressed in its mobility form [23]. The modal damping associated to mode k can be expressed by

$$\varepsilon_k = \frac{f_a^2 - f_b^2}{2 f_k [f_a \tan(\theta_a/2) + f_b \tan(\theta_b/2)]}, \tag{3.6}$$

where f_k is the natural frequency of the mode, f_a/f_b are frequencies close to f_k around the circle and θ_a/θ_b are the corresponding angles measured with respect to the radius of the circle associated to the resonance frequency. An example of these parameters is shown in Fig. 3.8. The mean value of the different ε_k computed with different values for f_a and f_b is equal to 0.096% and is therefore in good agreement with the result of the peak-picking method.

In order to check the linearity of the behavior of the structure, a second test is performed by switching the excitation and the measurement points. The structure is therefore excited at point P2 and the response is measured at point P9. Notice that the point P2 is also sufficiently close to the top fixation of the strip to avoid overloading of the channels (Fig. 3.4). The norms of the two frequency response functions are plotted in Fig. 3.9. The curves are in good agreement except at low frequencies where the data are noisy, as already shown by the coherence function in Fig. 3.6. Fig. 3.9 shows that the reciprocity principle is verified and that the assumption of linearity is therefore justified.

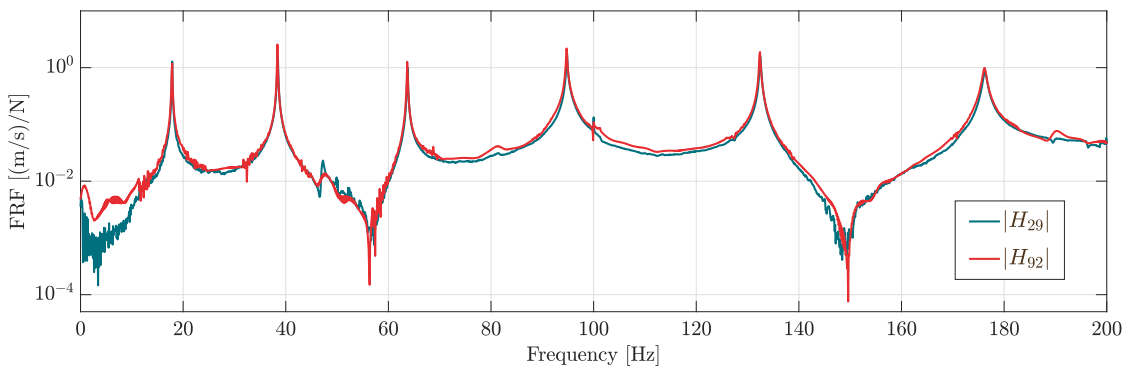

FIGURE 3.9 - Frequency response functions corresponding to an excitation at point P9 (resp. P2) and the measure of the response at point P2 (resp. P9). Illustration of the reciprocity principle.

Before moving to the more detailed data acquisition, it should be noted that the structure has also been excited at other points and that the response has been measured at other points to check that no mode is missed in this preliminary study. Also, this preliminary data acquisition has been repeated several times on several days characterized by different ambient conditions. The frequency response functions appear to be invariant with respect to these conditions. The system can therefore hopefully be considered as time-invariant.

Identification process

A more detailed data acquisition is performed on the strip. The structure is excited at point P9 (Fig. 3.4) and the response is successively measured at each of the other points. The values given to the various parameters used for the acquisition have already been given and justified previously. Using the measurement data, it is then possible to extract the modal parameters of the structure. The natural frequencies f_r and damping ratios ε_r are obtained using the *Least Square Complex Exponential* (LSCE) method. The mode shapes $\mathbf{z}_r$ are computed with the *Least Square Frequency Domain* (LSFD) method.

The LSCE method, introduced in 1979 by Brown et al. [7], works in the time domain and requires experimental measurements in the form of impulse response functions (IRF). The impulse response functions are not directly given by the LMS Test.Lab software but are easily obtained by taking the inverse Fourier transforms of the transfer functions.

An important issue of many identification techniques is the selection of the model order. The stabilization diagram allows to differentiate between real and spurious modes. In Fig. 3.10, a mode is considered as "stabilized in frequency" (green marker) if its frequency differs by less than 0.1 Hz from a mode identified with the previous order. A mode is considered as "stabilized in frequency and damping" (blue marker) if it is stabilized in frequency and if its damping ratio differs by less than 0.01% from the mode identified at this frequency at the previous order. If the mode is not stabilized in frequency, it is classified as "unstabilized" and represented by a red marker. The six modes corresponding to the peaks of the mean frequency response function (represented in gray in the figure) are clearly identified.

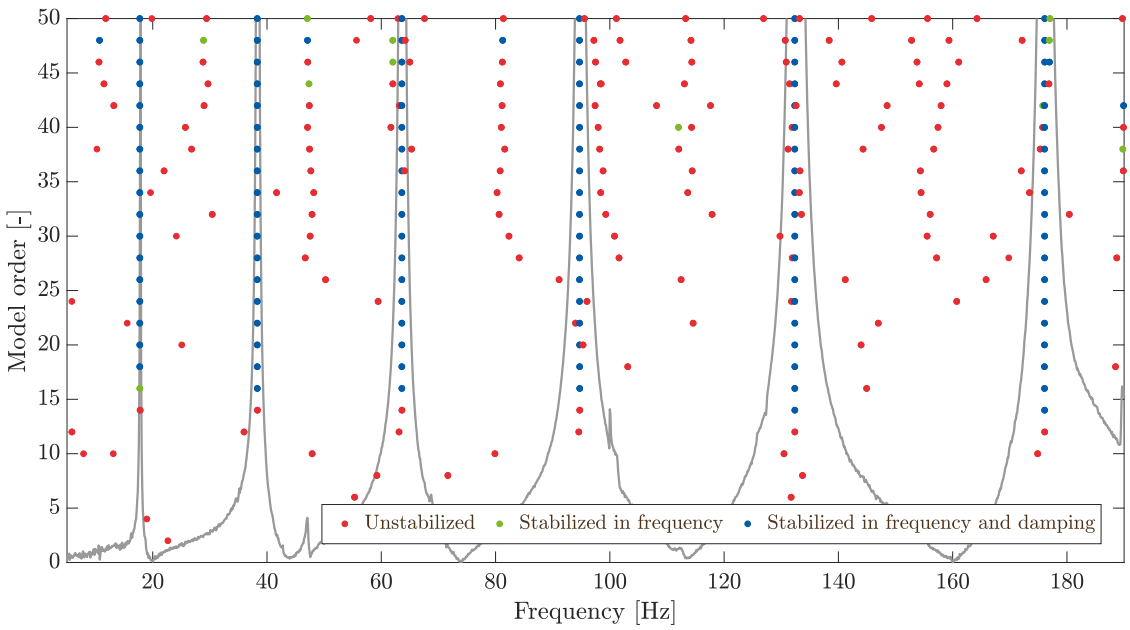

FIGURE 3.10 - Stabilization diagram of the LSCE method applied to the non-instrumented structure. The gray curve represents a reference frequency response function.

The eigenfrequencies and damping ratios obtained by identification with the LSCE method are given in Table 3.7. It should be noted that identification methods are also directly implemented in the LMS Test.Lab software. In particular, the *Polyreference Least-Squares Complex Frequency-Domain* (PolyMAX) method is a general purpose method for strongly and weakly damped structures that provides very clear stabilization diagrams [27]. It was introduced as an alternative to LSCE and allows to work directly on the frequency response functions to identify the natural frequencies and damping ratios. The natural frequencies and damping ratios obtained with the PolyMAX method are also listed in Table 3.7. A good agreement is observed between the two sets of results and gives confidence in the MATLAB implementation of the LSCE method. This table shows that the damping in the structure is really light. The fourth and sixth bending modes have a modal damping larger than the other modes. These results can be compared with the results of the preliminary data acquisition. The natural frequencies identified with the single frequency response function measured (Fig. 3.6) are close to the frequencies of the table. Moreover, it can also be checked that the value $\varepsilon = 0.09 - 0.10\%$ obtained for the fifth bending mode with the peak-picking method and the circle-fit method is a good estimate of the damping ratio.

	Frequency [Hz] LSCE	*Frequency [Hz]* PolyMAX	*Damping ratio [%]* LSCE	*Damping ratio [%]* PolyMAX
Bending mode 1	17.8	17.8	0.06	0.06
Bending mode 2	38.5	38.4	0.03	0.05
Bending mode 3	63.8	63.7	0.08	0.06
Bending mode 4	94.7	94.8	0.20	0.20
Bending mode 5	132.5	132.5	0.08	0.10
Bending mode 6	175.9	176.2	0.21	0.25

TABLE 3.7 - Comparison of the eigenfrequencies and damping ratios obtained with the LSCE method implemented in MATLAB and the PolyMAX method implemented in the LMS Test.Lab software.

The companion method LSFD is implemented to identify the mode shapes of the structure. Unlike the LSCE method, the LSFD method works in the frequency domain [23]. This method takes advantage of the previous knowledge of the natural frequencies and damping ratios identified with the LSCE method (Table 3.7). The modes extracted with this method are complex. However, because the identified damping ratios are small, one can expect that the different degrees of freedom of the structure vibrate in phase. The complexity of the mode shapes is assessed with the Argand diagram. Fig. 3.11 represents the Argand diagrams of the six bending modes identified with the LSFD method. It is checked that all the nodes of the structure vibrate in phase in the different mode shapes. The real bending modes extracted from the complex ones are shown in Fig. 3.12.

Different tools are commonly used in industry in order to check that the modes are physical and, therefore, that the order is correctly selected [43]. The first check is provided by a visual inspection of the modes. At low frequencies, the simplest modes must be observed. This is the case here: the first modes identified correspond to the usual first bending modes of a beam. Then, the different mode shapes must be independent. This is checked with the auto-MAC matrix represented in Fig. 3.13. Because all the out-of-diagonal terms are close to 0, the modes are indeed independent.

To end this experimental part, an estimate of the first torsion natural frequency is obtained by measuring the response at several points that are not located on the neutral fiber of the strip. A value of $f = 101.4$ Hz is found.

3.1.3 Model updating

At this stage of the study, two sets of modal parameters are available. On the one hand, estimates of the natural frequencies and mode shapes of the strip have been obtained in section 3.1.1 based on finite element models. On the other hand, a second set of modal parameters (natural frequencies, damping ratios and mode shapes) comes from the experimental modal analysis performed in section 3.1.2. In the first part of this section, the two sets of modal parameters are compared. Then, the finite element is updated in order to reduce the discrepancies between the results of the theoretical and experimental modal analyses, in agreement with the methodology set in Fig. 3.1.

The results obtained with the MATLAB finite element model and with the experimental modal analysis are summarized in Table 3.8. The natural frequencies obtained with the initial finite element models systematically overestimate the corresponding natural frequencies identified with the experimental analysis by 3-4% for the bending modes, which leaves room for improvement.

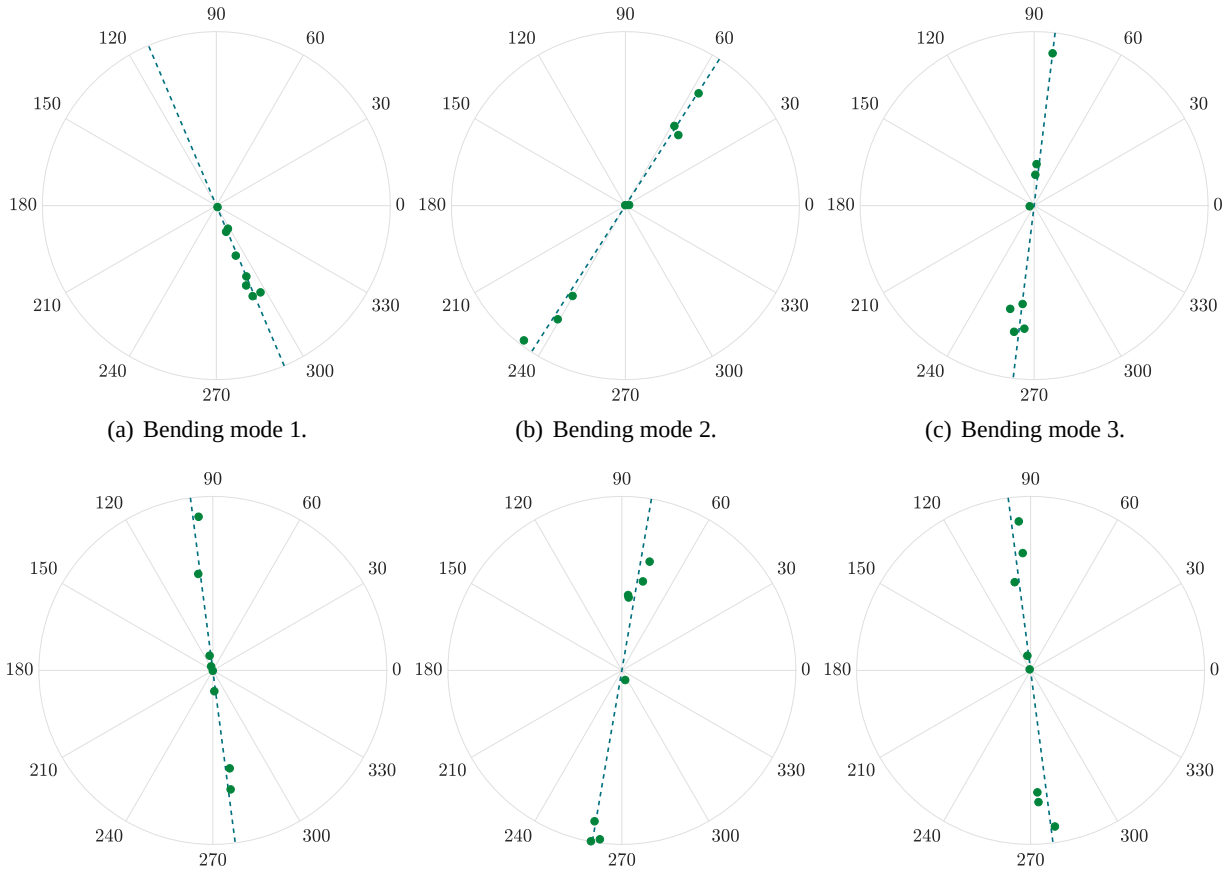

(a) Bending mode 1. (b) Bending mode 2. (c) Bending mode 3.

(d) Bending mode 4. (e) Bending mode 5. (f) Bending mode 6.

FIGURE 3.11 - Argand diagrams of the six first bending modes identified experimentally on the non-instrumented structure.

	Frequency [Hz] TMA	*Frequency [Hz]* EMA	*Relative error [%]*
Bending mode 1	18.4	17.8	3.1
Bending mode 2	39.7	38.5	3.1
Bending mode 3	65.9	63.8	3.3
Bending mode 4	98.2	94.7	3.7
Torsion mode 1	101.9	101.4	0.4
Bending mode 5	137.0	132.5	3.4
Bending mode 6	182.8	175.9	3.9

TABLE 3.8 - Comparison of the eigenfrequencies obtained from theoretical (TMA, initial model) and experimental (EMA, non-instrumented structure) modal analyses.

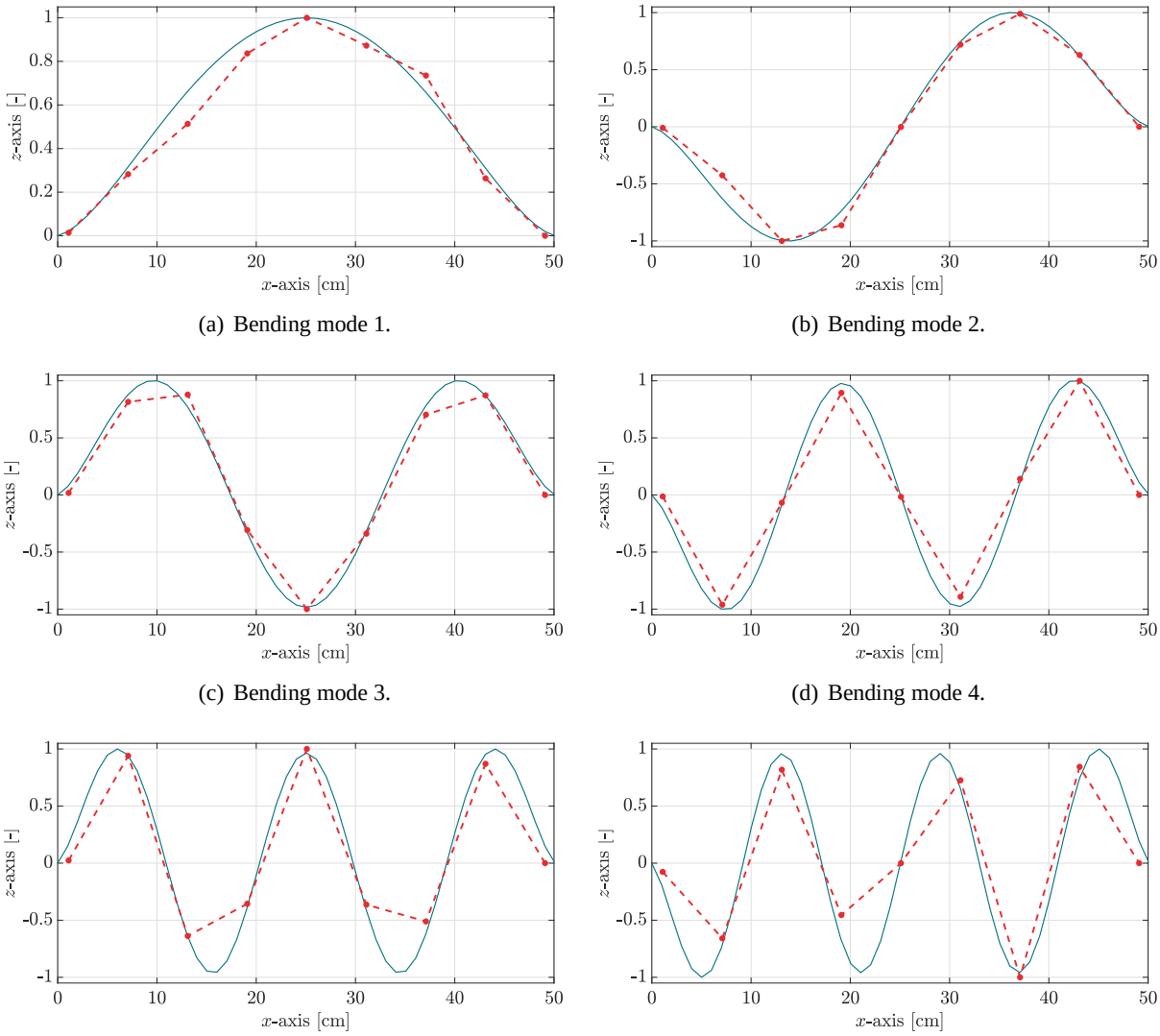

(a) Bending mode 1.

(b) Bending mode 2.

(c) Bending mode 3.

(d) Bending mode 4.

(e) Bending mode 5.

(f) Bending mode 6.

FIGURE 3.12 - The six first bending modes of the non-instrumented structure identified with the LSFD method (in red) compared to the modes obtained with the initial finite element model (in blue).

Visually, the two sets of mode shapes are in good agreement (Fig. 3.12). They correspond to the successive bending modes of the strip. The Modal Assurance Criterion (MAC) can be used to quantify the correlation between the two sets of modes [1]. The MAC computed between mode i of the first family $\psi^1_{(i)}$ and mode j of the second $\psi^2_{(j)}$ is given by

$$\mathrm{MAC}(\psi^1_{(i)}, \psi^2_{(j)}) = \left(\frac{{\psi^1_{(i)}}^T \psi^2_{(j)}}{||\psi^2_{(j)}|| \cdot ||\psi^2_{(j)}||} \right)^2 . \tag{3.7}$$

The MAC matrix based on the two sets of modes available is represented in Fig. 3.16. The close-to-one values of its diagonal elements and the negligible values of its out-of-diagonal elements confirm the very good correlation reported above.

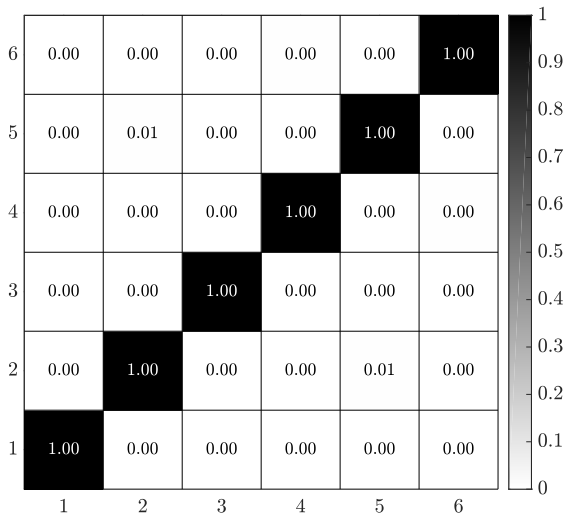

FIGURE 3.13 - Auto-MAC matrix of the experimental bending modes identified with the LSFD method (non-instrumented structure).

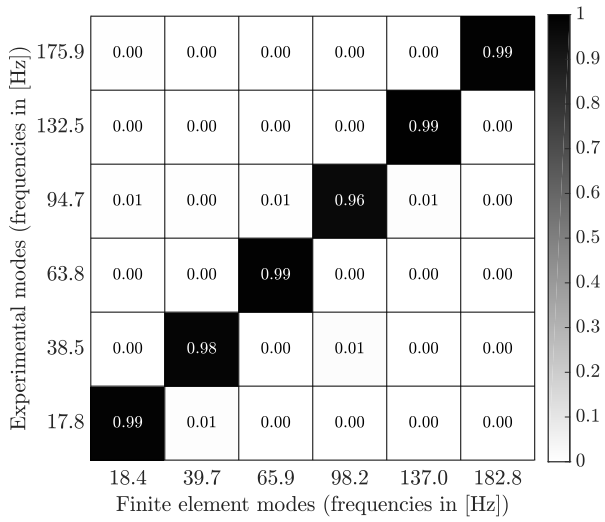

FIGURE 3.14 - MAC matrix between the numerical modes (initial model) and the experimental modes (non-instrumented structure).

Despite the high correlation between the mode shapes, a model updating can be carried out to reduce the relative errors between the natural frequencies.

The imperfect agreement can result from a bad experimental analysis or from modeling errors and uncertainties. It has been shown in the previous section that the measurement process is performed in a rigorous way and that the choice of the measurement coordinates is justified. Moreover, the modal identification gives the same results as the PolyMAX identification method implemented directly in the LMS Test.Lab software. It is therefore argued that it is the finite element modeling of the structure that must be improved.

While errors can be introduced by the discretization process, it was shown in section 3.1.1 that the number of finite elements used in the numerical models is sufficient to capture the dynamics of the problem. Refining the mesh does not lead to any significant change in the natural frequencies.

The errors can be related to the assumptions about the physics of the model. Here, the natural frequencies obtained with the model are slightly higher than the experimental ones. The model is therefore more rigid than the real structure. This can result from the choice of the boundary conditions in the initial model. Perfect clamping is a mathematical idealization that never exists in practice. It is impossible to completely prevent any rotation about the y-axis at the fixations of the strip (Fig. 2.2). The finite element model is therefore corrected by introducing a stiffness in rotation about the y-axis at both ends of the strip. To simplify the analysis, the stiffness coefficient is supposed to be the same on both sides. The rigidity of the clamping is determined in such a way that it minimizes the error (in a least-square sense) between the natural frequencies obtained with the numerical and experimental modal analyses. Fig. 3.15 shows the global error as a function of the stiffness in rotation k. An optimum value of $k = 3.83$ Nm/rad is found.

Table 3.9 shows the natural frequencies computed after updating of the finite element model, *i.e.* after modification of the boundary conditions. These frequencies can be compared with the experimental frequencies and show now relative errors less than 0.2%.

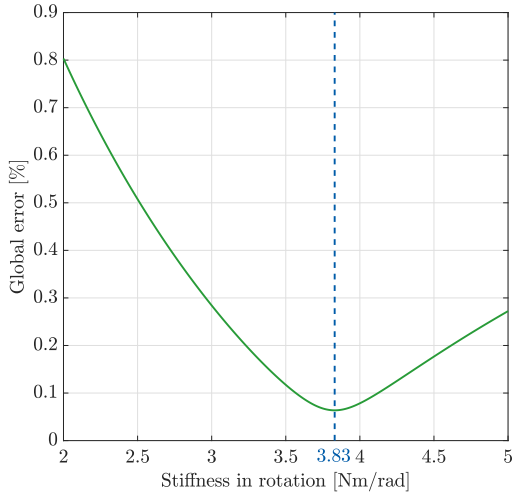

FIGURE 3.15 - Global error on the natural frequencies as a function of the stiffness in rotation and determination of the optimum value.

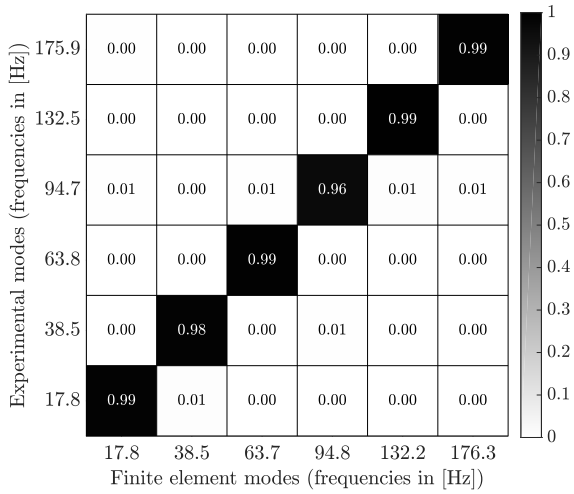

FIGURE 3.16 - MAC matrix between the numerical modes (updated model) and the experimental modes (non-instrumented structure).

	Frequency [Hz] TMA	*Frequency [Hz]* EMA	*Relative error [%]*
Bending mode 1	17.8	17.8	0.1
Bending mode 2	38.5	38.5	0.1
Bending mode 3	63.7	63.8	0.1
Bending mode 4	94.8	94.7	0.1
Torsion mode 1	101.9	101.4	0.4
Bending mode 5	132.2	132.5	0.2
Bending mode 6	176.3	175.9	0.2

TABLE 3.9 - Comparison of the eigenfrequencies obtained from theoretical (TMA, updated model) and experimental (EMA) modal analyses of the non-instrumented structure.

One can also check in Fig. 3.16 that the adjustment of the model does not have any detrimental effect on the correlation between the numerical and experimental mode shapes. The out-of-diagonal terms are really close to 0 while the diagonal terms vary between 0.96 and 0.99.

3.2 Modal analysis of the instrumented structure

While the model derived above provides an accurate description of the dynamics of the strip itself, the shakers mounted on it have a non-negligible influence on the dynamics and require therefore to modify the model. The objective of this section is to obtain a reliable model describing the dynamics of the structure when both the horizontal and vertical shakers are mounted on it. The first part is devoted to the experimental modal analysis of the structure. In the second part, in agreement with the methodology summarized in Fig. 3.1, the finite element model of the non-instrumented structure is updated to take into account the influence of the shakers on the dynamics of the structure. The last part describes how damping is added into the finite element model.

3.2.1 Experimental modal analysis

The experimental modal analysis is carried out by exciting the structure with the horizontal shaker. As explained previously, the horizontal shaker is located near the bottom fixation. The point of excitation is chosen in such a way that all the modes previously identified are excited. The vertical shaker is not exciting the structure but is mounted on it in such a way that its interaction with the structure is taken into account. The tool Spectral Testing of the module Test.Lab Structures Acquisition allows to control the excitation of the shaker. A white noise defined on the complete acquisition bandwidth is selected. The same acquisition parameters as before are chosen and a free run trigger is selected. As it is usually done for random signals, Hanning windows are used on both the excitation and the response to limit leakage problems [3].

The excitation levels for modal testing are usually very low. There is no need to provide large force levels for conducting a modal test, especially if appropriate response transducers with good sensitivity are selected. Large forces can excite nonlinear characteristics, which has to be avoided in the context of linear modal analysis.

Fig. 3.17 shows the frequency response function measured with the impedance head at point P9 where the horizontal shaker acts. As expected at drive points, the resonances are separated by anti-resonances.

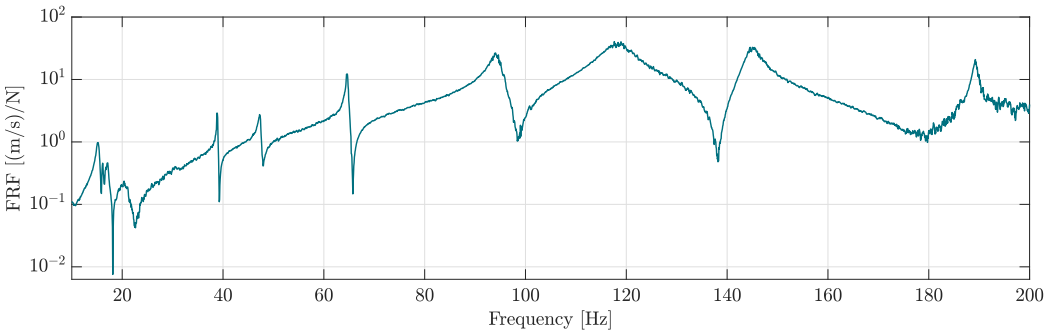

FIGURE 3.17 - Frequency response function measured at the drive point P9.

The identification of the natural frequencies, damping ratios and mode shapes is performed with the *Stochastic Subspace Identification* (SSI) method. This method directly works on the recorded time signals [34]. The stabilization diagram represented in Fig. 3.18 allows to distinguish real modes from spurious ones. A mode is considered as stabilized in frequency if its frequency differs by less than 0.1 Hz from a mode identified at the previous order. A mode is considered as stabilized in damping if its damping ratio differs by less than 0.01% from the damping ratio of the mode identified at this frequency at the previous order. A mode is considered as stabilized in mode shape if the modal assurance criterion (MAC) between the mode and a mode identified at the previous order is larger than 0.95.

The eigenfrequencies and damping ratios obtained by identification with the SSI method are given in Table 3.10. The results are compared with those obtained with the PolyMAX method implemented in LMS Test.Lab.

3.2.2 Model updating

Table 3.11 summarizes the natural frequencies obtained with the MATLAB finite element model and those identified experimentally. The relative errors greater than 10% observed for the last bending modes are clearly not acceptable. The interaction of the shaker with the structure has to be taken into account.

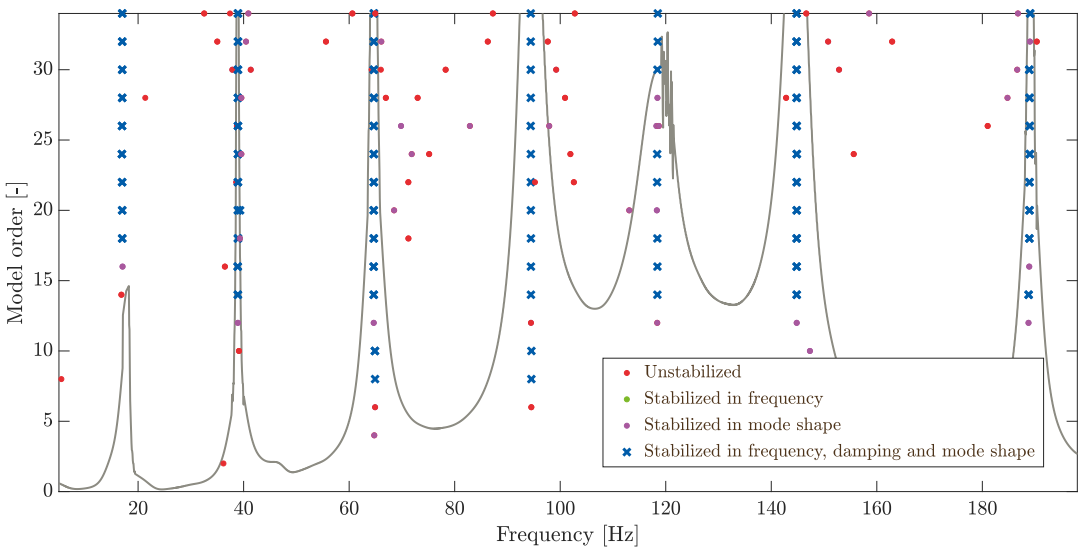

FIGURE 3.18 - Stabilization diagram of the SSI method applied to the instrumented structure. The gray curve represents a reference frequency response function.

	Frequency [Hz] SSI	*Frequency [Hz]* PolyMAX	*Damping ratio [%]* SSI	*Damping ratio [%]* PolyMAX
Bending mode 1	18.4	18.6	0.61	0.63
Bending mode 2	38.9	38.9	0.17	0.18
Bending mode 3	64.7	64.6	0.62	0.60
Bending mode 4	94.1	94.4	1.09	1.10
Bending mode 5	118.1	118.8	2.81	2.99
Bending mode 6	145.8	144.8	0.35	0.39

TABLE 3.10 - Comparison of the eigenfrequencies and damping ratios of the instrumented structure obtained with the SSI method implemented in MATLAB and the PolyMAX method implemented in the LMS Test.Lab software.

	Frequency [Hz] TMA	*Frequency [Hz]* EMA	*Relative error [%]*
Bending mode 1	17.8	18.4	4.3
Bending mode 2	38.5	38.9	1.0
Bending mode 3	63.7	64.7	1.5
Bending mode 4	94.8	94.1	0.4
Torsion mode 1	101.9	101.2	0.7
Bending mode 5	132.2	118.1	12.2
Bending mode 6	176.3	145.8	21.7

TABLE 3.11 - Comparison of the eigenfrequencies obtained from theoretical (TMA, non-instrumented structure) and experimental (EMA, instrumented structure) modal analyses.

The horizontal shaker, the stinger and the impedance head glued to the strip (Fig. 3.19) are modeled by a spring-mass system. This equivalent system is represented in Fig. 3.20. The values of the masses and stiffness coefficients used in the model are given in Table 3.12.

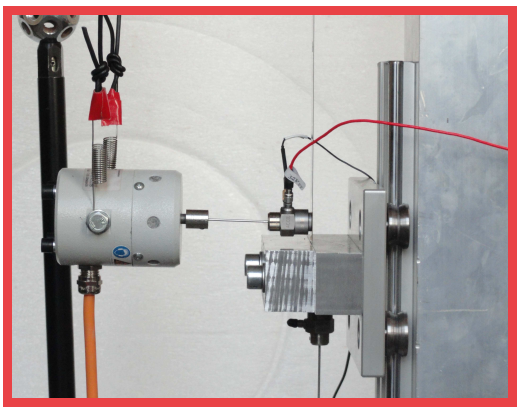

FIGURE 3.19 - Horizontal shaker picture.

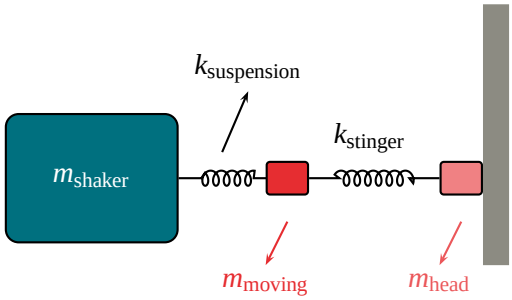

FIGURE 3.20 - Horizontal shaker modeling.

Parameter	*Symbol*	*Value*	*Units*
Shaker mass	m_{shaker}	1.7	kg
Moving mass	m_{moving}	15	g
Impedance head mass	m_{head}	30	g
Suspension stiffness	$k_{\text{suspension}}$	$4.0 \cdot 10^3$	N/m
Stinger stiffness	k_{stinger}	$4.5 \cdot 10^6$	N/m

TABLE 3.12 - Equivalent parameters of the spring-mass system modeling the horizontal shaker.

The influence of the impedance head is modeled by adding a concentrated mass m_{head} (equal to the mass of the impedance head) at the point where the horizontal shaker acts. The aluminum stinger connecting the shaker to the strip is replaced by a spring of stiffness coefficient

$$k_{\text{stinger}} = \left(\frac{EA}{L}\right)_{\text{stinger}}, \tag{3.8}$$

where E_{stinger} is the Young's modulus of the rod, A_{stinger} its cross section area and L_{stinger} its length. The values of these three parameters are given in Table 3.13.

Parameter	*Symbol*	*Value*	*Units*
Young's modulus	E_{stinger}	70	GPa
Cross section area	A_{stinger}	3.1	mm^2
Length	L_{stinger}	4.9	cm

TABLE 3.13 - Mechanical and geometrical properties of the aluminum stinger.

The shaker itself is modeled by two masses connected by a spring. The mass m_{shaker} represents the main body of the shaker and the mass m_{moving} corresponds to the small moving mass. The spring $k_{\text{suspension}}$ represents the moving mass suspension. The values of these three parameters are given in the technical sheet of the TIRA shaker [45].

This modification of the finite element model allows to better represent the first modes of the structure. The relative error on the higher natural frequencies is however of the order of 5% and the model still needs to be updated. The impedance head glued to the structure where the horizontal shaker acts prevents the strip from deforming and exhibiting significant curvature in this bottom region near the clamping (Fig. 3.21). Because the modes shapes characterized by a high curvature in this region are precisely the high frequency bending modes (Fig. 3.2), it is not surprising that the numerical model does not predict these natural frequencies with high accuracy. To reduce the errors, the stiffness of the two elements of the finite element model in contact with the impedance head is increased artificially. The increase in stiffness is determined to minimize the errors on the first height natural frequencies of the structure in a least square sense. The elementary stiffness matrices of the two elements are increased by 2%. It has also been checked that the number of elements near the clamping of the strip is sufficient to represent the boundary layer.

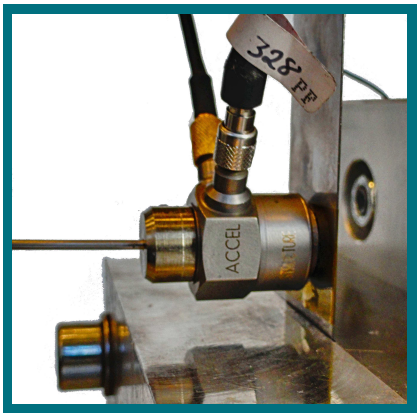

FIGURE 3.21 - Close-up on the impedance head/structure interaction.

This numerical model update allows to considerably reduce the errors on the natural frequencies. Table 3.14 summarizes the natural frequencies provided with the finite element model and with the experimental modal analysis. The relative errors are now acceptable.

	Frequency [Hz] TMA	*Frequency [Hz]* EMA	*Relative error [%]*
Bending mode 1	18.3	18.4	0.7
Bending mode 2	39.3	38.9	1.2
Bending mode 3	64.6	64.7	0.1
Bending mode 4	92.8	94.1	1.3
Torsion mode 1	102.0	101.2	0.7
Bending mode 5	116.8	118.1	1.1
Bending mode 6	147.2	145.8	0.9

TABLE 3.14 - Comparison of the eigenfrequencies obtained from theoretical (TMA, updated model) and experimental (EMA) modal analyses of the instrumented structure.

With respect to the theoretical modal analysis conducted on the non-instrumented structure, a new mode appears at low frequency. This mode is a deformation mode of the mass-spring system added to model the horizontal shaker. This is not a bending mode of the structure but a deformation mode of the shaker itself that will not be studied in the following and is not represented. The finite element bending modes are shown in Fig. 3.22 where the position of the horizontal shaker is indicated with a red marker.

Regarding the mode shapes, the MAC matrix is represented in Fig. 3.23. A good correlation is observed between the bending modes obtained numerically and experimentally for all the modes, except around the fifth bending mode. It was already observed in Fig. 3.18 that the frequency response function at this frequency is noisy. The coherence also drops on this frequency band. Moreover, a very high damping ratio of nearly 3% has been identified (Table 3.10). When exciting the structure around 118 Hz, it is observed (and heard) that the mechanical slider of the pre-stress mass shown in Fig. 2.12 seems to enter in resonance at these frequencies, which could explain the bad identification of the fifth bending mode. This is not a big issue: this mode will be avoided when performing the model reduction.

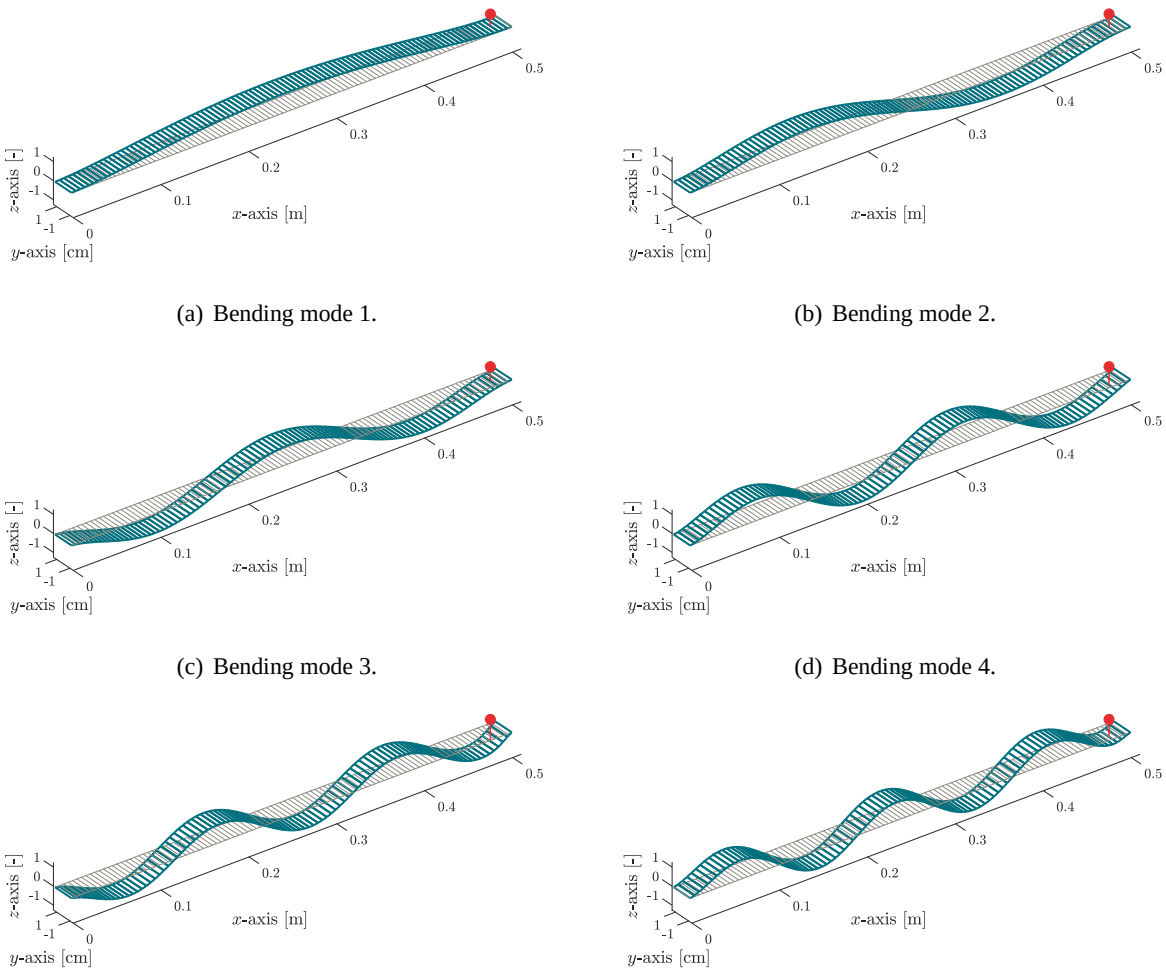

(a) Bending mode 1.

(b) Bending mode 2.

(c) Bending mode 3.

(d) Bending mode 4.

(e) Bending mode 5.

(f) Bending mode 6.

FIGURE 3.22 - The six first bending modes of vibration obtained in MATLAB with the updated model of the instrumented structure. The red marker allows to identify the position of the horizontal shaker.

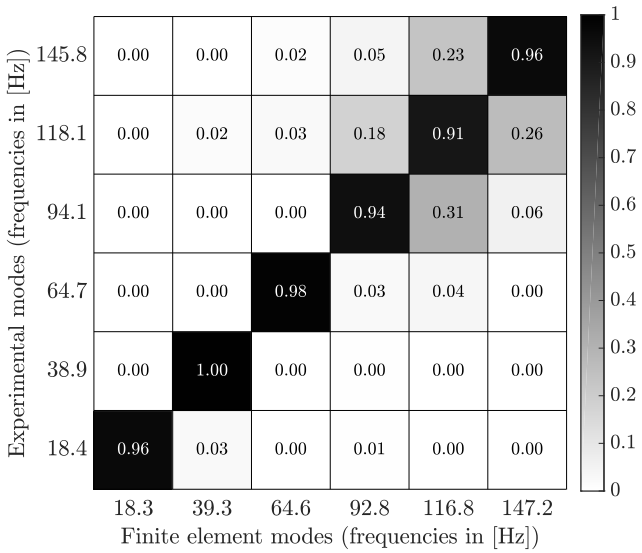

FIGURE 3.23 - MAC matrix between the numerical modes (updated model) and the experimental modes of the instrumented structure.

3.2.3 Damping

Damping is introduced in the conservative finite element model through a damping matrix **C** based on the experimentally identified damping ratios. The methodology introduced by Géradin and Rixen in [16] is followed. According to Rayleigh assumption, linearized viscous like dissipation with damping matrix **C** is assumed (*i.e.* no dissipation force present when the velocity is 0). The equation of motion takes therefore the general form

$$\mathbf{M}\ddot{\mathbf{x}}(t) + \mathbf{C}\dot{\mathbf{x}}(t) + \mathbf{K}\mathbf{x}(t) = \mathbf{f}(t), \tag{3.9}$$

where matrices **M** and **K** have been determined previously. In general, the modes are complex so that the equations are coupled and interactions occur between the modes. Defining $\mathbf{\Phi}$ as the modal matrix, the matrix $\mathbf{\Phi}^{\mathrm{T}}\mathbf{C}\mathbf{\Phi}$ is not diagonal and there is therefore no orthogonality relationship.

As shown previously, the modes identified experimentally can be considered in good approximation as real modes. The matrix $\mathbf{\Phi}^{\mathrm{T}}\mathbf{C}\mathbf{\Phi}$ is therefore supposed to be diagonal, with elements β_s on its diagonal. In the modal damping assumption, modal damping coefficients are defined by

$$\varepsilon_s = \frac{\beta_s}{2\omega_s\mu_s}, \tag{3.10}$$

where ω_s stands for the pulsation of mode $\mathbf{x}_{(s)}$ by analogy with one-degree-of-freedom systems and where

$$\mu_s = \mathbf{x}_{(s)}^{\mathrm{T}}\mathbf{M}\mathbf{x}_{(s)}. \tag{3.11}$$

A way to construct a damping matrix that guarantees diagonal modal damping is provided by the proportional damping approach

$$\mathbf{C} = \sum_{s=1}^{n} \mathbf{K}\mathbf{x}_{(s)} \frac{2\varepsilon_s}{\omega_s^3\mu_s} \mathbf{x}_{(s)}^{\mathrm{T}}\mathbf{K}. \tag{3.12}$$

In practice, only a small number m of modes are identified experimentally and **C** is computed as

$$\mathbf{C} = \sum_{s=1}^{m<n} \mathbf{K}\mathbf{x}_{(s)} \frac{2\varepsilon_s}{\omega_s^3\mu_s} \mathbf{x}_{(s)}^{\mathrm{T}}\mathbf{K}, \tag{3.13}$$

where the diagonal elements of the modal damping matrix $\mathbf{\Phi}^{\mathrm{T}}\mathbf{C}\mathbf{\Phi}$ are given by

$$\begin{cases} \beta_s = 2\varepsilon_s \omega_s \mu_s, & s \leqslant m \\ \beta_s = 0, & s > m \end{cases} \tag{3.14}$$

This automatically generates zero damping for the missing modes, which is not physical. The truncated expression is corrected by assuming for the higher modes a linearly increasing damping coefficient with frequency. It is assumed that the damping of the higher modes is governed by

$$\mathbf{C} = a\mathbf{K}, \tag{3.15}$$

so that

$$\varepsilon_s = \frac{a\omega_s}{2}, \qquad s > m, \tag{3.16}$$

and the diagonal elements of $\mathbf{\Phi}^{\mathrm{T}}\mathbf{C}\mathbf{\Phi}$ can be expressed as

$$\beta_s = a\omega_s^2 \mu_s, \qquad s > m. \tag{3.17}$$

The damping matrix is therefore built as

$$\mathbf{C} = a\mathbf{K} + \sum_{s=1}^{m<n} \mathbf{K}\mathbf{x}_{(s)} \left(\frac{2\varepsilon_s}{\omega_s^3 \mu_s} - \frac{a}{\omega_s^2 \mu_s} \right) \mathbf{x}_{(s)}^{\mathrm{T}} \mathbf{K}, \tag{3.18}$$

where the damping coefficients ε_s are identified experimentally (Table 3.10).

It has been shown that the finite element model reproduces in an accurate way the natural frequencies and mode shapes of the structure. To go one step further, the experimental and numerical frequency response functions can be compared. Fig. 3.24 compares the frequency response functions corresponding to excitation at point P9 and measurement at point P3. The blue curve is derived from the numerical finite element model where damping is taken into account through the damping matrix $\mathbf{C}$. A good agreement is observed between the curves. At the resonances, the peaks are, as expected, slightly shifted in frequency and the amplitudes are slightly different. This comparison gives confidence in the way damping is taken into account in the numerical model.

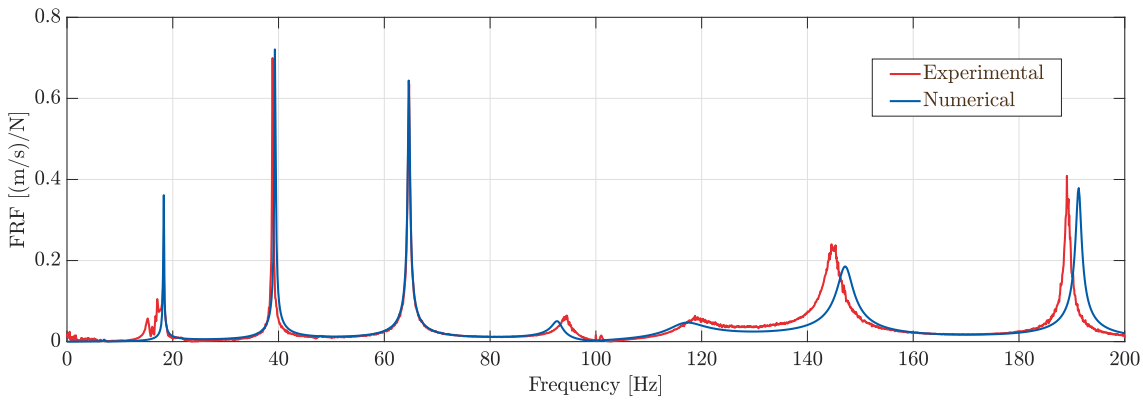

FIGURE 3.24 - Comparison of the frequency response functions (excitation at point P9, measurement at point P3) of the numerical finite element model and the experimental set-up.

3.3 Nonlinearities detection

Because of the lightness of the structure, it is expected that it can show nonlinear behaviors when it is subjected to high amplitude excitations. Such nonlinear behaviors must be avoided in the scope of the current study of the linear Mathieu equation. It is therefore important to identify when they occur. The modal analysis described in the previous section has been performed with very low excitation levels so that the structure behaves linearly. In order to highlight the nonlinear behavior of the strip, the structure is excited with the horizontal shaker with both sine-sweep excitations and simple sine excitations. These fully deterministic signals allow for an easy visual interpretation of the data.

The module MIMO Sweep & Stepped Sine Testing of the tool Test.Lab Structures Acquisition is used in this section for the acquisition of the response of the structure to sine-sweep excitations. Sine-sweep excitations allow to strongly activate nonlinearities as energy is concentrated in frequency. Linear sine-sweep excitations are selected to give the same importance to each frequency of the frequency band.

Sine-sweep excitations of increasing amplitudes are applied to the structure with the horizontal shaker to get a global view of the structure dynamics. The frequency varies linearly between 20 and 70 Hz at a sufficiently low rate of 0.05 Hz/s. This frequency interval covers two modes of the linear structure. Fig. 3.25 shows the envelope of the amplitude of the response of the structure measured at point P3 in terms of velocity for excitation amplitudes between 0.125 and 4 N. Each point $(f, \dot{x})$ of a curve corresponding to an excitation amplitude A relates the amplitude of the steady-state response of the structure $\dot{x}$ to a sine excitation of amplitude A and frequency f. When the amplitude of the excitation increases, the peaks in the response appear to be shifted towards the left. This is a compelling evidence of the existence of softening nonlinearities in the system when the amplitude excitation is sufficient. It can also be noted that the superposition principle does not apply here: multiplying the excitation amplitude by 2, does not multiply by the same factor the response of the structure. At low amplitudes (for excitations below 0.25 N), the linear behavior of the structure is recovered. Natural frequencies are independent of the level of excitation and the superposition principle is verified.

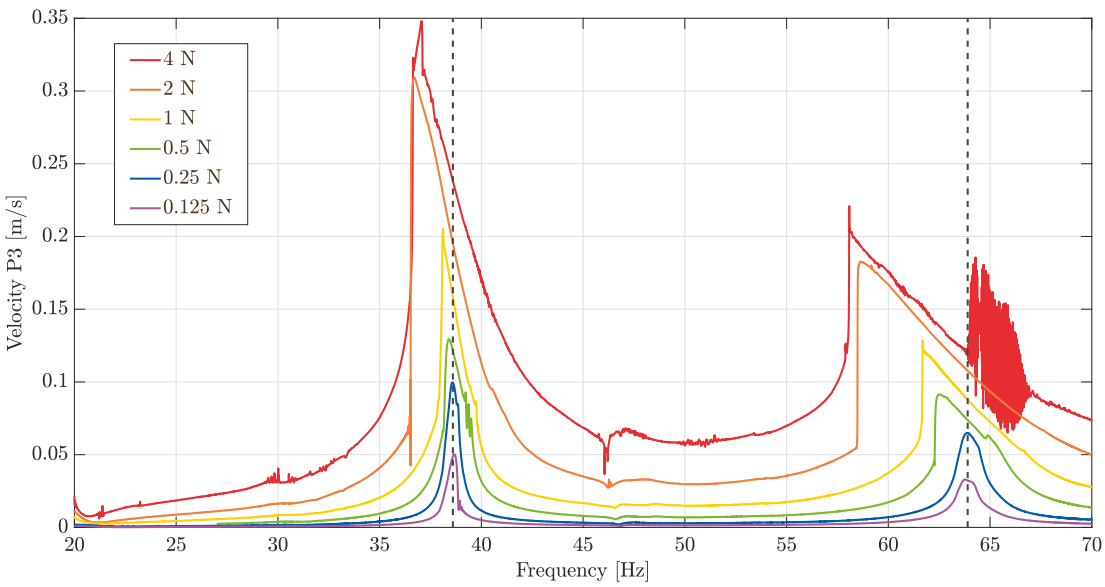

FIGURE 3.25 - Envelope of the velocity of the structure as a function of the frequency for sine-sweep excitations of amplitudes 0.125, 0.25, 0.5, 1, 2 and 4 N. Dashed lines indicate the respective positions of the two linear natural frequencies.

The comparison of the responses to sine-sweep excitation forces of equal amplitudes but reverse directions also provides interesting information about the nonlinear behavior of the system. The responses of the structure in terms of the velocity of point P3 to two sine-sweep excitation forces of amplitude 4 N and frequency varying linearly between 20 and 70 Hz are shown in Fig. 3.26. According to linear theory, both responses should superimpose, which is not the case for this amplitude of excitation. Nonlinear amplitude jumps are also observed in the response of the structure. At these jumps, the response of the structure appears to suddenly increase or decrease [18]. Fig. 3.27 shows the very different responses of the structure to sine excitations of amplitude 4 N and very close frequencies located just before and just after the jump. These jumps do not appear at the same frequencies for sine-sweep excitations of increasing or decreasing frequencies.

The shapes of the envelopes of the responses of the structure to sine-sweep excitations of increasing and decreasing frequencies suggest the shape of the nonlinear frequency response (NLFR). NLFRs describe the evolution of the steady-state response amplitude of the structure with the excitation amplitude and frequency [25]. For instance, it is expected that the nonlinear frequency response takes the form shown in Fig. 3.28 between 50 and 70 Hz. Contrary to linear FRF, several amplitudes of steady-state solutions can exist for a single frequency excitation. The solution is not unique but depends on the initial conditions. Initial conditions do not only influence the transient part of the response of a nonlinear system, but also its steady-state response [18]. However, all the solutions cannot be observed in practice and some regions of the NLFR are characterized as unstable. It is expected that, as in most nonlinear systems, the branch of the NLFR between points A and B is unstable. Therefore, only two different solutions can be observed for excitation frequencies between f_{B} and f_{A}.

Fig. 3.26 shows a non-smooth region around 65 Hz. This behavior cannot be explained by the linear theory. This suggests the existence of another nonlinear phenomenon. According to linear theory, the response of a system to a periodic solution is itself periodic. In this region, the periodic solution is periodically modulated. This illustrates the concept of quasiperiodicity well known in nonlinear theory [25]. The quasiperiodic response of the structure is represented in Fig. 3.29. The Fourier transform of this response confirms that two distinct frequencies are present in the response. Out of this region, the frequency content of the response of the structure is dominated by the excitation frequency.

The objective of this work is not to characterize the nonlinearities in the system neither to build a nonlinear numerical model of the structure but to study the linear Mathieu equation. In the following, the strip will be excited with sufficiently small force amplitudes to limit the excitation of the nonlinearities. It should also be noted that sine-sweep excitations are the worst case for nonlinearity since all the energy is concentrated on a single frequency. In the following, random excitations with energy content distributed on a finite frequency band will be applied. Moreover, random excitations have the characteristics of averaging slight nonlinearities [3]. At the end of this report (section 5.2.3), some experimental results obtained in the nonlinear domain will nevertheless be shown.

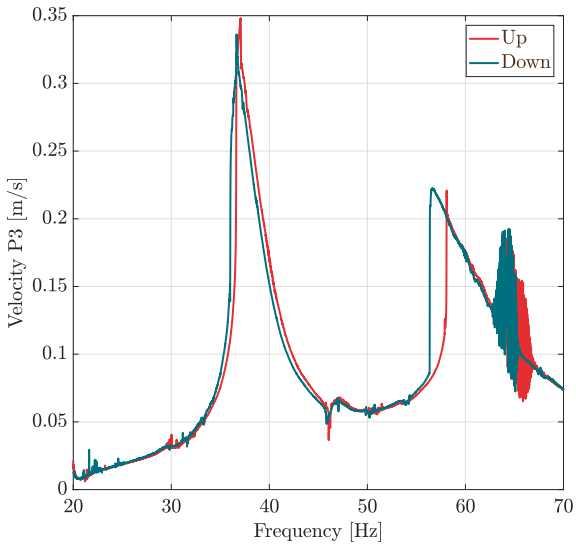

FIGURE 3.26 - Velocity at point P3 as a function of the frequency for sine-sweep excitations of amplitude 4 N in up and down senses.

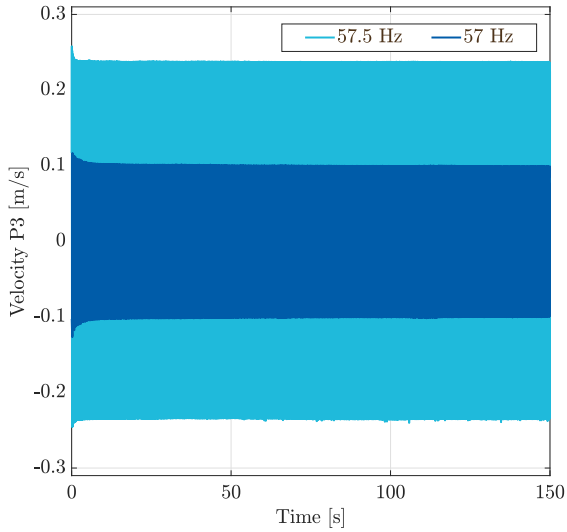

FIGURE 3.27 - Time evolution of the velocity at point P3 for sine excitations of amplitude 4 N and frequencies 57 and 57.5 Hz.

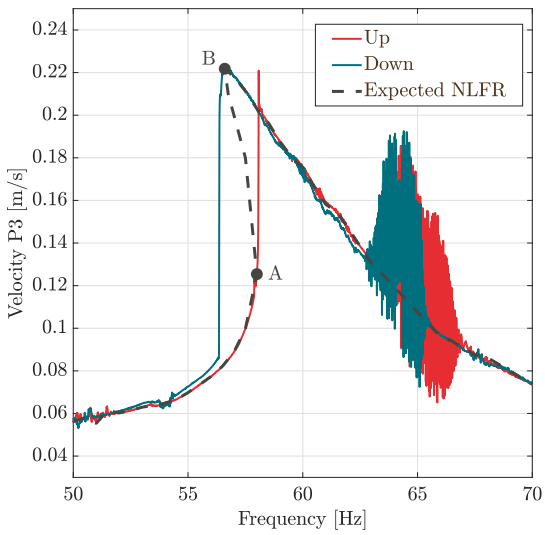

FIGURE 3.28 - Velocity at point P3 as a function of the frequency for sine-sweep excitations of amplitude 4 N in up and down senses and expected NLFR.

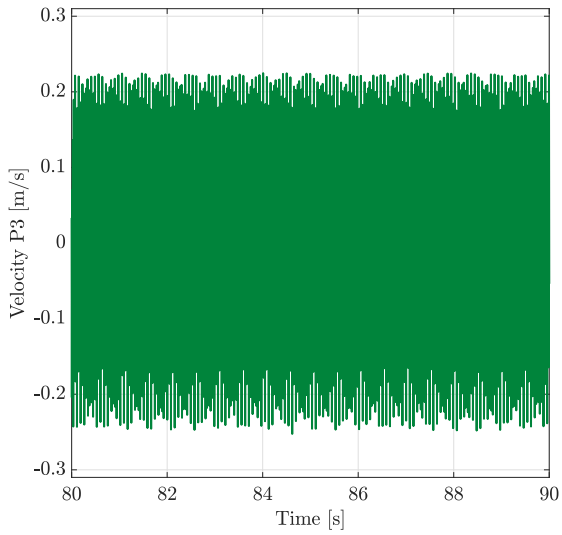

FIGURE 3.29 - Time evolution of the velocity at point P3 for sine excitation of amplitude 4 N and frequency 65 Hz. Illustration of the quasiperiodiciy nonlinear phenomenon.

PART 4

NUMERICAL STUDY OF FIRST PASSAGE TIME

This chapter is dedicated to the numerical study of first passage time using the finite element model of the structure introduced and validated in the previous part. This study is carried out in order to prepare the experimental validation described in the next chapter.

The analytical theory of first passage time summarized in section 1.2 applies to one-degree-of-freedom structures governed by the linear Mathieu equation and subjected to broadband forced and parametric excitations. The studied multi-degree-of-freedom structure is subjected to forced and parametric excitations and its dynamics is governed by a multi-dimensional Mathieu equation. In order to fit into the particular framework defined by the theory, several steps have therefore to be taken.

In the first section, the multi-degree-of-freedom equations of motion are reduced to a set of uncoupled single-degree-of-freedom equations. It is then shown that, for specific forced and parametric excitations, some aspects of the dynamics of the structure can indeed be approximated with a single-degree-of-freedom Mathieu equation. This study of the validity of the reduced model will naturally lead to introduce the concept of narrow-band excitations and the necessity to study numerically their influence. The second section therefore reports the results of a numerical study designed to analyze the influence of the frequency bands of the random excitations on the first passage time map. Some general conclusions are drawn and used to define the parametric and forced excitations to be applied in the experimental study of the structure.

4.1 From multiple-degree-of-freedom to single-degree-of-freedom equations of motion

This section describes the first step towards relating the complex reality of the physical set-up to the framework under which the analytical results of section 1.2 have been derived. It focuses on the assumption of single-degree-of-freedom system of the theory. In this section, the multi-degree-of-freedom equations of motion are reduced to a set of uncoupled single-degree-of-freedom Mathieu equations. The conditions under which a profitable use of this model reduction can be done are then identified.

4.1.1 Model reduction

The finite element modeling of the N-degree-of-freedom structure provides the mass matrix $\mathbf{M}$, the damping matrix $\mathbf{C}$ and the time-varying stiffness matrix $\mathbf{K}(t)$. The governing equation of the structure subjected to an external excitation $\mathbf{f}(t)$ therefore writes

$$\mathbf{M}\ddot{\mathbf{x}}(t) + \mathbf{C}\dot{\mathbf{x}}(t) + \mathbf{K}(t)\mathbf{x}(t) = \mathbf{f}(t), \tag{4.1}$$

where $\mathbf{x}$ is the vector of generalized coordinates. The stiffness matrix $\mathbf{K}(t)$ can be decomposed into a sum of three terms

$$\mathbf{K}(t) = \mathbf{K}_0 + \mathbf{K}_{\text{prestress,init}} + \mathbf{K}_{\text{prestress}}(t), \tag{4.2}$$

where $\mathbf{K}_0$ is the usual linear stiffness matrix (constant in time), $\mathbf{K}_{\text{prestress,init}}$ is the geometrical stiffness matrix due to the initial pre-stress mass (constant in time) and $\mathbf{K}_{\text{prestress}}(t)$ varies in time and characterizes the modulation of the stiffness induced by the zero mean parametric excitation $F_u(t)$. If $\mathbf{K}_{\text{prestress,1}}$ denotes the stiffness matrix due to the application of a unit parametric force to the structure, the third term of equation (4.2) can be expressed as

$$\mathbf{K}_{\text{prestress}}(t) = F_u(t)\mathbf{K}_{\text{prestress,1}}. \tag{4.3}$$

The stiffness matrices $\mathbf{K}_0$ and $\mathbf{K}_{\text{prestress,init}}$ have been introduced in section 3.1.1. The stiffness matrices $\mathbf{K}_{\text{prestress,1}}$ and $\mathbf{K}_{\text{prestress,init}}$ are obviously related by

$$\mathbf{K}_{\text{prestress,1}} = \frac{\mathbf{K}_{\text{prestress,init}}}{m_{\text{prestress}}g}. \tag{4.4}$$

The response of the structure $\mathbf{x}(t)$ can be written in the modal basis as

$$\mathbf{x}(t) = \mathbf{\Phi}\mathbf{q}(t), \tag{4.5}$$

where $\mathbf{\Phi}$ is the modal matrix (each column of $\mathbf{\Phi}$ corresponds to a mode of the structure) and $\mathbf{q}(t)$ is the vector of modal coordinates. Pre-multiplying the dynamical equation (4.1) by $\mathbf{\Phi}^{\mathrm{T}}$ and introducing (4.5) gives

$$\mathbf{\Phi}^{\mathrm{T}}\mathbf{M}\mathbf{\Phi}\ddot{\mathbf{q}}(t) + \mathbf{\Phi}^{\mathrm{T}}\mathbf{C}\mathbf{\Phi}\dot{\mathbf{q}}(t) + \mathbf{\Phi}^{\mathrm{T}}\mathbf{K}(t)\mathbf{\Phi}\mathbf{q}(t) = \mathbf{\Phi}^{\mathrm{T}}\mathbf{f}(t). \tag{4.6}$$

Defining modal matrices and vectors as the projections of the physical structural matrices and vectors in the modal basis by

$$\mathbf{M}^* = \mathbf{\Phi}^{\mathrm{T}}\mathbf{M}\mathbf{\Phi}, \qquad \mathbf{C}^* = \mathbf{\Phi}^{\mathrm{T}}\mathbf{C}\mathbf{\Phi}, \tag{4.7}$$

$$\mathbf{K}^* = \mathbf{\Phi}^{\mathrm{T}}\mathbf{K}_0\mathbf{\Phi} + \mathbf{\Phi}^{\mathrm{T}}\mathbf{K}_{\text{prestress,init}}\mathbf{\Phi}, \qquad \mathbf{K}^*_{\text{prestress,1}} = \mathbf{\Phi}^{\mathrm{T}}\mathbf{K}_{\text{prestress,1}}\mathbf{\Phi} \tag{4.8}$$

and

$$\mathbf{f}^*(t) = \mathbf{\Phi}^{\mathrm{T}}\mathbf{f}(t), \tag{4.9}$$

the equation governing the dynamics of the modal coordinates is written as

$$\mathbf{M}^*\ddot{\mathbf{q}}(t) + \mathbf{C}^*\dot{\mathbf{q}}(t) + [\mathbf{K}^* + F_u(t)\mathbf{K}^*_{\text{prestress,1}}]\mathbf{q}(t) = \mathbf{f}^*(t). \tag{4.10}$$

In the ideal case where the modal matrices $\mathbf{M}^*$, $\mathbf{C}^*$, $\mathbf{K}^*$ and $\mathbf{K}^*_{\text{prestress,1}}$ are diagonal, the N equations of system (4.10) can be decoupled and the dynamics of the structure in the different deformation modes can be studied separately. In such a case, the N-degree-of-freedom system behaves like N single-degree-of-freedom systems. The modal matrices $\mathbf{M}^*$ and $\mathbf{K}^*$ are diagonal by definition. The matrix $\mathbf{C}^*$ is also diagonal under the modal damping assumption (section 3.2.3). There is no reason for the matrix $\mathbf{K}^*_{\text{prestress,1}}$ to be perfectly diagonal. In the current study, its diagonal elements are only one order of magnitude larger than its out-of-diagonal elements. As long as the products of $F_u(t)$ by the out-of-diagonal terms of $\mathbf{K}^*_{\text{prestress,1}}$ are well below the diagonal terms of $\mathbf{K}^*$, the coupling between the modes is small. In the following, only small amplitude parametric excitations will be considered to limit the excitation of nonlinearities and to keep a quasi-Hamiltonian system. It is therefore expected that this condition will be verified in good approximation.

When the modal matrices are diagonal, the equations of motion can be decoupled for each modal coordinate. According to the conventions introduced by Ewins in [15], the diagonal elements of the modal

matrices are referred to as the modal masses, modal damping ratios and modal stiffnesses. There is however no unique value for these modal parameters as they are directly related to the scaling method used to define the mode shape eigenvectors. Ewins therefore introduces effective parameters defined for a given mode i at a given degree-of-freedom r by normalizing the modal parameters by the square of the value of mode i at degree-of-freedom r. The effective parameters are unique and form a useful description of the underlying behavior of the structure point by point and mode by mode. Eventually, Ewins introduces generalized properties that are referred to as unique properties of each mode. They are defined as the effective properties at the degree-of-freedom with the largest amplitude of response in the mode.

The single-degree-of-freedom equation governing the i-th modal coordinate $z(t) = q_i(t)$ takes therefore the form

$$m_{\text{eq}}\ddot{z}(t) + c_{\text{eq}}\dot{z}(t) + [k_{\text{eq}} + F_u(t)k_{\text{p,eq}}]z(t) = p(t). \tag{4.11}$$

Using Ewins' approach, the generalized mass, damping ratio and stiffness coefficients in this equation are defined by

$$m_{\text{eq}} = \frac{\mathbf{M}^*(i,i)}{[\mathbf{\Phi}(n_i,i)]^2}, \qquad c_{\text{eq}} = \frac{\mathbf{C}^*(i,i)}{[\mathbf{\Phi}(n_i,i)]^2}, \qquad k_{\text{eq}} = \frac{\mathbf{K}^*(i,i)}{[\mathbf{\Phi}(n_i,i)]^2} \quad \text{and} \quad k_{\text{p,eq}} = \frac{\mathbf{K}^*_{\text{prestress,1}}(i,i)}{[\mathbf{\Phi}(n_i,i)]^2}, \tag{4.12}$$

where n_i is the degree-of-freedom with the largest amplitude of response in mode i. The participation factor of the forced excitation to mode i is given by

$$p(t) = \frac{\mathbf{\Phi}(n_{F_w},i)}{[\mathbf{\Phi}(n_i,i)]^2}F_w(t) = \alpha F_w(t), \tag{4.13}$$

where n_{F_w} is the degree of freedom where the forced excitation F_w is applied.

If the multi-degree-of-freedom system is vibrating in mode j only, $q_i(t) = 0\ \forall\, i \neq j$ and the response of the structure is given by

$$\mathbf{x}(t) = \mathbf{\Phi}\mathbf{q}(t) = \mathbf{\Phi}_j\, q_j(t), \tag{4.14}$$

so that the solution $z(t)$ of the single-degree-of-freedom system characterized by (4.11) is directly related to the real displacement of the structure.

In conclusion, for parametric excitations of sufficiently small amplitude, the responses of the structure in each of its mode can be decoupled. If the structure is excited in such a way that it responds only (or mainly) in a unique mode, then the response of the structure at a given point is the solution of an equivalent one-degree-of-freedom equation of the form (4.11), which is a linear Mathieu equation.

4.1.2 Validity of the single-degree-of-freedom governing equation

The objective of this section and the next two is to identify numerically under which excitations the solution of the one-dimensional equation (4.11) provides a sufficiently accurate approximation of the solution of the multi-dimensional equation (4.1) at a given point of the strip. In other words, these sections aim at answering the question: "What excitations should be applied to the structure so that the equations of motion are decoupled and the strip only responds in a single mode?". In a first step, deterministic excitations are applied to the structure (section 4.1.3). This helps drawing some general conclusions used in the second step where the same numerical experiment is carried out with stochastic excitations (section 4.1.4).

In order to identify the conditions under which an efficient use of the reduction of the multi-degree-of-freedom system can be done, both one-degree-of-freedom and multi-degree-of-freedom equations of motion are integrated using a Newmark integration scheme (see appendix B for more details). On the one hand, the governing equations of the multi-degree-of-freedom system (4.1) subjected to given forced and

parametric excitations are solved and the response at an antinode of vibration of the studied mode is extracted. On the other hand, the reduced one-degree-of-freedom equation of motion (4.11) is solved for the same excitations. The objective is to determine the characteristics of the excitations that ensure that both responses agree in good approximation. The responses are compared at an antinode of vibration in order to minimize the influence of the other modes.

The next question to answer is the choice of the mode used for the reduction. Several aspects of the problem have to be taken into account, keeping in mind the final objective of the work: the experimental validation of the theory of first passage time described in section 1.2. First, the equivalent parameters of the selected mode must allow to cover the largest possible part of the first passage time in a reasonable amount of time. This will be detailed further (section 5.1.2). Then, in order to have equations of motion highly decoupled, the selected mode must be such that the out-of-diagonal terms of $\mathbf{K}_{\text{prestress},1}$ are sufficiently small with respect to the diagonal elements. The structure must also respond in a single mode. The selected mode therefore has to be sufficiently far from the others in frequency to avoid exciting them. The first numerical mode is avoided since it does not correspond to a deformation mode of the structure but to a mode of the shaker. The first bending mode is also rejected to avoid the risk of exciting the shaker mode. Based on these remarks, the second bending mode is studied in the following. It is characterized by the equivalent parameters

$$k_{\text{p,eq}} = 39 \text{ m}^{-1}, \qquad k_{\text{eq}} = 3273 \text{ Nm}^{-1}, \qquad c_{\text{eq}} = 0.08 \text{ N[m/s]}^{-1} \quad \text{and} \quad m_{\text{eq}} = 0.05 \text{ kg}. \tag{4.15}$$

The frequency of this second bending mode is $f_0 = 39.3$ Hz.

4.1.3 Validity of the reduction for deterministic excitations

As a first step, the system is studied under deterministic (and more precisely harmonic) excitations. First, the instabilities of the structure are illustrated. Then, the influence of the forced and parametric excitations are studied separately. For each excitation condition, both the single-degree-of-freedom and the multi-degree-of-freedom equations of motion are solved and the responses are compared.

Instabilities

As pointed out in section 1.1, the system under study can exhibit two different kinds of instabilities, namely simple instabilities when the forced excitation frequency is equal to a natural frequency f_{nat} of the structure and parametric instabilities when the parametric excitation has a frequency equal to $2f_{\text{nat}}/k$ where k is an integer. These issues are shortly addressed here to gain useful insight for understanding the results below.

Fig. 4.1 shows the responses of the single-degree-of-freedom and multi-degree-of-freedom undamped systems to a forced excitation at the frequency of the selected mode f_0. No parametric excitation is considered. As expected, the response envelope grows linearly with time. The structure responds quasi exclusively in a single mode and the instability is well captured by the model reduction.

Fig. 4.2 illustrates the concept of parametric instability. The strip is excited with a parametric excitation at twice the frequency of the second bending mode of the structure. No damping, nor forced excitation is considered. As expected, the response grows exponentially. Here again, the single-degree-of-freedom equation does a good job and provides an accurate description of the dynamics of the instability. Numerical simulations also show that higher parametric excitation amplitudes are required to observe an instability when damping or forced excitation are considered. This has already been mentioned in section 1.1. The other parametric resonances of the second bending mode (at f_0, $2/3 f_0$, ...) are also much more sensitive to forced excitation or damping. In conclusion, parametric instabilities are well captured by the model reduction. They occur for slightly damped modes when the forced excitation is sufficiently small. As expected, the second harmonic is the most critical.

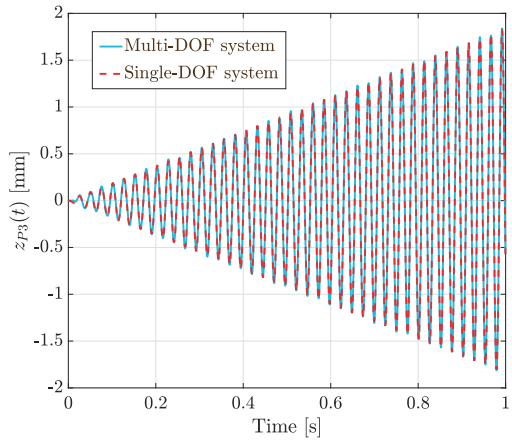

FIGURE 4.1 - Comparison of the temporal responses of the single- and multi-DOF undamped motion equations to a forced excitation of amplitude 1 N and frequency f_0.

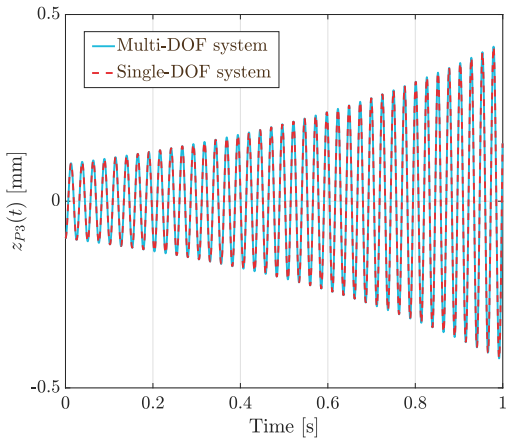

FIGURE 4.2 - Comparison of the temporal responses of the single- and multi-DOF undamped motion equations to a parametric excitation of amplitude 2 N and frequency $2f_0$.

Forced excitation

Obviously, the model reduction requires that the second bending mode of the structure is the only one to be excited. To avoid exciting the other structural modes, the frequency of the forced excitation must therefore be close to the selected natural frequency f_0. For the particular system considered here, numerical experiments show that the dynamics can be described by the single-degree-of-freedom equation if the frequency of the forced excitation lies between $0.95f_0$ and $1.05f_0$. As shown in Fig. 4.3, the time responses of the single-degree-of-freedom and multi-degree-of-freedom systems superimpose nicely when the structure is excited at the frequency $1.05f_0$. The solution is damped and a phenomenon of beating is observed. When the forced excitation has a frequency outside the interval $[0.95f_0\ ;\ 1.05f_0]$, other modes of the multi-degree-of-freedom structure are excited and the responses do not match.

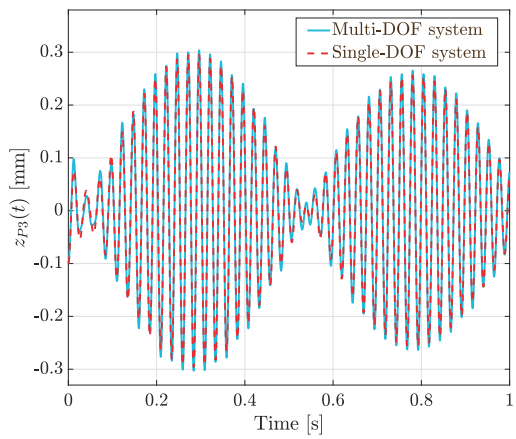

FIGURE 4.3 - Comparison of the temporal responses of the single- and multi-DOF damped motion equations to a forced excitation of amplitude 1 N and frequency $1.05f_0$.

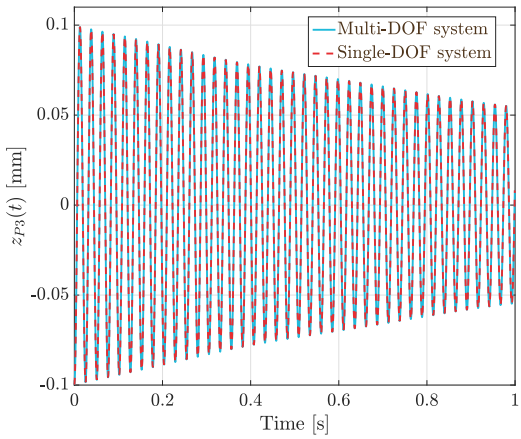

FIGURE 4.4 - Comparison of the temporal responses of the single- and multi-DOF damped motion equations to a parametric excitation of amplitude 0.1 N and frequency $1.95f_0$.

Parametric excitation

Regarding the amplitude of the parametric excitation, it should be noted that F_u cannot exceed the prestress of the strip. When this is the case, the multi-degree-of-freedom system becomes unstable and the single-degree-of-freedom system cannot reproduce this instability. In fact, in the single-degree-of-freedom model, F_u only modifies the stiffness of the strip but does not act as an external force applied to the system. In the multi-degree-of-freedom system, the low compression stiffness of the strip is modeled and leads to strip instabilities. It is therefore important to keep F_u lower than $m_{\text{prestress}}g = 17.8$ N to ensure the integrity of the structure and the correspondence between the single- and multi-degree-of-freedom equations of motion. Since the shakers used in the experimental set-up cannot apply a force larger than 9 N, this will not be an issue (section 2.3). Moreover, as detailed in section 4.1.1, the equations decoupling remains valid as long as the diagonalization of the equations is valid. F_u should therefore remain sufficiently small so that the out-of-diagonal elements of $F_u(t)\mathbf{K}^*_{\text{prestress},1}$ remain small with respect to the diagonal elements of $\mathbf{K}^*$. Finally, the parametric excitation should remain sufficiently low so that the modes of the structure are not significantly affected.

Regarding the frequency of the parametric excitation, a good match between the responses of the single-degree-of-freedom and multi-degree-of-freedom equations of motion is observed provided that the second bending mode dominates the response of the structure. Numerical simulations show that this is the case when the frequency of the parametric excitation is sufficiently close to the natural frequency of the mode f_0 or its second harmonic $2f_0$ (Fig. 4.4). When this is not the case, other modes of the multi-degree-of-freedom structure are excited.

4.1.4 Validity of the reduction for stochastic excitations

Now that the dynamics of the deterministic system is well understood, the same reasoning is followed in the case of stochastic excitations. The general conclusions drawn for deterministic excitations are used as a starting point to draw conclusions valid when the structure is subjected to stochastic excitations. To fit in the framework of the analytical results of section 1.2, the forced and parametric excitations are characterized by constant power spectral densities $\tilde{S}_w$ and $\tilde{S}_u$ (more details in appendix A). It is however rapidly observed that these excitations cannot be defined as broadband processes since this causes the excitation of different modes of the structure so that the responses of the single- and multi-degree-of-freedom systems do not match. Forced and parametric excitations are therefore defined as narrow-band processes.

Forced excitation

The forced excitation is defined in a limited frequency band centered on f_0. When the band covers more than the second bending mode, several modes are excited and the single- and multi-degree-of-freedom equations of motion do not provide the same response at all.

When the system is subjected to forced excitation only, a good match is observed as long as the frequency band is contained in $[0.8f_0\,;\,1.2f_0]$ (Fig. 4.5(a)). This interval is wider than the one identified in the deterministic case. In fact, some compensation happens between the response components at frequencies $f_0+\Delta f$ and $f_0-\Delta f$.

When the frequency interval is expanded beyond $[0.8f_0\,;\,1.2f_0]$, the closest modes are excited in such a way that the two responses do not superimpose perfectly. Fig. 4.5(b), for instance, shows the two temporal responses to a forced excitation defined on the frequency band $[0.6f_0\,;\,1.4f_0]$. Although this band does not include any other mode of the structure, other bending modes are nevertheless excited.

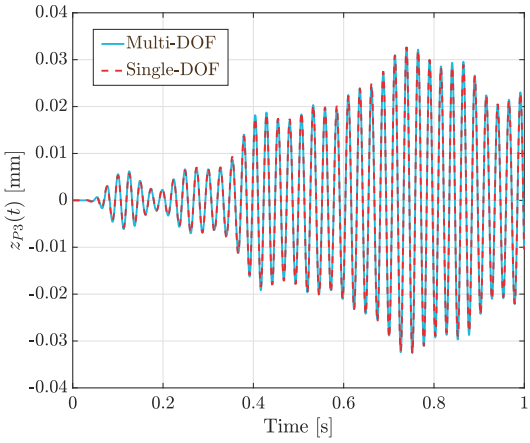

(a) F_w defined on $[0.8 f_0\,;1.2 f_0]$.

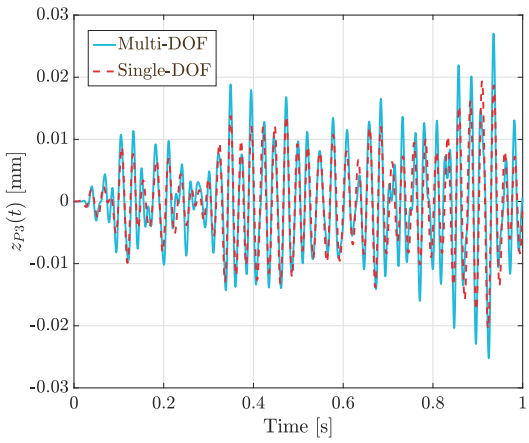

(b) F_w defined on $[0.6 f_0\,;1.4 f_0]$.

FIGURE 4.5 - Comparison of the temporal responses of the single- and multi-DOF damped motion equations to a forced excitation of power spectral density $\tilde{S}_w = 10^{-4}$ N^2/Hz.

Parametric excitation

When the system is only subjected to parametric excitation, the responses coincide as long as the frequency band of F_u includes the second harmonic of the second bending mode but does not include the second harmonics of other modes. It should however be noted that the second harmonic of highly damped modes can be included in the interval without degrading the accuracy of the solution. When damping differs from zero, the other harmonics of the other modes do not need to be avoided.

When forced excitation is added, the responses of both models remain close as long as the intensity of the parametric excitation $\tilde{S}_u$ is not too high with respect to $\tilde{S}_w$. In practice, $\tilde{S}_u$ should not exceed $\tilde{S}_w$ by more than a factor 100 (see Fig. 4.6 for F_w defined on $[0.8 f_0\,;1.2 f_0]$, F_u defined on $[0.8 f_0\,;2.4 f_0]$ and different ratios $\tilde{S}_u/\tilde{S}_w$). It should be noted that the interval of F_u contains the second harmonic of the first bending mode and the first harmonic of the third bending mode. Because these modes are sufficiently damped, this does not deteriorate the validity of the model reduction.

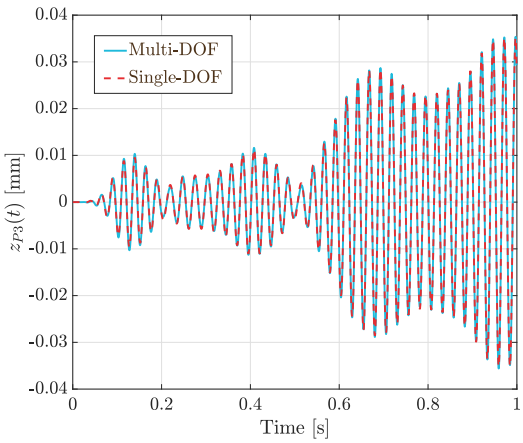

(a) $\tilde{S}_u = 10^{-4}$ N^2/Hz.

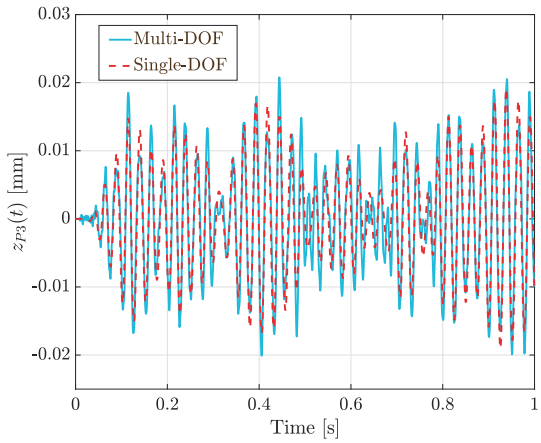

(b) $\tilde{S}_u = 10^{-1}$ N^2/Hz.

FIGURE 4.6 - Comparison of the temporal responses of the single- and multi-DOF damped motion equations to F_w of intensity $\tilde{S}_w = 10^{-4}$ N^2/Hz on $[0.8 f_0\,;1.2 f_0]$ and F_u on $[0.8 f_0\,;2.4 f_0]$.

4.2 Influence of narrow-band excitations on the first passage time

The analytical results of the first passage time derived in [36, 37] are based on three conditions. The system has to be governed by a single-degree-of-freedom equation of motion, it must be linear and subjected to broadband excitations. The previous section has allowed to show that some aspects of the dynamics of the structure studied are governed by a linear single-degree-of-freedom motion equation. Indeed, as a result of the reduction of the N-degree-of-freedom system into N single-degree-of-freedom systems, the dynamic behavior of the system is governed by N equations that take the general form (4.11). Each of these equations has the form of the linear single-degree-of-freedom Mathieu equation presented in part 1. The conditions under which the reduced model can be used have also been determined and show that the bandwidths of the forced and parametric excitations have to be limited. With the designed structure, it is therefore not possible to meet at the same time the condition of single-degree-of-freedom system and the condition of broadband excitations.

Because no analytical results are currently available for the first passage time of systems subjected to colored excitations, a numerical study of the influence of the frequency bands of the excitations is required and is carried out in this section. The oscillator is numerically studied in its dimensionless form characterized by the governing equation

$$\ddot{x}(t) + 2\xi\dot{x}(t) + [1 + u(t)]x(t) = w(t). \tag{4.16}$$

4.2.1 Introduction of the tools used in the study of narrow-band processes

First passage time maps are obtained numerically using Monte Carlo simulations. The response of the one-degree-of-freedom system in terms of displacement and velocity is computed at each time step using a Newmark integration scheme (see appendix B for more details) and the Hamiltonian H of the system is computed. When H reaches a given maximal value, the simulation is stopped and a new simulation is initiated. The average first passage time is eventually obtained by averaging the results of a large set of simulations. This approach allows to have a uniform quality of the map in the whole space $(H_0^*, \Delta H^*)$ as the averaging is based on the same number of samples at each point of the map.

Before studying the influence of narrow-band excitations, the methodology followed to compute first passage time maps and its implementation are validated by applying it to a system subjected to broadband excitations. The different parameters used in the simulation are $a = 0$, $S_u = 10^{-3}$ and $S_w = 5 \cdot 10^{-4}$. Fig. 4.7 compares the first passage time maps obtained analytically with results provided in section 1.2.2 and numerically with Monte Carlo simulations using 20 000 samples. A perfect match is observed.

The mean square first passage time map obtained with these 20 000 samples is represented in Fig. 4.8(a). More samples are required to smooth the curves in the bottom right corner. As shown in section 1.2.2, this corner is characterized by a high coefficient of variation and the solution converges more slowly in this region. The global trend is however recovered. Fig. 4.8(b) shows that 200 000 samples are required to obtain a smooth behavior in the bottom right corner. Because this computation is relatively heavy, the systematic study performed in the following sections to analyze the influence of the frequency bands of the excitations will be limited to the study of the average first passage time map.

The Monte Carlo approach can be used to build numerically the first passage time map of a system subjected to forced and parametric excitations defined as narrow-band random processes (see appendix A for more details on the numerical generation of stochastic processes). The procedure is first applied to an undamped system subjected to a parametric excitation with $S_u = 10^{-3}$ uniform on the frequency interval $[0.1 f_0 ; 3 f_0]$ and a forced excitation with $S_w = 5 \cdot 10^{-4}$ uniform on the frequency interval $[0.8 f_0 ; 1.2 f_0]$.

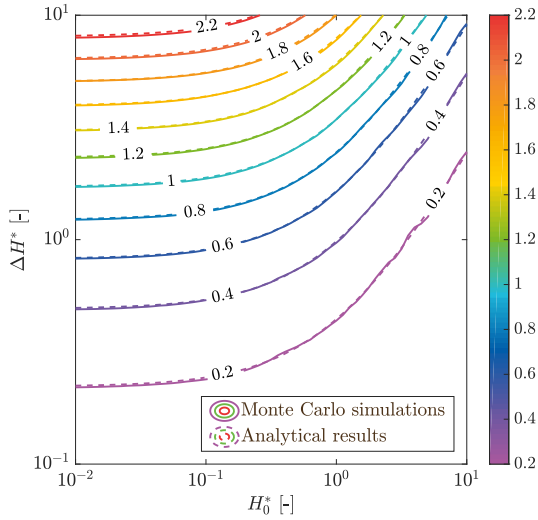

FIGURE 4.7 - Comparison of the reduced average first passage time $U_1 S_u/4$ maps obtained numerically and analytically for broadband excitations ($a = 0$, $S_u = 10^{-3}$, $S_w = 5 \cdot 10^{-4}$).

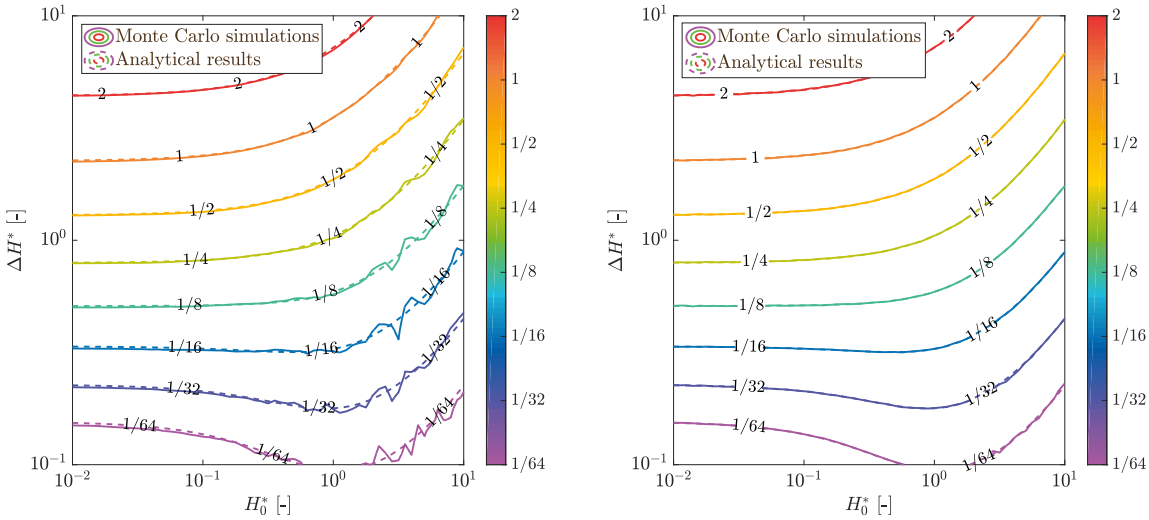

(a) $n = 20\,000$ samples.

(b) $n = 200\,000$ samples.

FIGURE 4.8 - Comparison of the reduced mean square first passage time $U_2 S_u^2/32$ maps obtained numerically and analytically for broadband excitations ($a = 0$, $S_u = 10^{-3}$, $S_w = 5 \cdot 10^{-4}$).

Before analyzing the results, it is important to check the convergence of the Monte Carlo simulations, *i.e.* that enough samples are used to compute the mean first passage time. Fig. 4.9 shows the influence of the number of samples on the calculated reduced mean first passage time for five points distributed on the $(H_0^*, \Delta H^*)$ map. As suggested in [4], a logarithmic scale is preferred on the horizontal axis. Indeed, the RMS value of the mean estimator scales with $1/\sqrt{n}$. In other words, if $n = 100$, 300 supplementary samples are expected to decrease the uncertainties by a factor 2. If $n = 1000$, 3000 additional realizations are needed for the same reduction. This behavior is naturally apparent with the logarithmic scale. Fig. 4.9 suggests that $n = 20\,000$ samples are sufficient to estimate the mean first passage time. This gives confidence in the map obtained and shown in Fig. 4.10. This is also confirmed by the validation shown in Fig. 4.7 in the case of broadband excitations.

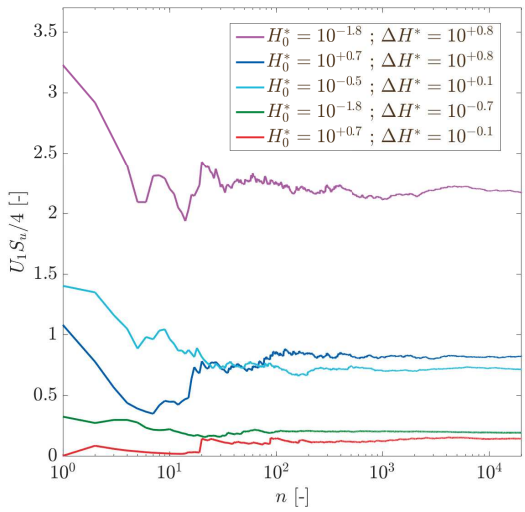

FIGURE 4.9 - Convergence of the reduced average first passage time $U_1 S_u/4$ at five distinct points of the map with the number of samples ($a = 0$, $S_u = 10^{-3}$, $S_w = 5 \cdot 10^{-4}$, u on $[0.1 f_0 ; 3 f_0]$ and w on $[0.8 f_0 ; 1.2 f_0]$).

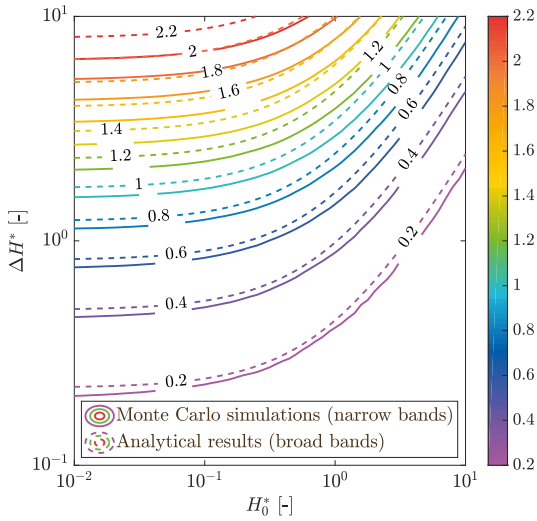

FIGURE 4.10 - Comparison of the reduced average first passage time $U_1 S_u/4$ maps obtained numerically for narrow-band excitations (u on $[0.1 f_0 ; 3 f_0]$ and w on $[0.8 f_0 ; 1.2 f_0]$) and analytically for broadband excitations ($a = 0$, $S_u = 10^{-3}$, $S_w = 5 \cdot 10^{-4}$).

Visual inspection of the maps (Fig. 4.10) reveals that the analytical results are not recovered when the system is subjected to narrow-band random processes. Although the additive, multiplicative and incubation regimes can still be clearly identified, the curves do not superimpose. This shows that the analytical results obtained for broadband excitations do not simply transfer to narrow-band random processes. Here, the frequency bands are limited and the corresponding first passage times are larger than those computed with broadband excitations. This is easily explained by the fact that, when the frequency band is wider, more rapid oscillations are added to the solution and decrease the first passage time.

To further analyze the difference between the broadband analytical results and the narrow-band numerical ones, indicators are defined to get a quantitative vision of the problem. The objective is to quantify the distance between the two results and to decide whether this difference is significant or not.

As a first step, a distance between the two sets of results is defined. If Z_{BB} denotes the mean first passage time matrix expected under broadband excitations at each point of the map, and Z_{NB} the one obtained with the Monte Carlo simulations of the system subjected to narrow-band excitations, a RMS distance Δ between the two first passage time maps is defined as

$$\Delta = \sqrt{\frac{1}{N} \sum_i \sum_j \left[\frac{(Z_{\mathrm{BB}})_{i,j} - (Z_{\mathrm{NB}})_{i,j}}{(Z_{\mathrm{BB}})_{i,j}} \right]^2}, \tag{4.17}$$

where N is the number of data points in the comparison. It was observed in Fig. 4.8(a) that convergence is slower in the bottom right corner of the map. The corresponding distribution of the first passage time computed numerically is therefore rather noisy. For this reason, this corner is neglected in the computation of the distance Δ.

The introduction of narrow-band excitations has a significant influence on the dynamics so that the analytical results reported in section 1.2 are no longer valid in this case, at least quantitatively. Based on the inspection of several average first passage time maps, a threshold of 4% on Δ is introduced to differentiate between maps showing a good concordance and maps exhibiting visible differences. The RMS distance Δ reaches 9% for the numerical results shown in Fig. 4.10.

As a second step, a statistic approach can also be used to assess if the narrow-band results differ significantly from the analytical results derived for broadband excitations. Based on the Monte Carlo simulations, a confidence interval is defined in which the actual value of the mean first passage time belongs with a probability of at least 95%. If the analytical value is outside this confidence interval, the difference between the broadband and narrow-band results is considered as significant given the number of samples. However, very little is known about the probabilistic distribution of the first passage time. Without damping nor forced excitation, and when the parametric excitation is a δ-correlated noise, the first passage time distribution follows an inverse Gaussian law of mean $4/S_u \ln(H_c/H_0)$ and shape-parameter $2/S_u \ln(H_c/H_0)^2$ [31]. In more general cases, the first passage time shows a more complicated distribution. As an example, Fig. 4.11 shows the histogram of the 20 000 first passage times computed at the point of the map characterized by $H_0^* = -1.6$ and $\Delta H^* = 0.7$ for the excitation and damping conditions of Fig. 4.10. The red curve represents the inverse Gaussian distribution fitted to the numerical data. Although the visual inspection of the experimental distribution suggests that the distribution remains similar to an inverse Gaussian distribution, such a hypothesis is rejected by this Chi-square test (MATLAB function chi2gof). Other goodness-of-fit tests also lead to reject the hypotheses that the first passage time follows a Gamma law or a Weibull law. For the large samples considered here ($n = 20\,000$), these tests are indeed very sensitive and lead to reject the hypothesis even if the experimental distribution only slightly departs from the theoretical one against which the data are tested.

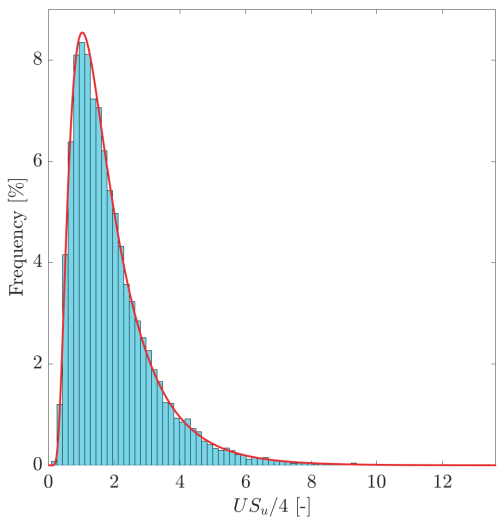

FIGURE 4.11 - Histogram of the reduced first passage time at the point characterized by $H_0^* = -1.6$ and $\Delta H^* = 0.7$ ($n = 20\,000$ samples) and inverse Gaussian distribution fitted to the data (u on $[0.1 f_0 ; 3 f_0]$, w on $[0.8 f_0 ; 1.2 f_0]$, $a = 0$, $S_u = 10^{-3}$, $S_w = 5 \cdot 10^{-4}$).

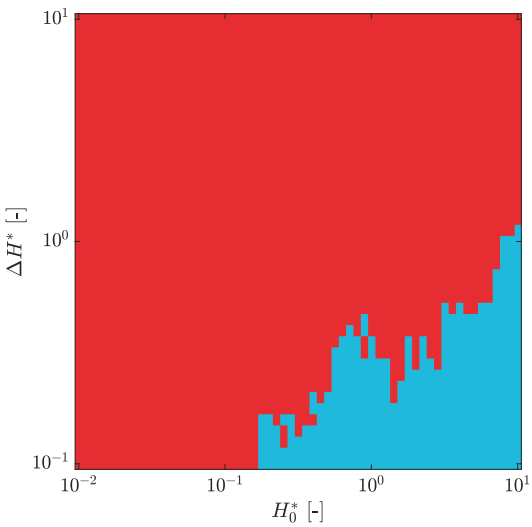

FIGURE 4.12 - Second indicator. Regions are colored in red when the mean first passage time obtained numerically for narrow-band excitations (u on $[0.1 f_0 ; 3 f_0]$ and w on $[0.8 f_0 ; 1.2 f_0]$) differs significantly from the value obtained analytically for broadband excitations ($a = 0$, $S_u = 10^{-3}$, $S_w = 5 \cdot 10^{-4}$).

In the absence of more information about the probabilistic distribution of the first passage time, the Bienaymé-Chebyshev inequality, which is valid whatever the distribution of the parent variable characterized by a finite mean μ and a finite non-zero variance σ^2, can be used to define confidence intervals [4]. This inequality writes

$$P\left[\bar{\mathcal{T}}_n - c\frac{\sigma}{\sqrt{n}} \leqslant \mu \leqslant \bar{\mathcal{T}}_n + c\frac{\sigma}{\sqrt{n}}\right] \geqslant 1 - \frac{1}{c^2} \tag{4.18}$$

and states that $1-1/c^2$ is an underestimation of the probability that the value of the process mean μ lies within the confidence interval centered around the sample mean $\bar{\mathcal{T}}_n$ and of semi-width $c\sigma/\sqrt{n}$, where n is the number of samples. Since σ is unknown, it is estimated with the unbiased estimator

$$S_{n-1}^2 = \frac{1}{n-1}\sum_{i=1}^{n}\left(\mathcal{T}_i - \bar{\mathcal{T}}_n\right)^2. \tag{4.19}$$

It is called an unbiased estimator because the expected value of this estimator equals the variance of the process. Since the number of samples studied is very large, the biased version of the estimator

$$S_n^2 = \frac{n-1}{n}S_{n-1}^2 \tag{4.20}$$

would provide similar results.

In Fig. 4.12, the Bienaymé-Chebyshev inequation (4.18) is used to check if the analytical broadband mean first passage times fall within the confidence intervals derived from the numerical results for narrow-band excitations corresponding to the conditions of Fig. 4.10. Regions colored in red indicate a statistically significant difference between the two sets of results. This figure leads to conclude that the mean first passage time of systems subjected to these narrow-band excitations significantly differs from the values derived analytically for broadband excitations in the whole map except in the bottom right corner where the coefficient of variation of the first passage time is too large to conclude that there exists a significant difference. Note that the same approach applied to the comparison of the analytical and numerical broadband results leads to the conclusion that there is no significant difference between the two sets of results.

The above discussion shows that a more detailed analysis has to be carried out to determine under which conditions (frequency bands of the excitations, damping, force intensities) narrow-band excitations lead to significant differences with respect to the analytical results derived for broadband excitations. In the next section, the influence of the forced excitation frequency band is analyzed. Then, the influence of the parametric excitation frequency band is studied. After that, the influence of the damping factor and the power spectral densities of the parametric and forced excitations is characterized.

4.2.2 Influence of the frequency band of the forced excitation

As a first step, the system is studied for parametric excitations in broadband and several different narrow bands for the forced excitation (including f_0 or not). A first passage time map is drawn for each case. The tools described in the previous section are used to analyze the results.

The three incubation, additive and multiplicative regimes can only be recovered if the frequency band of the forced excitation includes the natural frequency f_0. For instance, when the forced excitation is defined on the frequency interval $[1.2f_0\,;1.6f_0]$, the distance Δ (4.17) between the maps is larger than 200% and the qualitative behavior of the system is totally different. For limited frequency intervals around the natural frequency f_0, a nearly perfect match between the broadband and narrow-band results is observed in the whole map. For instance, Fig. 4.13 shows the map obtained when w is defined on $[0.9f_0\,;1.1f_0]$. The corresponding distance Δ is equal to 3%.

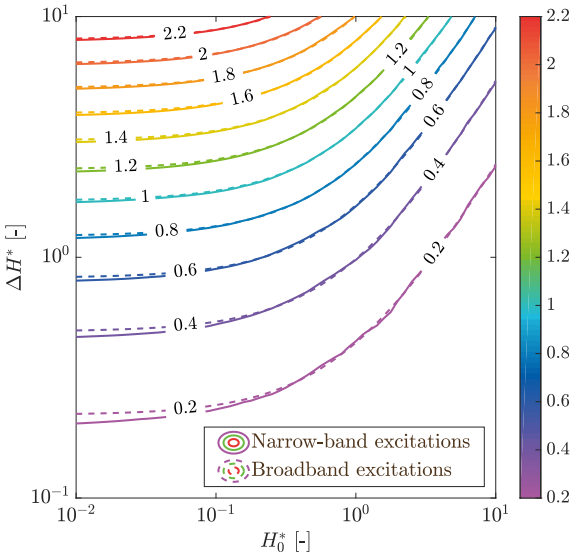

FIGURE 4.13 - Comparison of the reduced average first passage time $U_1 S_u/4$ maps obtained numerically for broadband u and narrow-band w ($[0.9 f_0\,;\,1.1 f_0]$) and analytically for broadband excitations ($a = 0$, $S_u = 10^{-3}$, $S_w = 5 \cdot 10^{-4}$).

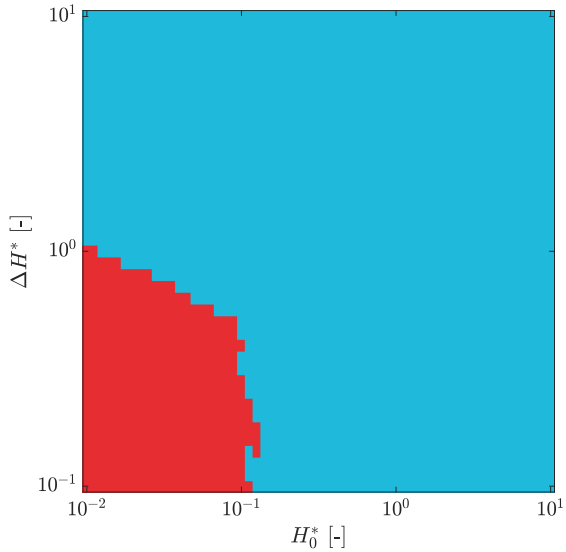

FIGURE 4.14 - Second indicator. Regions are colored in red when the mean first passage time obtained numerically for broadband u and narrow-band w ($[0.9 f_0\,;\,1.1 f_0]$) differs significantly from the value obtained analytically for broadband excitations ($a = 0$, $S_u = 10^{-3}$, $S_w = 5 \cdot 10^{-4}$).

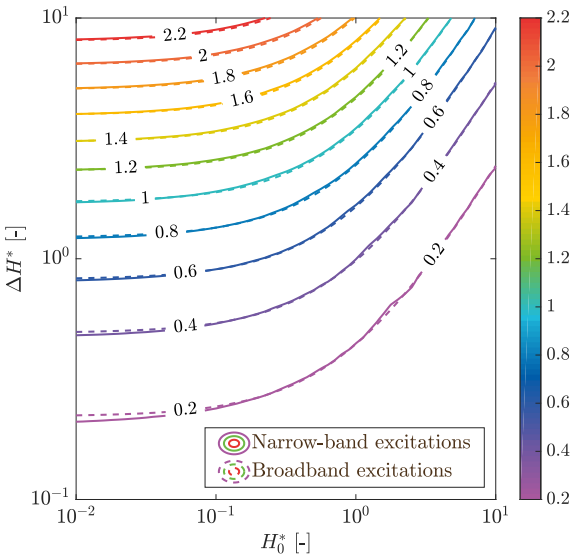

FIGURE 4.15 - Comparison of the reduced average first passage time $U_1 S_u/4$ maps obtained numerically for broadband u and narrow-band w ($[0.8 f_0\,;\,1.2 f_0]$) and analytically for broadband excitations ($a = 0$, $S_u = 10^{-3}$, $S_w = 5 \cdot 10^{-4}$).

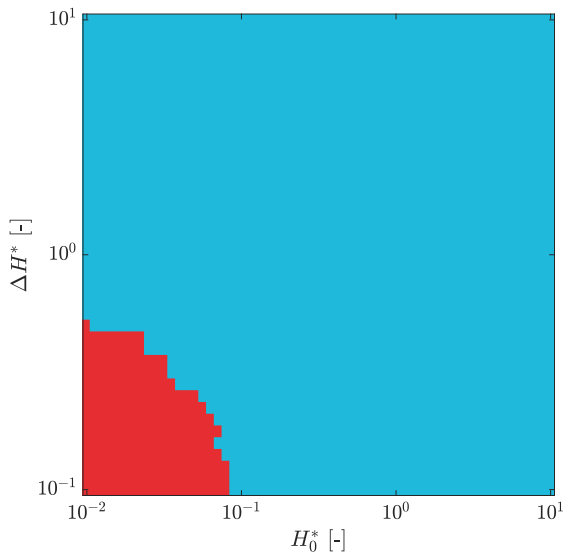

FIGURE 4.16 - Second indicator. Regions are colored in red when the mean first passage time obtained numerically for broadband u and narrow-band w ($[0.8 f_0\,;\,1.2 f_0]$) differs significantly from the value obtained analytically for broadband excitations ($a = 0$, $S_u = 10^{-3}$, $S_w = 5 \cdot 10^{-4}$).

The second indicator is shown in Fig. 4.14. It reveals that the results are significantly different only in the bottom left corner corresponding to small values of H_0^* and ΔH^*. This is not surprising, the bottom left corner corresponds to the limiting case where there is no parametric excitation; the forced excitation has therefore a dominant influence in this zone. The distance indicator Δ decreases when the width of the frequency band around the natural frequency increases. The discrepancies in the bottom left corner of the map also tend to disappear. This is expected since this corresponds to conditions closer to the assumptions used to develop the analytical results. For instance, Figs. 4.15 and 4.16 show the average first passage time map and the second indicator for a forced excitation defined on $[0.8 f_0\,;\,1.2 f_0]$.

In conclusion, in order to recover the general trend of the average first passage time map for broadband excitations, the natural frequency of the oscillator must be included in the frequency band of the forced excitation. When this is the case, results are very close to the analytical results. The narrow band influences only the bottom left corner of the map.

4.2.3 Influence of the frequency band of the parametric excitation

The influence of the frequency band of the parametric excitation appears more complex than for the forced excitation. Increasing the bandwidth does not always have the effect of getting closer to the analytical broadband results. A systematic study is required to characterize the influence of the parametric excitation.

As a first step, the parametric excitation is defined as a narrow-band process of constant power spectral density $S_u = 10^{-3}$ on the frequency interval $[f_1\,;\,f_2]$ and the bounds f_1 and f_2 are varied. For these tests, the forced excitation is defined as a narrow-band process of constant power spectral density $S_w = 5 \cdot 10^{-4}$ on the frequency interval $[0.8 f_0\,;\,1.2 f_0]$, in agreement with the conclusions of the previous section. Because of its large computation cost (the full map of first passage time must be computed, which requires about 20 000 samples), the distance Δ is inappropriate to carry out a systematic sensitivity study with two or more parameters. A simplified indicator I is therefore introduced and defined as

$$I = \left| \frac{U_1^{\mathrm{NB}} - U_1^{\mathrm{BB}}}{U_1^{\mathrm{BB}}} \right|, \tag{4.21}$$

where U_1^{NB} and U_1^{BB} are respectively the mean first passage time obtained from Monte Carlo simulations with narrow-band processes at one single point of the map and the corresponding analytical value for broadband processes. Based on the conclusions of the previous section, the observation point is chosen far from the bottom left corner where the influence of the limited bandwidth of the forced excitation is large and for moderate values of H_0^* and ΔH^* to limit the computation time.

Fig. 4.17(a) shows the value of I (4.21) as a function of the lower and upper frequencies f_1 and f_2 (normalized by the natural frequency f_0) that define the parametric excitation at the point of the map characterized by $H_0^* = 10^{-1.5}$ and $\Delta H^* = 10^0$. The results are similar when other observation points are used.

This figure shows that it is necessary to include the second harmonic of the natural frequency, $2 f_0$, in the frequency interval to be close enough to the analytical results for broadband excitations. In fact, when the second harmonic of the natural frequency does not belong to the frequency interval of the parametric excitation, the first passage time map looks completely different; even the three regimes identified in section 1.2 do not appear. By contrast, it is not necessary to include the natural frequency itself in the frequency interval $[f_1\,;\,f_2]$. This can be supported by the deterministic theory of Mathieu equation. As shown in section 1.1, instabilities occur at frequencies $2 f_0/k$ (k integer). While the instability for $k = 1$, *i.e.* at $f = 2 f_0$, is the most critical, the other instabilities do not develop when forced excitation or damping is introduced in the system unless the amplitude of the parametric excitation is large.

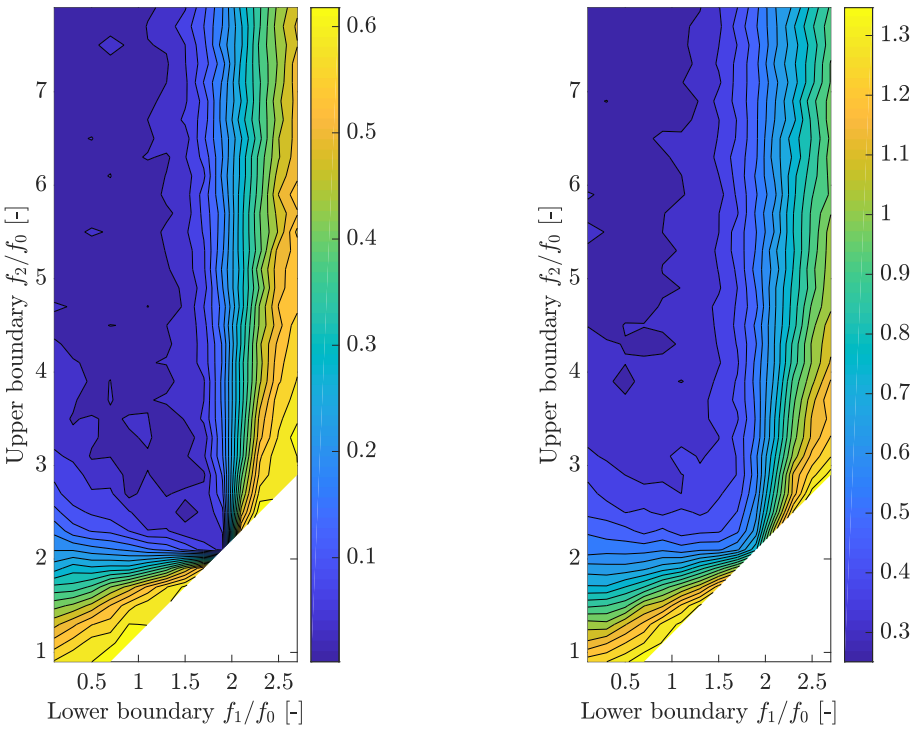

(a) $S_w = 5 \cdot 10^{-4}$ and $S_u = 10^{-3}$.

(b) $S_w = 5 \cdot 10^{-2}$ and $S_u = 10^{-1}$.

FIGURE 4.17 - Indicator I (4.21) at point $H_0^* = 10^{-1.5}$ and $\Delta H^* = 10^0$ as a function of the lower and upper bounds of the frequency band of the parametric excitation.

If the same Fig. 4.17(a) is plotted for different amplitudes of the parametric excitation, *i.e.* different values of its constant power spectral density (see for instance Fig. 4.17(b) for $S_u = 10^{-1}$ and $S_w = 5 \cdot 10^{-2}$), it is observed that the value of the indicator varies. Even if the general shape of the figure is not strongly modified when the magnitude of the parametric excitation increases, the value of the indicator increases. In other words, a larger frequency interval for u is required to get the same value of the indicator. A detailed study of the influence of the other parameters of the problem, the power spectral densities S_u and S_w of the excitations and the damping factor a is therefore required. This study is performed in the next section.

4.2.4 Damping and power spectral densities influence

In this section, the influence of the damping factor a and the constant values of the power spectral densities S_w and S_u of the forced and parametric excitations is studied. Based on the results of the previous sections, it seems acceptable to define the forced excitation on the frequency interval $[0.8 f_0 ; 1.2 f_0]$ and the parametric excitation on the frequency interval $[f_0 ; 4 f_0]$. The same indicator is computed at the same point of the map ($H_0^* = 10^{-1.5}$ and $\Delta H^* = 10^0$) by systematically varying a between 0 and 4, S_u between 10^{-3} and 10^{-1} and S_w between 10^{-6} and 10^{-1}. The results are plotted in Fig. 4.18.

Fig. 4.18(a) shows the indicator I (4.21) as a function of the power spectral densities of the forced and parametric excitations for a damping factor $a = 1.6$. At fixed a, the value of I seems independent of the power spectral density of the forced excitation, S_w. By contrast, the power spectral density of the parametric excitation, S_u, influences the value of indicator I. The higher the power spectral density of the parametric excitation S_u, the larger the difference between the narrow-band and broadband results.

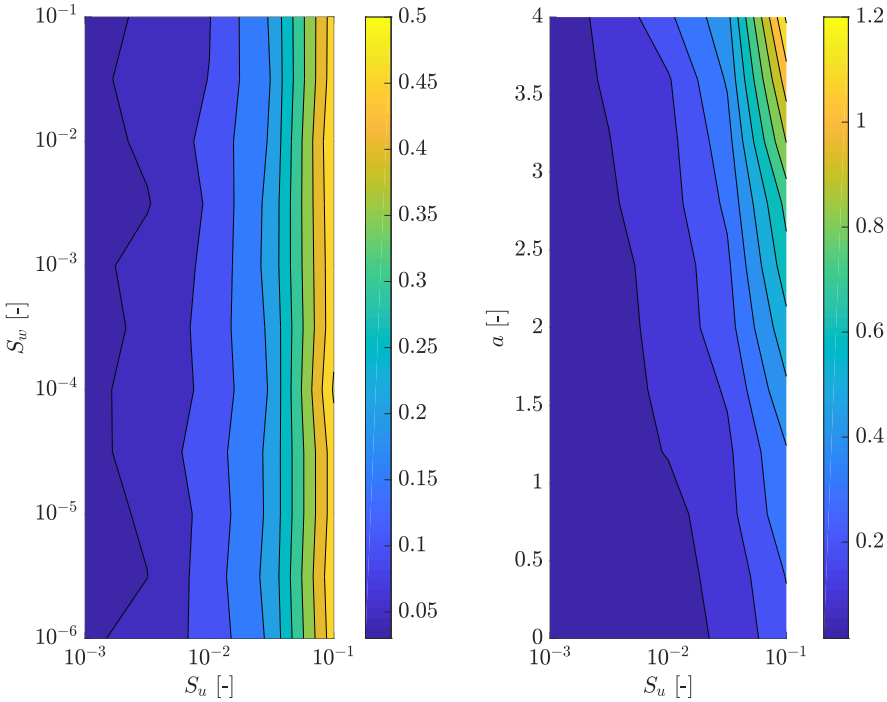

(a) $a = 1.6$.

(b) $S_w = 10^{-2}$.

FIGURE 4.18 - Indicator I (4.21) at point $H_0^* = 10^{-1.5}$ and $\Delta H^* = 10^0$ as a function of the parameters of the problem a, S_u and S_w.

Fig. 4.19 shows a cross-section of Fig. 4.18(a) at a constant value of S_w and allows to describe the evolution of indicator I with S_u. The indicator I grows linearly for large values of S_u (larger than 0.02) but scales as a logarithm for smaller values of S_u. It is not really surprising that S_u directly influences the first passage time, as it is also the case for broadband excitations. As detailed in section 1.2 (Equation 1.53), the first passage depends on the reduced parameters H_0^* and ΔH^*, in which only the ratio S_u/S_w appears, but also explicitly on the power spectral density S_u.

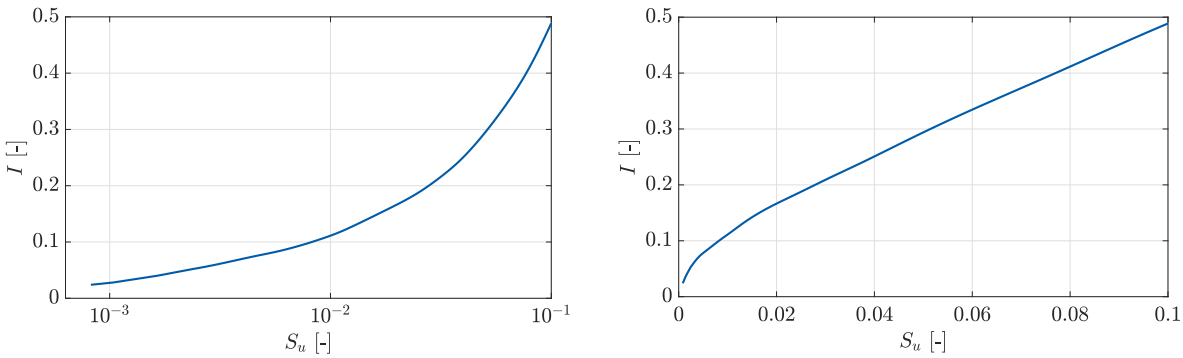

(a) S_u in logarithmic scale.

(b) S_u in linear scale.

FIGURE 4.19 - Indicator I (4.21) as a function of S_u for $S_w = 10^{-2}$ and $a = 1.6$.

Fig. 4.18(b) shows the influence of a and S_u on I for S_w fixed to 10^{-2}. It is observed that results from narrow-band Monte Carlo simulations depart from the broadband ones when a and/or S_u is increased. Curves of iso-I appear as parallel lines (with the a-axis in linear scale and the S_u-axis in logarithmic scale).

Before concluding, it should be noted that, even if this study is based on a single point of the map ($H_0^* = 10^{-1.5}$ and $\Delta H^* = 10^0$) located in the additive regime, the same exercise has been performed at other points located in other regimes. The study of the evolution of the indicator I with parameters S_w, S_u and a at different points located in the three regimes shows that the general behavior of I is recovered and that the conclusions drawn in the additive regime are valid in the whole map.

4.3 Numerical study of first passage time conclusions

This chapter constitutes the last step before the experimental validation of the first passage time theory described in the next part of the work. This part aims particularly at preparing the experimental tests and has allowed to highlight some new results related to first passage time of systems subjected to narrow-band excitations.

As a first step, the multi-degree-of-freedom equations of motion have been reduced to a set of decoupled single-degree-of-freedom equations of motion. An efficient use of the reduced model can be done when the forced and parametric excitations are defined on a limited narrow band in the frequency domain, and when the parametric excitation amplitude is not too high.

Because the available analytical results are only valid for broadband excitations, a numerical study has been conducted to characterize the influence of narrow-band excitations on the first passage time map. The global behavior is recovered when the frequency bands of the forced and parametric excitations include respectively the natural frequency of the oscillator and its second harmonic. A small shift can however be observed between the broadband and narrow-band results when the bandwidths of the excitations decrease and when the intensity of the parametric excitation or the damping factor increase.

All these important conclusions will be taken into account and will help to define the right forces to apply on the experimental set-up in the next part.

PART 5

EXPERIMENTAL STUDY OF FIRST PASSAGE TIME

This part of the work is dedicated to the experimental study of first passage time. The numerical study performed in the previous part will help to prepare the experimental part. The first section is devoted to the physical limitations that constrain the experimental validation of the theory. Then, the second section focuses on the experimental study of the one-degree-of-freedom Mathieu equation. Eventually, the third section draws some experimental conclusions in the case of the multi-degree-of-freedom Mathieu equation.

5.1 Experimental limitations

In the previous part, it was supposed that the parameters S_u, S_w and a could take any value. The first passage time maps corresponding to narrow-band excitations were built for ranges of variation of these parameters that allow to highlight the three additive, multiplicative and incubation regimes. In practice, S_u, S_w and a are linked to physical parameters and their values are therefore constrained. In this section, the dimensionless parameters of the single-degree-of-freedom system are first related to the physical dimensional parameters of the problem. Then, the practical experimental limitations on these parameters are listed. The mode used for the model reduction is also selected and this choice is justified.

5.1.1 Nondimensionalization

As a result of the reduction of the N-degree-of-freedom system into N single-degree-of-freedom systems, the dynamic behavior of the system is governed by N equations that take the general form

$$m_{\text{eq}}\ddot{z}(t) + c_{\text{eq}}\dot{z}(t) + [k_{\text{eq}} + F_u(t)k_{\text{p,eq}}]z(t) = p(t), \tag{5.1}$$

where m_{eq}, c_{eq}, k_{eq} and $k_{\text{p,eq}}$ are equivalent parameters defined in section 4.1, $F_u(t)$ is the parametric excitation applied to the multi-degree-of-freedom system, $p(t)$ is the projection of the forced excitation on the mode under consideration and $z(t)$ is the modal coordinate corresponding to the mode studied. In order to compare the results with the analytical expressions introduced in part 1, this equation needs to be rewritten in a dimensionless form. A characteristic time is defined as

$$T_{\text{charact}} = \sqrt{\frac{m_{\text{eq}}}{k_{\text{eq}}}} \tag{5.2}$$

and the dimensionless time

$$\tau = \frac{t}{T_{\text{charact}}} \tag{5.3}$$

is introduced so that the derivative of z with respect to the dimensional time t, $\dot{z}$, can be rewritten in terms of the derivative of z with respect to the dimensionless time τ, z', as

$$\dot{z} = \frac{z'}{T_{\text{charact}}}. \tag{5.4}$$

Mathieu equation (5.1) can then be rewritten as

$$z''(\tau) + \frac{c_{\text{eq}}}{k_{\text{eq}} T_{\text{charact}}} z'(\tau) + \left[1 + F_u(\tau)\frac{k_{\text{p,eq}}}{k_{\text{eq}}}\right] z(\tau) = \frac{p(\tau)}{k_{\text{eq}}}. \tag{5.5}$$

This equation is equivalent to the single-degree-of-freedom dimensionless Mathieu equation for the modal coordinate $z(\tau)$

$$z''(\tau) + 2\xi z'(\tau) + [1 + u(\tau)]z(\tau) = w(\tau) \tag{5.6}$$

if the damping coefficient ξ is related to the physical parameters of the problem by

$$\xi = \frac{c_{\text{eq}}}{2k_{\text{eq}} T_{\text{charact}}} \tag{5.7}$$

and the forced and parametric excitations $w(\tau)$ and $u(\tau)$ are respectively defined by

$$w(\tau) = \frac{p(\tau)}{k_{\text{eq}}} = \alpha \frac{F_w(\tau)}{k_{\text{eq}}} \quad \text{and} \quad u(\tau) = \frac{F_u(\tau) k_{\text{p,eq}}}{k_{\text{eq}}}, \tag{5.8}$$

where α is given by (4.13). From the definition of the power spectral density (A.3), the power spectral density of a signal βy as a function of the dimensionless frequency f/f^* is related to the power spectral density of the signal y function of the frequency f by

$$S_{\beta y}(f/f^*) = \beta^2 f^* S_y(f). \tag{5.9}$$

The constant power spectral densities of $F_w(t)$ and $F_u(t)$ (denoted $\tilde{S}_w(f)$ and $\tilde{S}_u(f)$ and functions of the dimensional frequency f) are therefore related to the power spectral densities $S_w(fT_{\text{charact}})$ and $S_u(fT_{\text{charact}})$ (functions of the dimensionless frequency fT_{charact}) of $w(\tau)$ and $u(\tau)$ by

$$S_w = \frac{\tilde{S}_w}{T_{\text{charact}}} \left(\frac{\alpha}{k_{\text{eq}}}\right)^2 \quad \text{and} \quad S_u = \frac{\tilde{S}_u}{T_{\text{charact}}} \left(\frac{k_{\text{p,eq}}}{k_{\text{eq}}}\right)^2. \tag{5.10}$$

Accordingly, (5.1) and (5.6) provide the same solution z if the dimensional and dimensionless times are related by (5.3), the damping coefficients by (5.7) and the power spectral densities of the excitations by (5.10).

5.1.2 Constraints on the parameters

This section aims at listing the practical limitations on the parameters for the experimental validation of the first passage time theory described in section 1.2. As illustrated in section 4.1.1, a set of equivalent parameters is associated to each mode. Those are linked to the geometrical and physical parameters of the structure and cannot be changed without redesigning a new experimental set-up. The equivalent parameters of several bending modes have however been identified and the choice of the mode remains free. The limitations detailed in this section restrain, on the one hand, the choice of the bending mode studied and, on the other hand, the definition of the excitation applied to the structure.

As shown in section 4.2, at least 20 000 samples are required to obtain a smooth average first passage time map using numerical simulations. The same constraint applies to the experimental tests. In order to observe experimentally reduced first passage times

$$\frac{1}{4} U S_u = \frac{1}{4} \frac{\tilde{U}}{T_{\text{charact}}} \frac{\tilde{S}_u}{T_{\text{charact}}} \left(\frac{k_{\text{p,eq}}}{k_{\text{eq}}}\right)^2 = \frac{\tilde{U}\tilde{S}_u}{4} \left(\frac{k_{\text{p,eq}}}{k_{\text{eq}} T_{\text{charact}}}\right)^2 \tag{5.11}$$

in a reasonable dimensional time $\tilde{U}$, the coefficient $\tilde{S}_u \left(k_{\mathrm{p,eq}}/\left[k_{\mathrm{eq}}T_{\mathrm{charact}}\right]\right)^2$ has to be as large as possible. This has an influence on the choice of the mode, since bending modes characterized by a large value of the ratio $k_{\mathrm{p,eq}}/\left[k_{\mathrm{eq}}T_{\mathrm{charact}}\right]$ are therefore to be preferred. To achieve this objective, the parametric excitation power spectral density $\tilde{S}_u$ should also be as high as possible.

As shown in section 1.2.4, when a is larger than 2, the iso-time curves in the multiplicative regime are characterized by a negative slope equal to $2-a$ (in the case of broadband excitations). The higher the damping factor a, the higher the slope (in absolute value) and the more difficult the identification of the multiplicative regime since the part of the multiplicative regime reachable in a reasonable amount of time reduces to the bottom right corner that is characterized by the highest coefficient of variation (section 1.2.2). According to (5.7) and (5.10), the dimensionless coefficient a is related to the dimensional parameters of the problem by

$$a = \frac{8\xi}{S_u} = 4\frac{c_{\mathrm{eq}}k_{\mathrm{eq}}}{k_{\mathrm{p,eq}}^2\tilde{S}_u}. \tag{5.12}$$

In order to minimize a, the ratio $c_{\mathrm{eq}}k_{\mathrm{eq}}/k_{\mathrm{p,eq}}^2$ should be minimized and high values of $\tilde{S}_u$ must be applied.

The above considerations form a set of guidelines for the model reduction. Given the equivalent parameters of the first six bending modes of the structure identified in section 4.1, they provide the ultimate justification supporting the selection of the second bending mode, as already implemented in section 4.1. The equivalent parameters of the second bending mode are given by

$$T_{\mathrm{charact}} = 4\cdot 10^{-3}\ \mathrm{s}, \qquad k_{\mathrm{p,eq}} = 39\ \mathrm{m}^{-1}, \qquad k_{\mathrm{eq}} = 3273\ \mathrm{Nm}^{-1}, \tag{5.13}$$

$$c_{\mathrm{eq}} = 0.08\ \mathrm{N[m/s]}^{-1}, \qquad \text{and} \qquad m_{\mathrm{eq}} = 0.05\ \mathrm{kg}.$$

The dimensionless parameter $\xi = 4\cdot 10^{-3}$ is therefore much smaller than one, as required by the theory to have a quasi-Hamiltonian system.

Regarding the definition of the excitations applied to the structure, other conditions have to be met by F_u and F_w. From a practical point of view, combinations of the power spectral densities and frequency bands have to give rise to maximal amplitudes less than 9 N for the parametric and forced excitations. This corresponds to the limitation of the shakers mounted on the structure (section 2.3). In any case, given the lightness of the structure, it is not safe to apply larger forces. One must also keep in mind that the dimensionless parameters S_u and S_w have to remain significantly less than 1 (in practice, less than 0.1) so that the system remains quasi-Hamiltonian.

All these constraints on the parameters hold for the remaining of the chapter. In the following sections, other conditions will be added to address different specific cases and will be detailed when required. Section 5.2 is devoted to the study of the experimental one-degree-of-freedom Mathieu equation. It focuses on both the linear case and the nonlinear one. In section 5.3, a brief study of the multi-degree-of-freedom Mathieu equation is performed.

5.2 Single-degree-of-freedom system first passage time

This section focuses on the one-degree-of-freedom Mathieu equation and the experimental study of its first passage time. The first paragraph briefly lists the conditions on the excitations that are valid in the whole section, *i.e.* those that ensure that the assumption of a single-degree-of-freedom system is verified. Then, the linear equation is studied. Eventually, the amplitudes of the forces are increased to excite the nonlinearities of the structure.

5.2.1 Constraints on the excitations

Some constraints on the excitations have to be added with respect to those described in section 5.1.2. First, because this section is devoted to the study of the single-degree-of-freedom Mathieu equation, the conditions under which the model reduction is valid must be met. These conditions are detailed in section 4.1. In practice, F_w has to be defined on a frequency band centered on the natural frequency f_0 selected for the model reduction and sufficiently narrow. F_u must not be too high in amplitude and the second harmonic of the other bending modes should not be included in its frequency band. Then, it was shown numerically in section 4.2 that first passage time maps similar to the analytical broadband ones can be obtained with narrow-band excitations provided that the frequency intervals of definition of F_w and F_u include respectively the natural frequency f_0 (condition similar to the condition for the validity of the model reduction) and its second harmonic $2f_0$.

5.2.2 Linear Mathieu equation

In order to avoid exciting the nonlinearities of the structure, the forced and parametric excitations should be kept as small as possible. Based on all the conditions pertaining to the forced and parametric excitations, they are defined as follows. The forced excitation is defined as a narrow-band process of constant power spectral density $\tilde{S}_w = 5 \cdot 10^{-3}$ N^2/Hz on the frequency interval $[0.87 f_0 ; 1.13 f_0] = [34 ; 44]$ Hz. This frequency interval covers the natural frequency of the second bending mode but does not cover any of the other natural frequencies of the strip. The parametric excitation is defined as a narrow-band process of constant power spectral density $\tilde{S}_u = 5 \cdot 10^{-3}$ N^2/Hz on the frequency interval $[0.77 f_0 ; 2.57 f_0] = [30 ; 100]$ Hz. This frequency interval covers the natural frequency f_0 and its second harmonic. It can be objected that the second harmonic of the first bending mode and the natural frequency of the third bending mode are also included. This is not an issue thanks to the high damping ratios of these two modes (Table 3.10). Dimensionless parameters a, S_w and S_u are obtained with (5.10) and (5.12) and given by

$$a = 132, \qquad S_w = 2.5 \cdot 10^{-10} \qquad \text{and} \qquad S_u = 1.8 \cdot 10^{-4}. \tag{5.14}$$

As required by the theory to have a quasi-Hamiltonian system, S_u and S_w are much smaller than one. The assumption of a quasi-Hamiltonian system is also checked further by analyzing the measured Hamiltonian. The high value of a does not mean that damping is high in absolute figures ($\xi = 4 \cdot 10^{-3} \ll 1$) but, merely, that damping is high with respect to the parametric excitation intensity.

The approach followed numerically cannot be chosen to build the experimental first passage time map because it is not possible to compute the Hamiltonian at each time of acquisition and to stop the acquisition when a given Hamiltonian is reached. Another approach, that is based on a single time-recording of the structure response, is therefore followed. This approach is described in the next paragraphs.

First, data acquisition is performed in the lab on the real structure. The reader is referred to section 2.3 for more details about the measurement chain. The structure is excited by the horizontal and vertical shakers for 30 minutes and the response of the structure is measured at point P3 with the laser transducer. The point P3 (Fig. 3.4) corresponds to an antinode of vibration of the second bending mode (Fig. 3.22(b)). It has been selected according to section 4.1.1 to limit the influence of the other bending modes.

Data acquisition and signal processing are carried out using the LMS Test.Lab software and the LMS SCADAS Lab acquisition system. For the study of first passage time and the recording of time signals, the tool Multi-axis Random Control of the module Test.Lab Environmental is chosen. This tool is presented in LMS documentation as a solution for advanced vibration testing and closed-loop multi-shaker control [43]. The system implements a reliable, fast and accurate control algorithm. In the current case, this module is particularly well suited since the objective is to apply forced and parametric excitations that are characterized by a power spectral density as close as possible to a constant in a given frequency band. The

tool Multi-axis Random Control allows to define and control a random excitation that matches a predefined power spectral density profile. Power spectral densities of the parametric and forced excitations measured experimentally on the structure are plotted in Fig. 5.1 with the target power spectral densities defined as references (dotted lines).

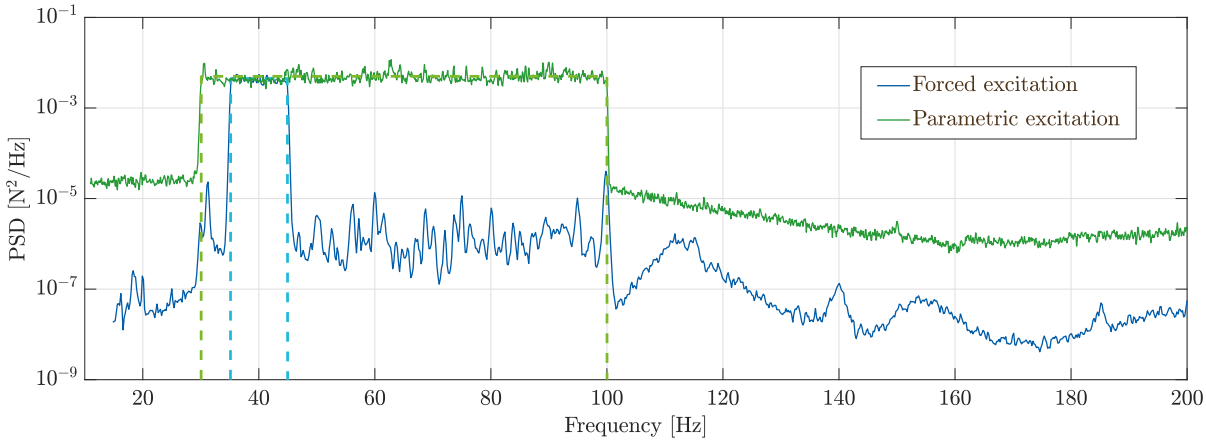

FIGURE 5.1 - Power spectral densities of the forced and parametric excitations measured experimentally (solid lines) and reference power spectral densities (dotted lines).

Fig. 5.2 shows a part of the time series of the velocity $\dot{x}$ measured at point P3. Its power spectral density is represented in Fig. 5.3 and shows that the peak at the natural frequency dominates the other peaks. This confirms that the structure responds quasi exclusively in the second bending mode at point P3. The forced and parametric excitations applied to the structure therefore allow to meet this necessary condition required for the model reduction to be valid.

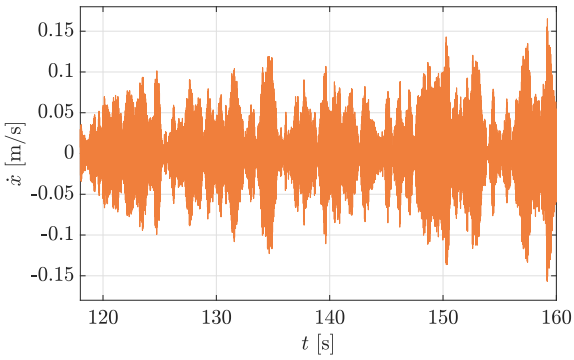

FIGURE 5.2 - Fragment of the time evolution of the velocity measured at point P3.

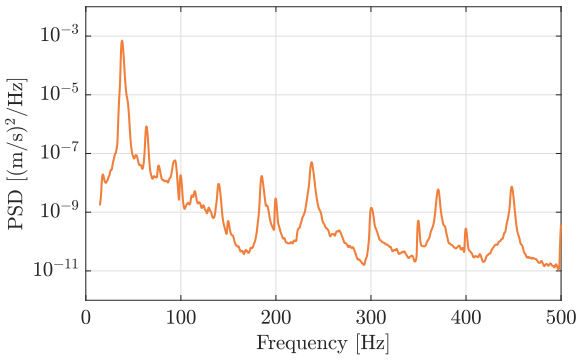

FIGURE 5.3 - Power spectral density of the velocity measured at point P3.

The response of the structure measured at point P3 in terms of velocity $\dot{x}(t)$ is then numerically integrated to compute the evolution with time of the position of point P3. Since the structure responds only in the second bending mode, the position $x(t)$ is directly related to the modal coordinate $z(\tau)$ of (5.6) and the dimensionless Hamiltonian corresponding to this equation is computed as

$$H = \frac{z^2}{2} + \frac{[z']^2}{2} = \frac{z^2}{2} + \frac{[\dot{z}T_{\text{charact}}]^2}{2}. \tag{5.15}$$

A fragment of the time evolution of the Hamiltonian is plotted in Fig. 5.4. The condition of a quasi-Hamiltonian system can be verified graphically by representing the response of the structure in the phase plane $(x, \dot{x})$. Fig. 5.5 shows three segments of the trajectory of the system. They appear to be nearly tangent to the ellipses of constant energy so that the Hamiltonian varies only by a small quantity over one period of revolution of the unperturbed dynamical system.

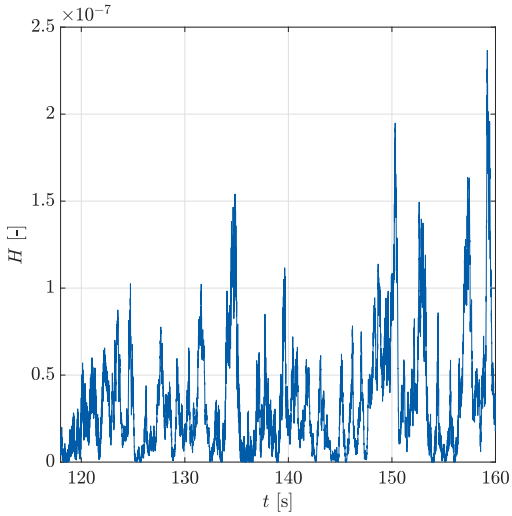

FIGURE 5.4 - Fragment of the time evolution of the Hamiltonian H.

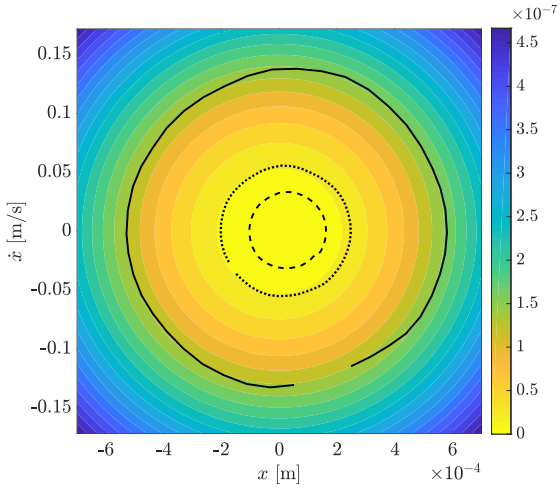

FIGURE 5.5 - Three fragments of the measured experimental trajectory of the system in the phase plane and contours of the Hamiltonian H.

The average first passage time map corresponding to the evolution of the Hamiltonian of the system with time can then be built. If the time signal is sufficiently long, the same level of energy is reached several times and the system passes many times from initial energies H_0 to higher energies $H_c = H_0 + \Delta H$. Both energy axes are discretized in a finite number of values. The intervals between these values are chosen with uniform sizes on a logarithmic scale as this is the physical scaling suggested by the stochastic model. The mean first passage time corresponding to each point of the map (*i.e.* each combination of initial energy H_0 and energy increment ΔH) is obtained by averaging all the first passage times corresponding to the transitions between these levels of energy. The map obtained is represented in solid lines in Fig. 5.6. The main drawback of this method is that it provides an average map that does not show the same quality everywhere because the number of samples used in the averaging is not the same in the whole space $(H_0^*, \Delta H^*)$. Indeed, for a given H_0^*, points of the map characterized by small ΔH^* are described by a larger number of experimental data than the points with large ΔH^* as the system needs to go through lower energy levels before reaching any higher energy level.

Fig. 5.6(a) compares the experimental results with the analytical average first passage time map obtained under the assumption of broadband excitations. The results are qualitatively similar and the general trend of the average first passage time is recovered experimentally. In spite of the very small value of S_u, the damping factor a is large and a shift between the curves is observed, in agreement with the conclusions drawn in section 4.2.

Fig. 5.6(b) compares the experimental results with the map obtained using Monte Carlo simulations of the numerical system subjected to narrow-band excitations. Globally, a good quantitative match between the two maps is observed and the global behavior of the mean first passage time is recovered. The different regimes can be analyzed separately.

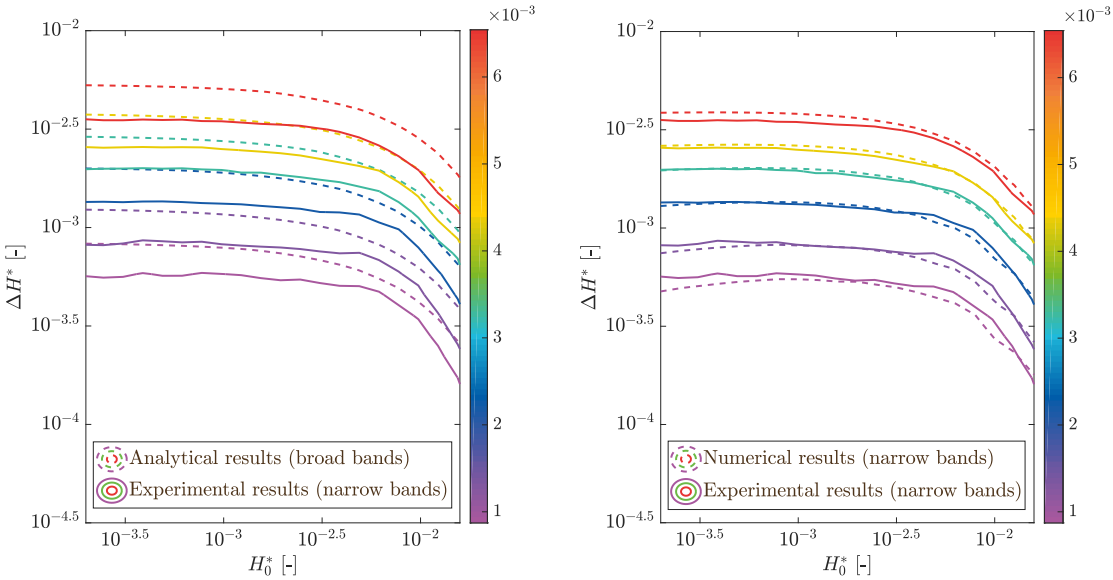

(a) (b)

FIGURE 5.6 - Reduced average first passage time $U_1 S_u/4$ as a function of H_0^* and ΔH^*. Comparison of the maps obtained experimentally and numerically for narrow-band excitations (F_u on $[0.77\,f_0\,;\,2.57\,f_0]$, F_w on $[0.87\,f_0\,;\,1.13\,f_0]$) and analytically for broadband excitations ($a = 132$, $S_w = 2.5 \cdot 10^{-10}$, $S_u = 1.8 \cdot 10^{-4}$).

The additive regime is well represented. In the left part of Fig. 5.6(b), the experimental curves tend towards horizontal asymptotes, at least for sufficiently large values of the increment ΔH^*. The incubation regime can be highlighted by considering cross-sections of the map at constant values of H_0^*. Fig. 5.7(a) shows the evolution of the average first passage time as a function of ΔH^* for $H_0^* = 2 \cdot 10^{-2}$ and $2 \cdot 10^{-3}$. Crosses represent the average first passage time extracted from the experimental data. Dotted lines are obtained by linear regression of the experimental data. The coefficients of determination are higher than 0.99 and the linear trend characteristic of the incubation regime is well recovered. Fig. 5.7(b) demonstrates that the incubation regime is however limited to small values of ΔH^*. The linear behavior is lost outside the incubation regime for larger values of ΔH^*.

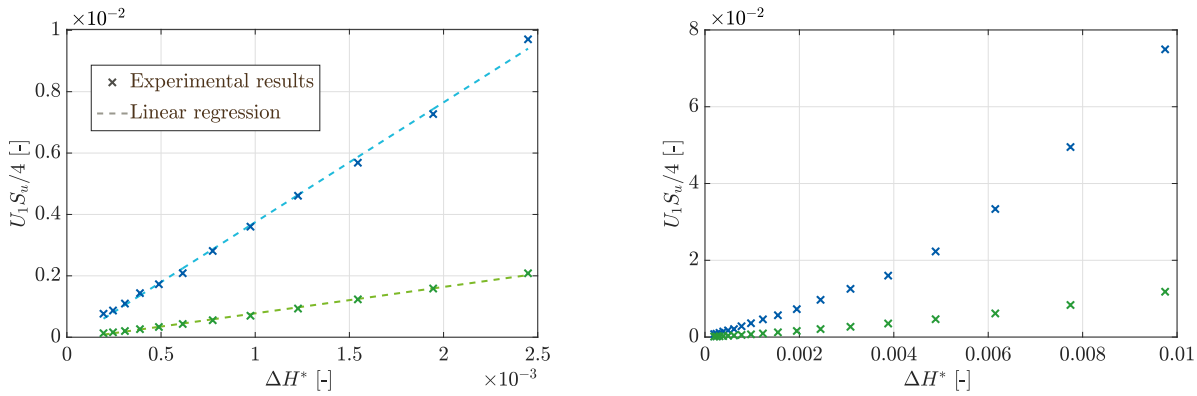

(a) (b)

FIGURE 5.7 - Cross-sections of the average first passage time map (Fig. 5.6(b)) for $H_0^* = 2 \cdot 10^{-2}$ (in blue) and $H_0^* = 2 \cdot 10^{-3}$ (in green).

The multiplicative regime cannot be rigorously observed in Fig. 5.6(b). In the right part of the figure, the curves show the same negative slope but the multiplicative regime is not yet reached since the highest value of H_0^* is of the order of $10^{-1.5}$ while the multiplicative regime appears for $H_0^* \gg 1$. On the one hand, larger values of H_0^* must be avoided here since this can trigger the nonlinearities in the system. On the other hand, it was shown in section 1.2.4 that, for damped systems subjected to broadband excitations, the asymptotic slope in the multiplicative regime equals $2-a$. This result is certainly not directly valid in the narrow-band excitations case but suggests that, given the high value of $a = 132$, the part of the multiplicative region reachable in a limited amount of time reduces to the bottom right corner. Because this corner is characterized by high coefficients of variation, very long time signals are required to get a smooth map in this region.

The differences between the numerical and experimental results can be ascribed to different factors. First, the experimental conditions never match exactly the numerical ones. For instance, the power spectral densities of the excitations are not perfectly constant on the frequency band of definition, and do not drop to zero outside this interval (Fig. 5.1). Then, the structure is inherently a multi-degree-of-freedom system and it is not possible to excite a single mode of the structure. Even if Fig. 5.3 shows that the structure responds mainly in its second bending mode at point P3, the other modes also slightly contribute to the response of the structure, which limits the validity of the reduced model. Modeling errors are also inherent to the process. Therefore, the response at point P3 is not exactly described with the linear Mathieu equation (4.11) with the equivalent parameters identified in section 4.1. Structure nonlinearities can also be a source of differences between the numerical and experimental results. Even if the intensities of the excitations have been chosen extremely small to limit the excitation of the nonlinearities, those are inherent to the structure. When the system is excited, the Hamiltonian increases and can reach high values (corresponding to high displacements and/or high velocities) so that the strip enters the nonlinear regime, even for small excitations. Finally, it can be noted that the experimental curves could be smoothed by increasing the length of observation. Here, the different points of the map are obtained by averaging between 4000 and 17 000 experimental samples. Increasing the number of samples would increase the quality of the map.

The requirement to include the second harmonic of the natural frequency in the frequency band of the parametric excitation has been introduced in section 4.2.3 based on numerical simulations but can also be illustrated experimentally. The forced excitation is defined as a narrow-band process of constant power spectral density $\tilde{S}_w = 4 \cdot 10^{-3}$ N^2/Hz on the frequency interval $[0.87 f_0\,;\, 1.13 f_0] = [34\,;\,44]$ Hz. This frequency interval does not cover any of the other natural frequencies of the strip. The parametric excitation is defined as a narrow-band process of constant power spectral density $\tilde{S}_u = 6 \cdot 10^{-3}$ N^2/Hz on the frequency interval $[0.76 f_0\,;\, 1.27 f_0] = [30\,;\,50]$ Hz. This frequency interval covers the natural frequency f_0 but not its second harmonic. Fig. 5.8 compares the average first passage time map obtained experimentally with the analytical results obtained under the assumption of broadband processes. As already mentioned in section 4.2, the results are totally different when the second harmonic is not included. In Fig. 5.8, none of the three theoretical regimes can be identified.

In conclusion, the excitation of the designed experimental set-up with the right forced and parametric excitations allows to observe the incubation and the additive regimes. In order to observe rigorously the multiplicative regime, the coefficient a should be decreased. The damping factor a is related to the other dimensional parameters of the problem by (5.12). In order to ensure the validity of the multi-degree-of-freedom system reduction and that the nonlinearities are not excited, $\tilde{S}_u$ should not be increased. The structure has therefore to be redesigned. The equivalent parameters k_{eq}, and therefore a, could be decreased by decreasing the initial pre-stress (see the definition of the equivalent parameters in section 4.1.1). Another way of decreasing a is to decrease the length of the strip. It is indeed checked numerically that this modification has the effect of decreasing the ratio $k_{\text{eq}}/k_{\text{p,eq}}^2$.

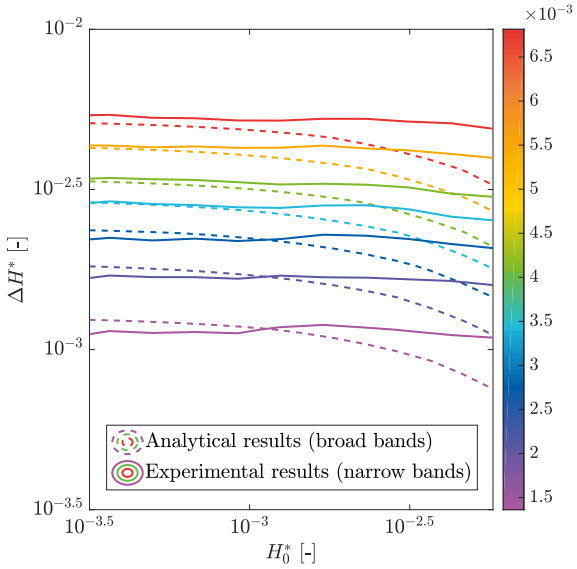

FIGURE 5.8 - Reduced average first passage time $U_1 S_u/4$ as a function of H_0^* and ΔH^*. Comparison of the maps obtained experimentally for narrow-band excitations (F_u on $[0.77 f_0\,; 1.27 f_0]$, F_w on $[0.87 f_0\,; 1.13 f_0]$) and analytically for broadband excitations ($a = 108$, $S_w = 2.5 \cdot 10^{-10}$, $S_u = 2.2 \cdot 10^{-4}$).

5.2.3 Nonlinear Mathieu equation

The same exercise can be carried out with a larger excitation triggering some nonlinearities of the structure. In this section, the structure is subjected to forced and parametric excitations defined on the same frequency bands as in Fig. 5.6 but the power spectral densities are increased by one order of magnitude. The Hamiltonian is still computed by (5.15) where T_{charact} is linked to the natural frequency identified at low level when the system behaves linearly. Note that this is an approximation of the actual energy since the functional dependency of the energy is modified by nonlinearities. This approach to compute the energy is suggested in [20].

The experimental average first passage time map obtained is represented in Fig. 5.9 and compared with the numerical map corresponding to the equivalent dimensionless parameters that characterize the experimental test, *i.e.*

$$a = 29, \qquad S_w = 3 \cdot 10^{-9} \qquad \text{and} \qquad S_u = 8 \cdot 10^{-4}. \tag{5.16}$$

This figure shows that the main characteristics of the average first passage time map can still be observed, but the experimental curves are shifted with respect to the curves obtained with the linear numerical model. The additive regime is observed for small H_0^*. When H_0^* increases, the curves go down with similar negative slopes. The slope has decreased in absolute value with respect to the previous linear case (Fig. 5.6) as the coefficient a is smaller. Fig. 5.10 shows cross-sections of the map for constant values of the initial energy level. For small energy increments, a more or less linear behavior is observed. This linear behavior in the incubation regime is however not as strong as in the reference case (coefficient of determination close to 0.9).

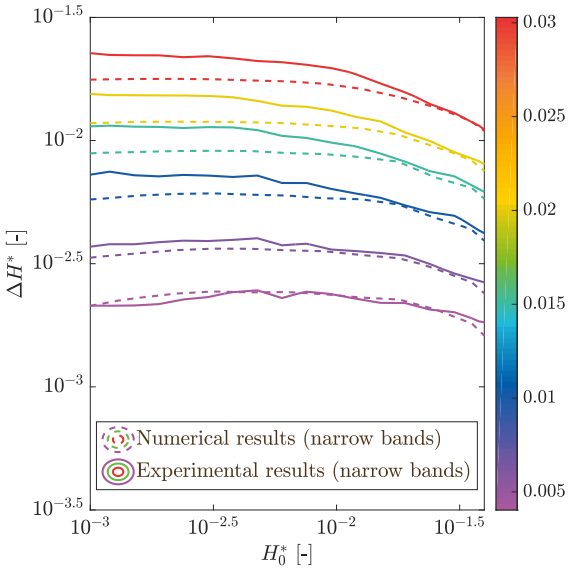

FIGURE 5.9 - Reduced average first passage time $U_1 S_u/4$ as a function of H_0^* and ΔH^*. Comparison of the maps obtained experimentally and numerically for narrow-band excitations (F_u on $[0.77\,f_0\,;1.27\,f_0]$, F_w on $[0.87\,f_0\,;1.13\,f_0]$). $a = 29$, $S_w = 3\cdot 10^{-9}$, $S_u = 8\cdot 10^{-4}$. Nonlinear case.

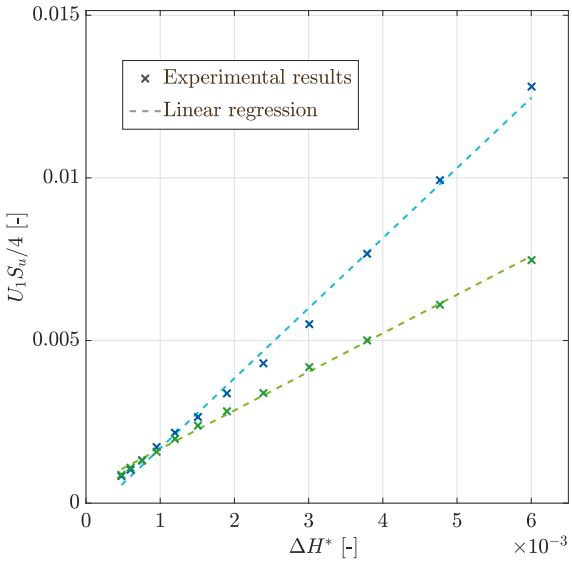

FIGURE 5.10 - Cross-sections of the average first passage time map (Fig. 5.9) in the incubation regime for $H_0^* = 5\cdot 10^{-2}$ (in blue) and $H_0^* = 6\cdot 10^{-3}$ (in green). Experimental data and linear regression. Nonlinear case.

5.3 Multi-degree-of-freedom system first passage time

Numerical study of the first passage time of the multi-degree-of-freedom system would be prohibitively expensive in terms of computation time since it requires a large number of numerical integrations of a system with many degrees of freedom. Only experimental tests performed on the physical set-up of the structure are therefore reported in this section. The intensities of the excitations are chosen sufficiently small to limit the excitation of the system nonlinearities.

The forced excitation is defined as a narrow-band process of constant power spectral density $\tilde{S}_w = 10^{-4}$ N^2/Hz on the frequency interval [30 ; 70] Hz. As a first attempt to explore the dynamics of the multi-degree-of-freedom system, this frequency interval covers the second and the third bending modes of the strip. The parametric excitation is defined as a broadband process of constant power spectral density $\tilde{S}_u = 8\cdot 10^{-6}$ N^2/Hz on the frequency interval [10 ; 400] Hz.

As far as the multi-degree-of-freedom equations of motion can be decoupled in a set of single-degree-of-freedom motion equations of the form (5.1), the Hamiltonian of the multi-degree-of freedom system can be expressed as

$$H(t) = \frac{1}{2}\sum_i m_{\mathrm{eq},i}\,\dot{q}_i^2(t) + \frac{1}{2}\sum_i k_{\mathrm{eq},i}\,q_i^2(t), \tag{5.17}$$

where $m_{\mathrm{eq},i}$ and $k_{\mathrm{eq},i}$ are the equivalent mass and stiffness coefficients of mode i and $q_i(t)$ is the i-th modal coordinate. The physical response of the structure at the degree of freedom n_P writes

$$x(t) = \sum_i \mathbf{\Phi}(n_P, i) q_i(t). \tag{5.18}$$

In the current case, even if the forced excitation covers only two modes of the structure, the other modes are also excited. Indeed, the broadband parametric excitation covers the second harmonics of the other bending modes so that they are also triggered. The first six bending modes are therefore taken into account in the computation of the Hamiltonian. The equivalent parameters of the different bending modes have been identified in section 4.1 about the model reduction. The modal coordinates $q_i(t)$ are extracted from the measured velocity signal. The products $\mathbf{\Phi}(n_P, i)q_i(t)$ are obtained by filtering the signal around the natural frequencies of the corresponding mode. The $q_i(t)$ are obtained by dividing these products by $\mathbf{\Phi}(n_P, i)$, the value of the mode at the point where the velocity is measured. This method assumes that an accurate numerical model of the structure is available.

The experimental map is obtained using the same algorithm as before. The results are shown in Fig. 5.11. A global behavior similar to the one expected for single-degree-of-freedom systems is observed. The first passage time is approximately independent of the initial energy level H_0 when H_0 is small and ΔH sufficiently high. This corresponds to the additive regime. The beginning of a multiplicative regime is also observed for the largest values of the initial energy level. An incubation regime is identified for small values of the energy increment ΔH. Fig. 5.12 illustrates the linearity of the first passage time in the incubation regime.

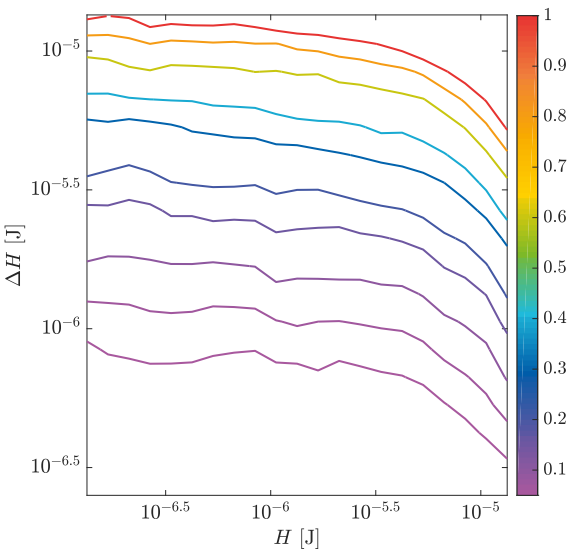

FIGURE 5.11 - Average first passage time $\tilde{U}_1$ [s] as a function of H_0 and ΔH. Map obtained experimentally for broadband excitations (F_w on [30 ; 70] Hz, F_u on [10 ; 400] Hz). $\tilde{S}_w = 10^{-4}$ N^2/Hz, $\tilde{S}_u = 8 \cdot 10^{-6}$ N^2/Hz.

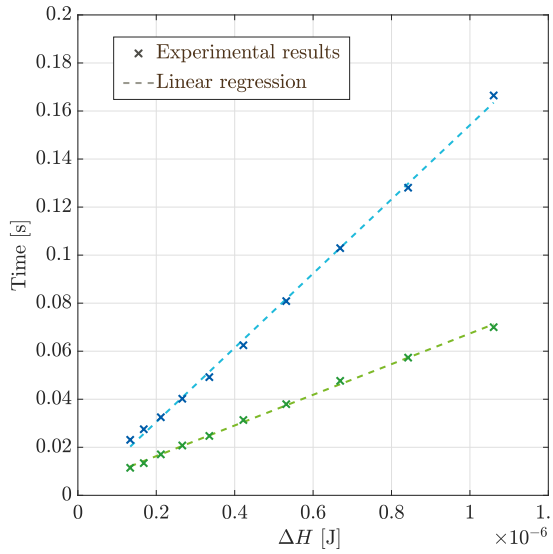

FIGURE 5.12 - Cross-sections of the average first passage time map (Fig. 5.11) for $H_0 = 10^{-5}$ J (in blue) and $H_0 = 10^{-5.5}$ J (in green).

CONCLUSIONS AND PERSPECTIVES

This work aimed at designing and using an experimental set-up to illustrate and provide empirical evidence of the main results of the theory of first passage time developed in [36, 37]. As reported in the first part of the work, the current theory applies to quasi-Hamiltonian systems meeting three strong and restrictive conditions. Firstly, the system is characterized by a single degree of freedom. Secondly, the dynamics of the system is governed by a linear Mathieu equation. Thirdly, the system is subjected to broadband forced and parametric excitations (δ-correlated Brownian processes).

In order to provide a sound empirical validation of the theory, the challenge was therefore to design an experimental set-up using a real mechanical structure that nevertheless complies with the three above conditions to a reasonable level of approximation. The selected structure consists in a vertical steel strip pre-stressed by a mass. It is excited by horizontal and vertical shakers to apply, respectively, the forced and parametric excitations.

First, a finite element model of the mechanical structure has been built to get a deep insight into its dynamics and help guiding the choice of the experimental parameters. The Least Square Complex Exponential, Least Square Frequency Domain and Stochastic Subspace Identification methods have been applied to conduct the experimental modal analysis of the strip. After updating, the numerical model reproduces the modal properties of the real strip with a very good accuracy.

The inherently multi-degree-of-freedom system must be reduced to match the assumption of a single-degree-of-freedom system behind the analytical theory of first passage time. This is done by defining the forced and parametric excitations as narrow-band random processes triggering only one bending mode of the structure. The amplitudes of the forced and parametric excitations have also to be kept small to avoid entering the nonlinear regime.

Since analytical results are not available for the first passage time of systems subjected to narrow-band excitations, a numerical study has been performed and some general conclusions have been drawn about the influence of the frequency bands of the forced and parametric excitations on the first passage time. The general behavior of the average first passage time for broadband excitations is recovered in the whole map as long as the natural frequency of the oscillator is included in the frequency band of the forced excitation and the frequency band of the parametric excitation contains the second harmonic of the natural frequency. When these conditions are met, small quantitative differences can be observed when broadband or narrow-band excitations are used but the dynamics remains qualitatively similar. The shift between the corresponding maps increases when the frequency bandwidths decrease. It also increases with the amplitude of the parametric excitation and with the damping factor.

The previous steps provide a rationale for selecting the appropriate parameters of the experimental testing. The experimental first passage time map has been built and compared with the theoretical and model results. A good quantitative match is observed between the experimental map and the numerical results obtained with Monte Carlo simulations of the system subjected to narrow-band excitations. The experimental results are also qualitatively similar to the theoretical ones for broadband excitations. Both the additive and incubation regimes are clearly identified. Only the beginning of the multiplicative regime can however be observed. Some results related to the multi-degree-of-freedom system and the excitation of its nonlinear characteristics have also been presented and similar regimes have been observed. The current work provides therefore a sound experimental validation of the theory of first passage time.

The concepts presented and illustrated in this report can appear very theoretical and the considered experimental set-up, while realistic, is still rather simple with respect to actual mechanical systems encountered in the industry. Nevertheless, this work further opens the way to promising applications of the concept of first passage time to revisit many problems in all fields of engineering. Some typical examples of application in various areas of engineering are briefly described below.

Sheet metal coating process The simple geometry of the experimental academic set-up studied in this work is very close to the geometry presented in [19] which details the process of galvanization of metal sheets. Galvanization is the process of applying a protective zinc coating to steel or iron to prevent rusting. Fig. I represents the geometry of the industrial galvanization tool studied in [19] that looks similar to the pre-stressed strip studied in this work. First, the very thin metal sheet is drawn through a bath of melted zinc. Then, it is dried in air and transported between two rollers so that the zinc solidifies.

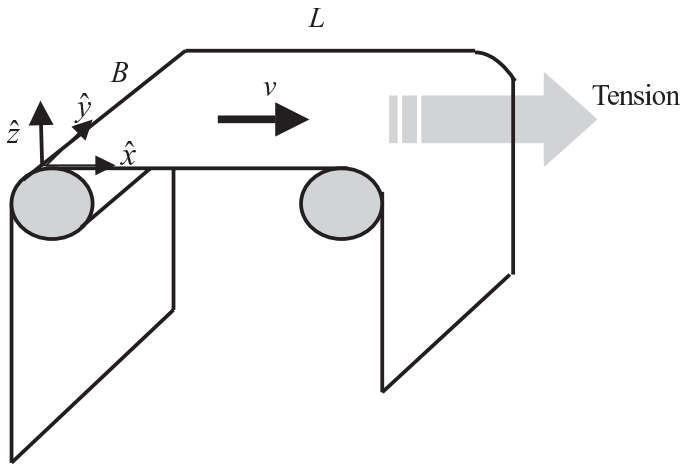

FIGURE I - Sheet metal coating process: metal sheet moving between two rollers at the translation speed v and subjected to tension [19].

Vibrations come from different mechanisms. An external excitation is produced by the eccentric rotation of the rollers. This triggers out of plane vibrations of the sheet. This source of excitation can be reduced by detuning the rollers rotation frequency from any natural frequency of the sheet or by reducing roller eccentricity by frequent servicing of the rollers' bearings. This source of excitation is however never completely suppressed as the bearings experience rapid wear in the zinc bath. Another external forcing is experienced by the metal sheet during the drying phase when air is blown on the surface to speed up the drying. Then, the metal sheet also experiences a time-varying tension. Fig. II shows the temporal evolution of the tension (measured experimentally on a real set-up), which varies randomly by up to 10% of the mean tension. This causes a random parametric excitation of the structure.

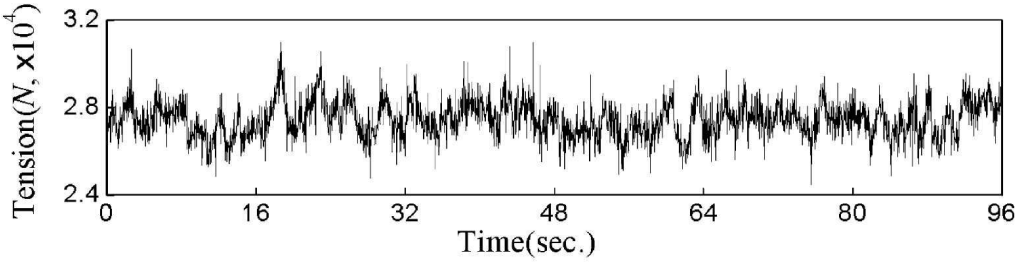

FIGURE II - Tension measured experimentally on a plate during the coating process [19].

The vibration of metal sheets during zinc coating processes can lead to uneven coating thickness and overall poor product quality. It must therefore be controlled. It is suggested here that the theory of first passage time could provide an efficient framework for the design of such mechanical systems. The metal sheet is indeed subjected to both forced and parametric stochastic excitations, which corresponds to the conditions of the Mathieu equation. The first passage time theory could help to answer the question of the design of the velocity v of the sheet, the design of the rollers and the conditions of air blowing to apply so that the plate does not reach a too high energy level in the time required for the complete coating and drying process.

This real industrial application departs however from the restrictive conditions of the theory developed analytically. Firstly, this structure can a priori not be simply modeled by a single-degree-of-freedom system. Secondly, the forced and parametric excitations are not broadband processes of constant power spectral densities. Fig. III shows an example of the power spectral density of the experimentally measured time-varying tension (the parametric excitation) that does not appear to be constant on the complete frequency band. Thirdly, it should also be noted that the crowned shape of the roller creates spatially varying tension in the lateral direction ($\hat{y}$ in Fig. I). This influences the linear vibration characteristics of wide sheets and a nonlinear theory of first passage time needs therefore to be developed.

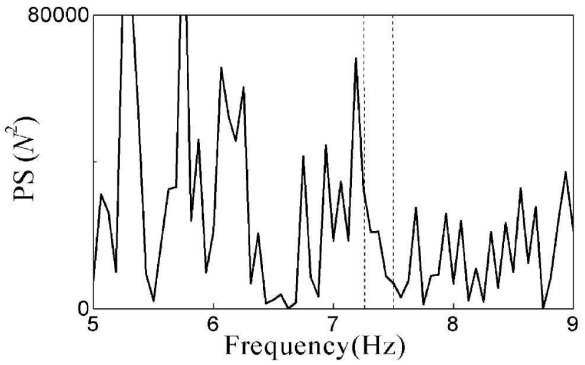

FIGURE III - Power spectral density of the tension measured experimentally on a plate during the coating process [19].

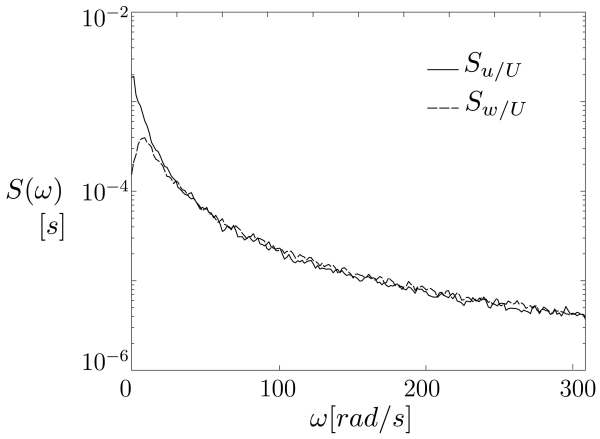

FIGURE IV - Power spectral densities of the forced and parametric excitations acting on a crane measured during wind tunnel tests [35].

Wind engineering As already introduced in [35], the first passage time theory provides a nice new analysis tool in experimental wind engineering. In this field, transient regimes are indeed induced by the aerodynamic loading providing forced and parametric random excitations. The increasing number of accidents due to high wind and to autorotation of tower cranes motivates the search for new efficient scientific methods. Since the dynamics of a tower crane that is left free to rotate in turbulent (and therefore random) wind field can be modeled by a governing equation of the form of the linear Mathieu equation, the first passage time theory appears as a good candidate for the study of such systems. The first passage theory could help to predict the time required for the crane to exhibit large amplitude oscillations or even complete autorotations under given wind conditions. This could also help to predict the duration of the tests in wind tunnels required to reach some energy levels. In the case of rotation of tower crane, the assumption of single-degree-of-freedom structure is not far from reality since the focus is mainly put on the rotation angle. Tests in wind tunnels have revealed that the power spectral densities of the excitations are not broadband processes (Fig. IV), but are closer to narrow-band processes similar to those studied in this work.

Microelectromechanical systems Some applications can also be found on smaller length scales, in microelectromechanical systems (MEMS). As one example among others, MEMS used for the detection of particles are of great societal value. These systems are widely used in airports and public places to detect explosives on people and luggage. Such systems are often based on Ion Mobility Spectrometry that consists in ionizing the sample, applying an electrical field and detecting the concentration of ions that gain a specific velocity [10]. It is suggested here that the theory of first passage time could help to design such systems and understand which parameters of the problem could be tuned to minimize the detection time, *i.e.* the first passage time at a given energy level. This would allow to reduce waiting time in airports.

Predictive maintenance The theory of first passage time could also be applied to predictive maintenance tools. Predictive maintenance techniques are designed to determine the condition of in-service equipment and predict when maintenance should be performed. The theory would also help to design a structure so that the first failure occurs late enough with a given probability.

The above examples in various fields of engineering show that the theory of first passage time seems very promising but needs some further developments to characterize real life systems, which are often (always) multi-degree-of-freedom, nonlinear and subjected to colored excitations.

The current work contributes to broadening the scope of the first passage time theory introduced in [36, 37] beyond the context of one-degree-of-freedom linear Mathieu systems subjected to broadband excitations considered so far. It is also a first physical evidence that the first passage time of real multi-degree-of-freedom mechanical systems can be characterized with the physical properties of the structure. Moreover, by studying numerically and experimentally oscillators subjected to narrow-band excitations, some general conclusions have been drawn. The first experimental results related to the first passage time maps of nonlinear and multi-degree-of-freedom systems have also been reported.

This study suggests that work is still needed to go further with analytical, numerical and experimental studies of the first passage time of systems subjected to colored excitations, showing nonlinear behavior or inherently multi-degree-of-freedom. In this regard, the specific experimental set-up considered here could be used to carry out an experimental study of the higher order moments of the first passage time of systems subjected to narrow-band processes. Besides, a nonlinear model could also be built to support a detailed numerical and experimental study of the influence of nonlinearities on the first passage time map. More generally, analytical studies of the first passage time of systems subjected to colored excitations, and in particular to narrow-band excitations, could be conducted to get a better insight into the phenomena.

BIBLIOGRAPHY

[1] R. J. ALLEMANG AND D. L. BROWN, *A correlation coefficient for modal vector analysis*, Proceedings of the 1st International Modal Analysis Conference, (1982), pp. 110–116.

[2] M. ASHBY, *Materials Selection in Mechanical Design*, Elsevier, 3rd ed., 2005.

[3] P. AVITABILE, *Modal Testing: A Practitioner's Guide*, Wiley, 1st ed., 2017.

[4] F. BALLIO AND A. GUADAGNINI, *Convergence assessment of numerical Monte Carlo simulations in groundwater hydrology*, Water Resources Research, 40 (2004).

[5] L. A. BERGMAN AND J. C. HEINRICH, *On the moments of time to first passage of the linear oscillator*, Earthquake Engineering & Structural Dynamics, 9 (1981), pp. 197–204.

[6] R. D. BLEVINS, *Formulas for Natural Frequency and Mode Shape*, Krieger Publishing Company, 1st ed., 1979.

[7] D. BROWN, R. ALLEMANG, R. ZIMMERMAN, AND M. MERGEAY, *Parameter Estimation Techniques for Modal Analysis*, SAE Transactions, 88 (1979).

[8] S. BUTTERWORTH, *On the theory of filter amplifiers*, Wireless Engineer, 7 (1930), pp. 536–541.

[9] M. CARTMELL, *Introduction to Linear, Parametric and Nonlinear Vibrations*, Springer, 1st ed., 1990.

[10] R. CUMERAS, *Review on Ion Mobility Spectrometry: Part 1 - Current Instrumentation*, The Analyst, 140(5) (2015), pp. 1376–1390.

[11] E. DE SÁ CAETANO, *Cable Vibrations in Cable-stayed Bridges*, Structural engineering documents, IABSE, 2007.

[12] E. DELHEZ, *Experimental and numerical modal analyses of a pre-stressed steel strip*, Internal report, University of Liège, 2017.

[13] E. DELHEZ, H. VANVINCKENROYE, J.-C. GOLINVAL, AND V. DENOËL, *Numerical and experimental study of first passage time of a steel strip subjected to forced and parametric excitations*, Proceedings of the 28th International Conference on Noise and Vibration Engineering, (2018).

[14] V. DENOËL, *Application des méthodes d'analyse stochastique à l'étude des effets du vent sur les structures du génie civil*, PhD thesis, University of Liège, 2005.

[15] D. EWINS, *Modal Testing: Theory, Practice and Application*, Research Studies Press Ltd, 2nd ed., 2000.

[16] M. GÉRADIN AND D. RIXEN, *Mechanical Vibrations: Theory and Application to Structural Dynamics*, Wiley, 3rd ed., 2015.

[17] M. GITTERMAN, *Spring pendulum: Parametric excitation vs an external force*, Physica A: Statistical Mechanics and its Applications, 389 (2010), pp. 3101–3108.

[18] G. KERSCHEN, K. WORDEN, A. F. VAKAKIS, AND J.-C. GOLINVAL, *Past, present and future of nonlinear system identification in structural dynamics*, Mechanical Systems and Signal Processing, 20 (2006), pp. 505–592.

[19] C. KIM, N. PERKINS, AND C. LEE, *Parametric resonance of plates in a sheet metal coating process*, Journal of Sound and Vibration, 268 (2003), pp. 679–697.

[20] I. A. KOUGIOUMTZOGLOU AND P. D. SPANOS, *An approximate approach for nonlinear system response determination under evolutionary stochastic excitation*, Current Science, 97 (2009), pp. 1203–1211.

[21] J. LILIEN AND A. DA COSTA, *Vibration amplitudes caused by parametric excitation of cable stayed structures*, Journal of Sound and Vibration, 174 (1994), pp. 69–90.

[22] Y. LUKE, *The Special Functions and Their Approximations*, Mathematics in Science and Engineering, Elsevier Science, 1969.

[23] N. MAIA, J. SILVA, J. HE, J. LIEVEN, R.-M. LIN, G. SKINGLE, W. TO, AND A. URGUEIRA, *Theoretical and Experimental Modal Analysis*, Research Studies Press Ltd, 1st ed., 1997.

[24] E. MATHIEU, *Mémoire sur le mouvement vibratoire d'une membrane de forme elliptique*, Journal de Mathématiques Pures et Appliquées, 13 (1868), pp. 137–203.

[25] J. P. NOËL AND G. KERSCHEN, *Nonlinear system identification in structural dynamics: 10 more years of progress*, Mechanical Systems and Signal Processing, 83 (2017), pp. 2–35.

[26] J. J. OLSEN, *Unified Flight Mechanics and Aeroelasticity for Accelerating, Maneuvering, Flexible Aircraft*, Research and Technology Organization Meeting Proceedings, (2000).

[27] B. PEETERS, H. VAN DER AUWERAER, P. GUILLAUME, AND J. LEURIDAN, *The PolyMAX frequency-domain method: a new standard for modal parameter estimation?*, Shock and Vibration, 11 (2004), pp. 395–409.

[28] L. PONTRYAGIN, A. ANDRONOV, AND A. VITT, *Appendix: On the statistical treatment of dynamical systems*, in Noise in Nonlinear Dynamical Systems Volume 1. Theory of Continuous Fokker-Planck Systems, Cambridge University Press, 1989, pp. 329–348.

[29] F. J. POULIN AND G. R. FLIERL, *The stochastic Mathieu's equation*, Proceedings of the Royal Society of London A: Mathematical, Physical and Engineering Sciences, 464 (2008), pp. 1885–1904.

[30] A. PRIKHODKO, A. NESTEROV, AND S. NESTEROV, *Analysis of Mathieu equation stable solutions in the first zone of stability*, Procedia Engineering, 150 (2016), pp. 341–346. 2nd International Conference on Industrial Engineering (ICIE-2016).

[31] T. PRIMOZIC, *Estimating expected first passage times using multilevel Monte Carlo algorithm*, Master thesis, University of Oxford, 2011.

[32] E. ROSTOVA, G. DIETLER, AND S. SEKATSKII, *Application of the Mathieu's equation for a design of a photonic crystal supporting surface electromagnetic waves*, Advanced Electromagnetics, 4 (2015), pp. 17–24.

[33] A. J. F. SIEGERT, *On the first passage time probability problem*, Physical Review, 81 (1951), pp. 617–623.

[34] P. VAN OVERSCHEE AND B. DE MOOR, *Subspace Identification for Linear Systems: Theory - Implementation - Applications*, Springer US, 1st ed., 1996.

[35] H. VANVINCKENROYE, T. ANDRIANNE, AND V. DENOËL, *First passage time as an analysis tool in experimental wind engineering*, Journal of Wind Engineering and Industrial Aerodynamics, 177 (2018), pp. 366–375.

[36] H. VANVINCKENROYE AND V. DENOËL, *Average first-passage time of a quasi-Hamiltonian Mathieu oscillator with parametric and forcing excitations*, Journal of Sound and Vibration, 406 (2017), pp. 328–345.

[37] H. VANVINCKENROYE AND V. DENOËL, *Second-order moment of the first passage time of a quasi-Hamiltonian oscillator with stochastic parametric and forcing excitations*, Journal of Sound and Vibration, 427 (2018), pp. 178–187.

[38] M. WARD, *Mathematical Modeling and Analysis of Industrial Problems - Basic Floquet Theory*, Lecture notes, University of British Columbia, 2010.

[39] P. WELCH, *The use of fast Fourier transform for the estimation of power spectra: A method based on time averaging over short, modified periodograms*, IEEE Transactions on Audio and Electroacoustics, 15 (1967), pp. 70–73.

[40] *Hasberg official website*. `https://www.hasberg-schneider.de`. [Last view March 26th, 2018].

[41] *LTAS (Faculty of Applied Sciences - ULiège) official website*. `www.ltas-vis.ulg.ac.be`. [Last view April 11th, 2018].

[42] *MathWorks official website*. `https://www.mathworks.com`. [Last view April 11th, 2018].

[43] *Siemens official website*. `https://www.plm.automation.siemens.com`. [Last view November 5th, 2017].

[44] *UEE (Faculty of Applied Sciences - ULiège) official website*. `www.uee.uliege.be`. [Last view May 18th, 2018].

[45] *TIRA official website*. `https://www.tira-gmbh.de`. [Last view March 11th, 2018].

[46] *Wolfram official website*. `https://www.wolfram.com`. [Last view April 11th, 2018].

APPENDIX A

NUMERICAL GENERATION OF STOCHASTIC PROCESSES

The first passage time theory introduced in section 1.2 applies to oscillators subjected to broadband random excitations characterized by a constant power spectral density (PSD). Narrow-band excitations are however also considered in this work. The objective of this appendix is to define the main conventions used through the work and to describe how such stochastic processes can be generated numerically.

A.1 Power spectral density

Different conventions are used in the literature to define the power spectral density. This section defines the specific conventions used in this report and explains how the PSD are computed numerically.

A.1.1 Definition

The stochastic process $x(t)$ can be seen as a succession of random variables [14]. The value taken by x at a given instant $t = t_1$ is a random variable $\mathcal{X}_1 := x(t_1)$. The first moment of the random process x is therefore a function of time and can be evaluated at any time t_1 by

$$\mu_x(t_1) = E\left[\mathcal{X}_1\right]. \tag{A.1}$$

The autocovariance function of the stochastic process x is defined by

$$R_x(t_1, t_2) = E\left[\mathcal{X}_1 \mathcal{X}_2\right] - \mu_x(t_1)\mu_x(t_2), \tag{A.2}$$

where $\mathcal{X}_2 := x(t_2)$. This function allows to quantify the degree of correlation between the values taken by the process at two different instants. For stationary processes, the autocovariance function depends only on the time increment $\Delta t = |t_2 - t_1|$ and is simply written $R_x(\Delta t)$. The Fourier transform of the autocovariance function is the power spectral density $S_x(f)$, which is defined in the frequency domain by

$$S_x(f) = \int_{-\infty}^{+\infty} R_x(\tau) e^{-j2\pi f \tau} d\tau. \tag{A.3}$$

The power spectral density describes the distribution of power into frequency components making up the signal. The integral of the power spectral density over the whole domain of frequency gives the variance of the signal

$$\int_{-\infty}^{+\infty} S_x(f) df = \sigma_x^2 \tag{A.4}$$

and is therefore linked to the total energy of the signal.

Under the assumption of ergodicity, the power spectral density of a stationary process can be estimated from a single realization $x_i(t)$ by

$$S_x(f) = \lim_{T\to\infty} \frac{1}{T}|X_i(f,T)|^2, \tag{A.5}$$

where $X_i(f,T)$ is the truncated Fourier transform of the process

$$X_i(f,T) = \int_{-T/2}^{+T/2} x_i(t)e^{-j2\pi ft}dt. \tag{A.6}$$

A.1.2 Numerical computation

Numerically, power spectral densities are usually not computed by (A.5). In order to limit the importance of the two underlying assumptions (*i.e.* ergodicity and stationarity of the process), the power spectral density is computed by the Welch method [39]. This method consists in subdividing the time sample of the process in several blocks, which may overlap (Fig. A.1). For each block, a formula similar to (A.5) is used to get a spectrogram, *i.e* the power spectral density characterizing the block. An estimate of the power spectral density of the process is obtained by averaging all the spectrograms. MATLAB function `pwelch` provides the power spectral density estimated via Welch's method.

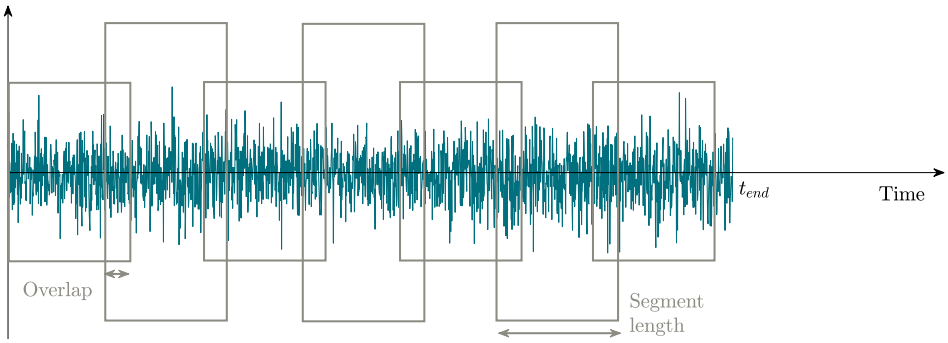

FIGURE A.1 - Illustration of the Welch method for the computation of the power spectral density.

A.2 Random process generation

This section briefly explains how broadband and narrow-band random processes are generated numerically.

A.2.1 Broadband noise generation

The analytical theory of first passage time relies on the assumption that the forced and parametric excitations are δ-correlated Brownian white noises, *i.e.* stationary processes whose frequency content is uniformly distributed on $f \in\ ]-\infty;+\infty[$. By (A.4), the energy associated with such a process would be infinite, which is not physically acceptable. The autocovariance of such a process can be expressed as

$$R_x(\Delta t) = R_0\delta(\Delta t), \tag{A.7}$$

which means that there is no correlation between the values taken by the process at two distinct instants, even if the two instants are very close to each other. In practice, a finite discretization is used with a small but non-zero time step dt and no information is available about what happens between two generated values. Shannon theorem states that for a sampling frequency $f_s = 1/dt$, the frequency content outside the interval $[-f_s/2\ ;\ f_s/2]$ cannot be represented.

Numerically, a white noise of limited band with a constant power spectral density S_0 on the frequency interval $[-f_s/2\ ;\ f_s/2]$ is therefore generated. The frequency content outside this interval is equal to zero. The variance of this process is found using (A.4) and given by $\sigma^2 = S_0 f_s$ with the conventions adopted in this report. One way of generating a Gaussian white noise therefore consists in generating a set of samples coming from a Gaussian distribution of mean and variance specified.

A.2.2 Narrow-band noise generation

Two different approaches can be followed to define numerically narrow-band noises of constant power spectral densities.

On the one hand, narrow-band processes can be generated by filtering a generated broadband white noise and keeping only the frequency content of interest. The Filter Designer tool of the Signal Processing MATLAB toolbox is used to design the filter [42]. A Butterworth filter is selected because it is considered as the maximally flat magnitude filter and is designed to have a frequency response as flat as possible in the passband [8]. Fig. A.2 shows an example of the results obtained with this generation method[1]. The blue signal corresponds to the white noise defined on the whole frequency band. The signals shown in green and red are obtained by filtering the blue signal with Butterworth filters of orders 60 and 90 respectively. This generation method has a low computation time but the power spectral densities are not perfectly rectangular so that some leakage phenomena can be observed. The order increase is limited by stability issues.

On the other hand, a narrow-band signal can be defined in the frequency domain using (A.5) and transposed in the time domain using Fourier transform theory [14]. The limit expression (A.5) is required because a finite temporal signal cannot contain all the information required to describe the power spectral density at low frequencies. In practice, however, the frequency content of the studied stochastic processes is often included in a frequency interval $[f_{\min}\,;\ f_{\max}]$. The smallest frequencies can therefore be represented with time signals of duration of the order of $1/f_{\min}$, and the limit symbol can be omitted provided the time signal is sufficiently long. The truncated Fourier transform of the signal must be such that

$$|X_i(f,T)| = \sqrt{TS_x(f)}. \tag{A.8}$$

One way to satisfy this relation consists in choosing

$$X_i(f,T) = \sqrt{TS_x(f)}e^{j\phi(f)}, \tag{A.9}$$

where $\phi(f)$ is an arbitrary phase (e.g. a random variable of uniform distribution in [0 ; 2π]). The inverse Fourier transform eventually allows to generate the narrow-band process. This generation method is very accurate (see the Fourier transform of the signal generated in Fig. A.3) but the passage from the frequency domain to the time domain using an inverse Fourier transform requires a large computation time. As illustrated in Fig. A.4, the computation time of the first method is smaller than the computation time of the second one[2].

For the current study, *i.e.* the numerical construction of first passage time maps, it is checked that both methods of narrow-band processes generation provide the same final map, with similar convergence rates. Narrow-band processes are therefore obtained by filtering broadband processes since this method is much less demanding in computation time.

[1] Only the half parts of the PSD corresponding to positive frequencies are represented as PSD are symmetric with respect to the origin.

[2] Simulations done on a PC (Windows 10) with an Intel Core I7 processor.

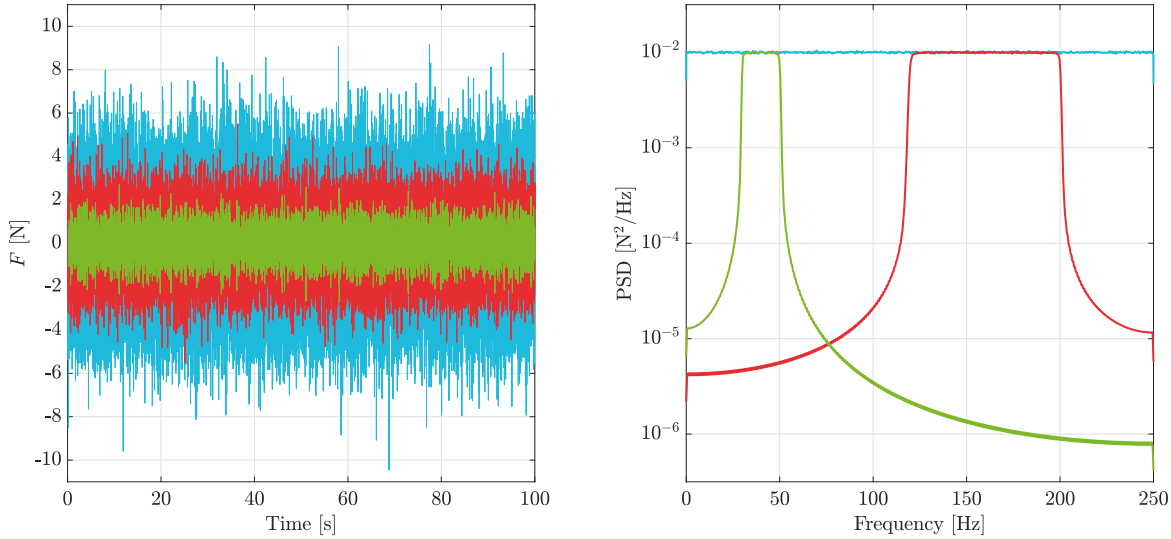

(a) Force signal.

(b) Power spectral density.

FIGURE A.2 - Stochastic processes and corresponding power spectral densities. The blue signal is a broadband process defined on the whole frequency band ($S_F = 10^{-2}$ N^2/Hz, $f_s = 500$ Hz). The green and red signals are obtained by filtering the blue signal with Butterworth filters of orders 60 and 90 between 30 and 50 Hz and between 120 and 200 Hz.

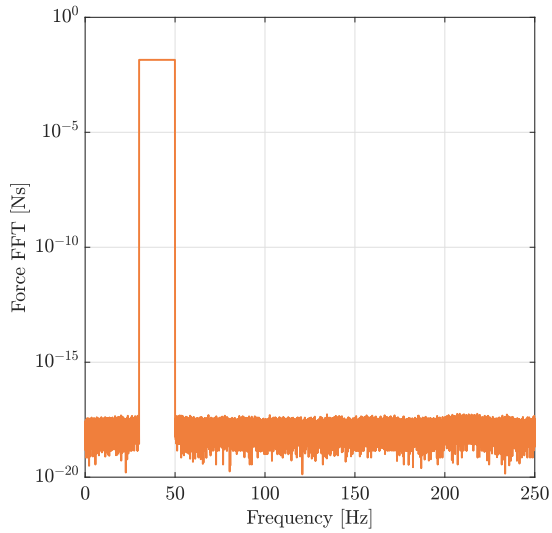

FIGURE A.3 - Fast Fourier transform of the narrow-band noise between 30 and 50 Hz generated by the second method ($S_F = 10^{-2}$ N^2/Hz, $f_s = 500$ Hz).

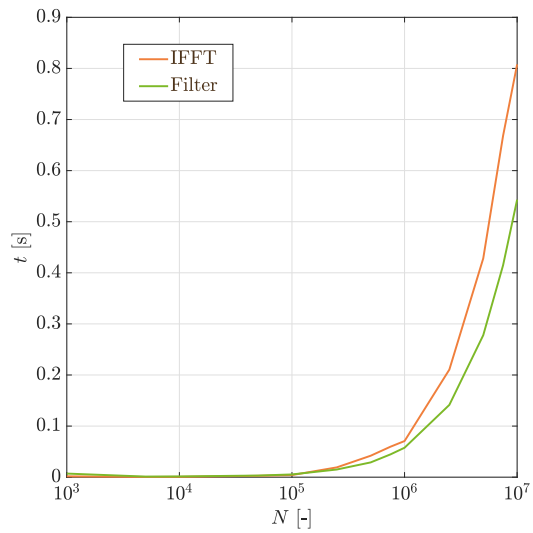

FIGURE A.4 - Computation times of the two narrow-band process generation methods presented as a function of the length N of the generated signal ($f_s = 500$ Hz).

APPENDIX B

NUMERICAL INTEGRATION OF THE EQUATIONS OF MOTION

This appendix describes the numerical method used to integrate the governing equations and compute the time response. It also defines the numerical parameters associated to this integration.

The structural response to external forced and parametric excitations is computed by direct integration of the equations of motion using a Newmark integration scheme. Starting from given initial conditions for the position and the velocity, the prediction/correction Newmark scheme is used to advance the solution forward in time. The procedure is summarized in Fig. B.1.

This integration scheme is characterized by three distinct integration parameters: the time step of integration h and the two parameters γ and β. The parameter γ is set equal to 0.5 because this leads to the minimum integration errors [16]. Moreover, since this value corresponds to the stability limit, it does not induce artificial amplification nor damping of the response. To ensure an unconditionally stable integration method, β must be equal to or greater than 0.25. The maximum accuracy is reached when β is exactly equal to 0.25. For these reasons, β is set to 0.25 even if this choice does not minimize the integration errors. The algorithm corresponding to these values of γ and β is called "average constant acceleration" and is the standard algorithm used in commercial codes. For a single-degree-of-freedom oscillator without damping, the numerical damping associated to this algorithm is equal to zero while the relative error on the period T increases with the pulsation ω as

$$\frac{\Delta T}{T} \sim \frac{\omega^2 h^2}{12}. \tag{B.1}$$

A particular attention should be paid to the choice of the time step of integration h. First, the time step must be smaller than the characteristic time of the excitation. When the excitation is defined as a random white process, this is not a constraint since there is no characteristic time associated with such a process. For a harmonic excitation, h is defined in such a way that each period of the excitation is discretized with at least 100 points. Then, h must be sufficiently small to represent the response of the system accurately. At least 100 points are used to describe the smallest period (corresponding to the highest frequency) in the response. Because damping is very low, it does not add additional constraints on the time step of integration. Beside these conditions, the time step should also be chosen in such a way that the periodicity error (B.1) induced by the use of Newmark integration scheme is negligible for all frequencies of interest.

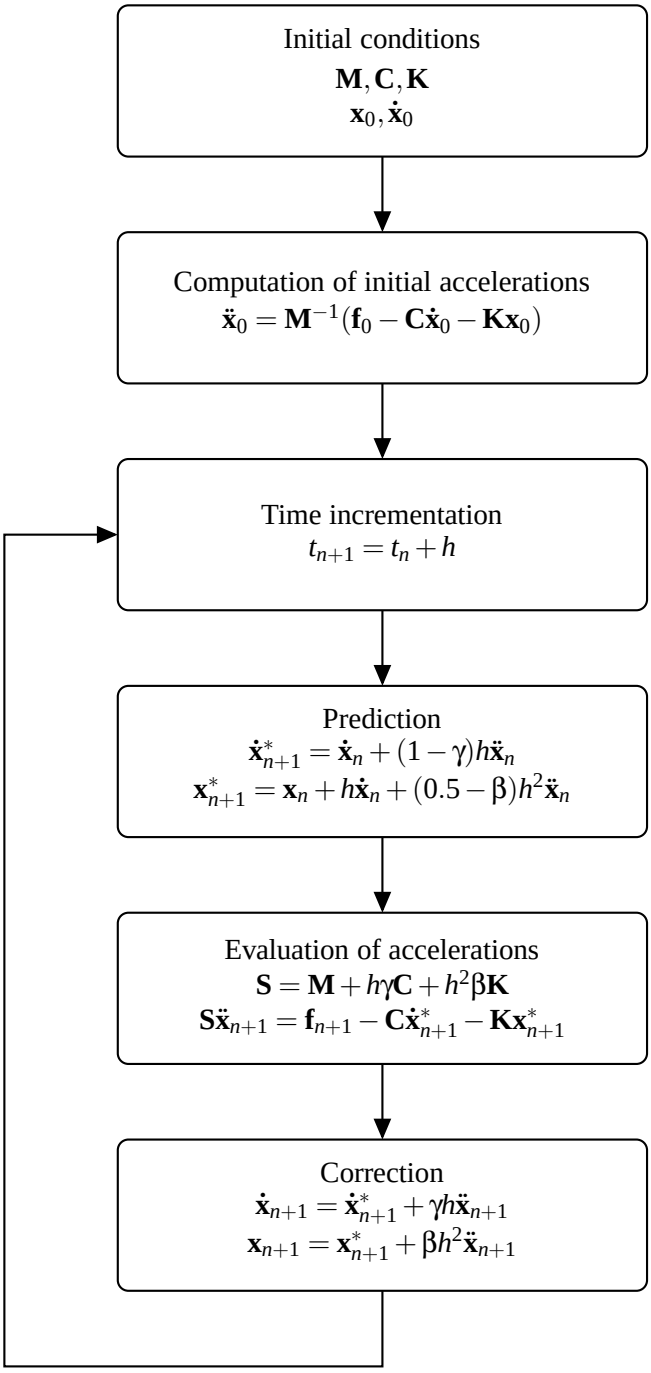

FIGURE B.1 - Newmark integration scheme for linear systems [16].